STATISTICAL PROCESSING METHODS

FOR

POLARIMETRIC IMAGERY

DISSERTATION

Daniel A. LeMaster

GG-12, DAF

AFIT/DEE/ENG/08-18

DEPARTMENT OF THE AIR FORCE

AIR UNIVERSITY

AIR FORCE INSTITUTE OF TECHNOLOGY

Wright-Patterson Air Force Base, Ohio

AFIT/DEE/ENG/08-18

Statistical Processing Methods
for
Polarimetric Imagery

DISSERTATION

Presented to the Faculty

Graduate School of Engineering and Management

Air Force Institute of Technology

Air University

Air Education and Training Command

In Partial Fulfillment of the Requirements for the

Degree of Doctor of Philosophy

Daniel A. LeMaster, B.S.E.P., M.S.

GG-12, DAF

September 2008

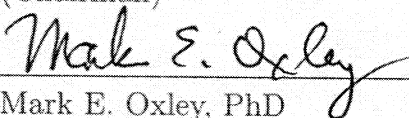APPROVED FOR PUBLIC RELEASE; DISTRIBUTION UNLIMITED.

STATISTICAL PROCESSING METHODS
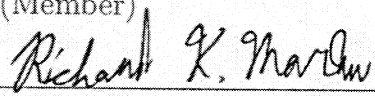
FOR

POLARIMETRIC IMAGERY

Daniel A. LeMaster, B.S.E.P., M.S.
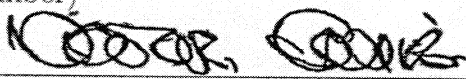
GG-12, DAF

Approved:
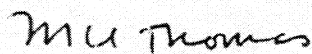
_____   8 Aug 2008
Stephen C. Cain, PhD   Date
(Chairman)

_____   12 Aug 2008
Mark E. Oxley, PhD   Date
(Member)

_____   11 Aug 2008
Richard K. Martin, PhD   Date
(Member)

_____   7 Aug 2008
Victor L. Gamiz, PhD   Date
(Member)

Accepted:

_____   14 Aug 08
M. U. Thomas, PhD   Date
Dean, Graduate School of Engineering and Management

AFIT/DEE/ENG/08-18

Abstract

Estimation theory is applied to a physical model of incoherent polarized light to address problems in polarimetric image registration, restoration, and analysis for electro-optical imaging systems. In the image registration case, the Cramer-Rao lower bound on unbiased joint estimates of the registration parameters and the underlying scene is derived, simplified using matrix methods, and used to explain the behavior of multi-channel linear polarimetric imagers. This discussion is expanded to include biased estimators up to the point where the results become registration algorithm specific.

In the image restoration case, a polarimetric maximum likelihood blind deconvolution algorithm is derived and tested using laboratory and simulated imagery. The angle of polarization, polarized and unpolarized components of the scene, and channel point spread functions are jointly estimated using this approach. The results of this estimation are combined to unambiguously determine the scene state of linear polarization.

Finally, a principal components analysis is derived for polarization imaging systems. This analysis expands upon existing research by including an allowance for partially polarized and unpolarized light. From these results, a means of detecting polarizing objects under weakly polarizing obscurations is proposed by discarding the principal component channels that are insensitive to temporal fluctuations in scene polarization.

Acknowledgements

My advisor, Stephen Cain, has placed an indelible mark on my way of thinking toward optical science, engineering, and professional ethics over the course of two degrees; I am extremely grateful. I must also acknowledge R. Martin and M. Oxley for their excellent teaching abilities and suggestions for my research. Also, special thanks to M. Sambora for his thorough reviews of my work. Finally, I want to thank my wife for everything we have together.

Daniel A. LeMaster

Table of Contents

List of Figures

List of Tables

<div align="center">

STATISTICAL PROCESSING METHODS

FOR

POLARIMETRIC IMAGERY

</div>

I. Introduction

This dissertation describes research in three areas of passive polarimetric image processing: image registration, restoration, and optimized analysis. This chapter provides an overview of polarimetric imaging in remote sensing, describes the problems addressed in this research, and provides an overview of this document as a whole.

1.1 Polarimetric Imaging

Polarimetric Imaging (PI) is a form of remote sensing in which an object or event is characterized in terms of the polarization state of its reflected radiation. Polarization, which is a fundamental property of electro-magnetic radiation, will be defined in detail in Chapter II. The purpose of this section is to introduce and motivate polarimetric imaging as a remote sensing discipline.

Though less common than panchromatic, multispectral, and radar imaging, polarimetry has been applied successfully to a number of remote sensing problems. Astronomers have used PI to characterize the surface of planets and their atmosphere, to determine the surface properties of comets and asteroids, and to investigate novae and the interstellar medium [4, 20]. In the earth's atmosphere, attempts have been made to characterize clouds and atmospheric aerosols. Additionally, PI has been applied to earth surface characterization problems such as hydrology and oceanography as well as inventory and species identification problems in forestry

<div align="center">

1

</div>

and agriculture [8, 47]. The reader may also be interested in applications of PI in machine vision [27] and imaging through scattering media [44]. Finally, additional applications are discussed in texts dedicated to the subject of polarization [5, 42] as well as general optical texts [3, 16, 31].

The military applications of polarimetric imagery include targeting, reconnaissance, and intelligence. The targeting and reconnaissance applications are straightforward: man-made materials tend to produce more highly polarized reflections than their surroundings; ergo, polarimetry is a queueing aid. In addition, adversary camouflage, concealment, and deception techniques are becoming increasingly sophisticated and include those with spectral and radar defeating properties; PI is an additional discriminator that can be used to defeat these techniques separate from or in addition to other sensing modalities. PI has also been shown to be a capable detector of smoke and rocket plumes [7]. Besides intrinsic value as a queueing technique, PI can potentially be used as a material identification and surface characterization tool especially when used in conjunction with spectral analysis. As alluded to previously, PI can be used to characterize asteroids and it has been suggested that PI can be used to locate and characterize space debris [47]. Finally, Strong makes an argument for PI as an enabler for space situational awareness [43].

The literature cited in this section is provided as an overview of the existing work. To facilitate understanding, a more complete literature review on each of the addressed aspects of polarimetric imaging is included in the beginning of each chapter.

1.2 Research Contributions

This work is an estimation theory approach to processing polarization imagery. The references in the preceding section solve problems using polarization imagery and from a physics-based, phenomenological perspective. In other cases, such as the works listed in the introduction to Chapter III, estimation problems (e.g. image

2

registration) are treated as equivalent to their polarization insensitive counterparts. (Noteworthy exceptions to this rule include [43, 51]. Consequently, estimation research into polarization imagery is ripe with possibilities, even in cases that have been exhausted in traditional image processing literature.

Three polarimetric imaging processing problems are addressed in this dissertation: registration, restoration, and optimized analysis. Polarimetric imaging is inherently a multi-channel discipline. A channel, in this context, refers to an imaging path that is most sensitive to a specific state of scene polarization. Reliable channel-to-channel registration is therefore a prerequisite for exploitation of polarimetric data and worthy of further study. Image restoration, which is the process of estimating the true target scene in the presence of a corrupting transmission media and noise, is often studied in traditional intensity imaging to improve sensor performance without increasing cost, size, and complexity; here, these concepts are applied to polarization imaging to achieve the same advantages. And, at the end of the processing chain, the multichannel nature of these data place an unnecessary burden on the analyst in cases where some of the channels contain no useful information. If the unnecessary information can be reduced by eliminating channels (or combinations of channels) using prior knowledge then a tangible savings to the analyst is achieved. An attempt to address each of these points is laid out in the following three chapters.

In Chapter III, the effects of polarization diversity, channel noise, and registration errors on polarization image estimation are considered in the context of the Cramer-Rao Lower Bound (CRLB). The bound is derived for the N-channel case in the presence of random translational registration errors. The bound is then used to study three and four channel polarization imagers and the special case of N misregistered polarization insensitive images. The bulk of this work was originally published in [24]. Some new material on the bound, including a discussion of external parameter measurement versus joint estimation and a correlation based interpretation of the CRLB, can be found in Appendix B.

In Chapter IV, a multichannel blind deconvolution algorithm is developed for polarization imagery. The algorithm is an instance of maximum likelihood estimation derived from expectation maximization theory. This derivation and some results using laboratory data are published in [25]. To this work, the later sections of the chapter are devoted to new material addressing the attributes of the estimator extracted via simulation. This new work includes a comparison of the multichannel estimator to a single channel estimator and a discussion of estimator bias with respect to polarization angle.

In Chapter V, a method is proposed for optimizing combinations of polarimetric imaging channels. Optimization is achieved through identification of combinations of channels that yield the greatest sensitivity to polarization effects, especially for the case of obscured targets. The remaining data are discarded as superfluous. These results are obtained using principal components analysis (PCA) and thresholding based on assumed temporal fluctuations in polarization state. Theoretical work is described for three and four channel systems and simulation is used to demonstrate utility in the four channel case. This work was originally published in [26].

Additionally, several practical laboratory polarimetric imagers were constructed and employed during the course of this research. Though not a novel research contribution per se, this design work is anticipated to be of value to future students and researchers. As such, Appendix D includes the salient design details and a discussion of sampling.

1.3 Scope

PI has applications in both passive and active sensor systems. These systems include those with responsiveness to emitted or reflected radiation in all spectral regimes. The scope of this research, however, is limited to passive electro-optical remote sensing of incoherent radiation. To avoid repetition, the reader should infer this restricted definition of PI throughout the remainder of this document.

Polarization imagers may be comprised of one or more channels. A single polarization channel, either stationary or rotating, can serve as an aid for target queueing [2]. The two channel case, sometimes referred to as polarization difference imaging, is used for target queueing, coarse material identification, and imaging through optically scattering media [41, 44]. As shown in Chapter II, a minimum of three channels is required to unambiguously determine the state of linear polarization and four or more channels can sense both linear and elliptical polarization states. Since linear polarization is more common than elliptical in remote sensing applications, the scope of this research is generally restricted to the linear polarization, three or more channel case.

Polarization imagery is extremely sensitive to the relative orientations of the source, target, and receiver. Assuming there is motion in the target or receiver, the validity of the measurements in a multi-channel polarimetric imager have a temporal component. Throughout this research, all measurements are assumed to be essentially simultaneous on the time scale of the intended target scene.

1.4 Organization

The remainder of this document is organized as follows. Chapter II provides background on the fundamentals of incoherent polarized light, the mathematical description of its interaction with matter, and a largely qualitative discussion of the practical aspects of polarimetric remote sensing. At the end of the chapter, there is a brief discussion of atmospheric effects on polarimetric imaging systems. In Chapter III, the Cramer-Rao bound for the estimation of polarimetric imagery is derived and applied in a series of imaging case studies. The multichannel polarimetric blind deconvolution algorithm is derived and tested using laboratory data and simulation in Chapter IV. Next, the PCA-based channel optimization procedure is laid out in Chapter V. The document is summarized and concluded in Chapter VI. The appendices contain some useful background derivations (A), expansions on the

Cramer-Rao bound work (B), some additional derivation for the blind deconvolution problem (C), and a mechanical description of the polarization imagers constructed for laboratory use (D).

II. Overview of Polarimetry

The purpose of this chapter is to provide background on some recurring themes throughout this research. Chief among these topics is the mathematical formalism used here to describe the manipulation of polarized light: the Stokes vectors and Mueller matrices. These concepts are then used to describe a polarimetric imaging system. A brief section is then devoted to the phenomenology of polarimetric remote sensing. Finally, an overview of atmospheric effects is provided.

2.1 The Stokes Parameters

The Stokes parameters are a standard tool for describing the polarized state of light in passive remote sensing literature [6]. The utility of the Stokes parameters stems from the fact that they can be determined directly from observables. To illustrate this critical point, the Stokes parameters are derived here by closely following the work of Collett [5] but modified slightly using some ideas from statistical optics.

The analytic signal representation of light (plane wave radiation) in a vacuum is given by two orthogonal electric fields, $u_x(t)$ and $u_y(t)$, that are both orthogonal to the direction of propagation [12]:

$$u_x(t) = E_x(t)e^{-j2\pi v_0 t} \quad u_y(t) = E_y(t)e^{-j2\pi v_0 t} \tag{2.1}$$

where $E_x(t)$ and $E_y(t)$ are complex valued functions that modulate the signal center frequency, v_0. This representation adequately describes light of any bandwidth and any phase relationship including the case where the phase between the x and y field components are partially or wholly dependent (e.g. polarized light).

The polarization state of this field can be determined by placing two specialized optical elements in its path and measuring the result. The first of these two elements, a retarder, introduces a constant phase delay, ϕ, between the x and y field

(a) A monochromatic plane wave

(b) The phase delayed plane wave

(c) The delayed, attenuated plane wave
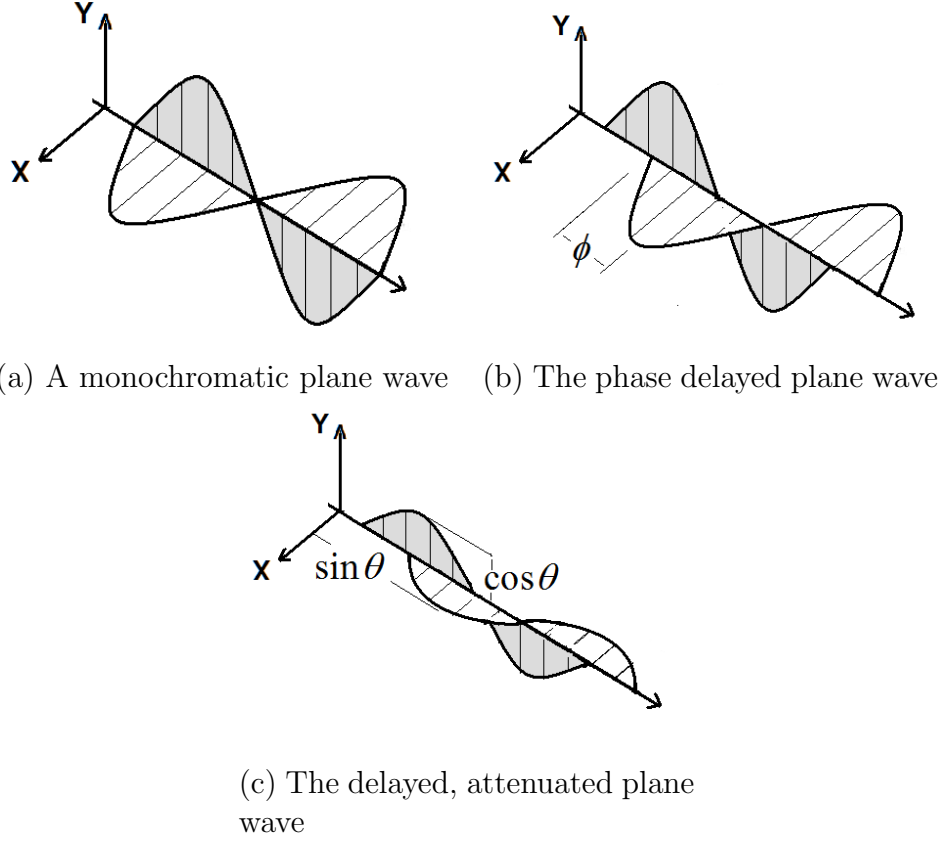
Figure 2.1: Polarization transformations on a plane wave

components (figure 2.1b). The second element, a polarizer, transmits the portion of the field along angle θ (measured with respect to the x axis) and completely attenuates the field everywhere else (figure 2.1c). The angle defined by θ is henceforth referred to as the primary transmission axis. The resulting field along the primary transmission axis is:

$$u_p(t) = u_x(t)e^{j\phi}\cos\theta + u_y(t)\sin\theta \tag{2.2}$$

The transition from (2.1) to (2.2) is derived in Appendix A.1.

Since semiconductor optical detectors respond to radiant intensity, the signal corresponding to equation (2.2) at the detector array is given by:

$$I(\theta, \phi) = \epsilon_0 c \left\langle u_p(t)u_p^*(t) \right\rangle \tag{2.3}$$

8

where u_p^* is the complex conjugate of u_p, $\langle\ldots\rangle$ represents the time average, c is the speed of light and ϵ_0 is the permittivity of free space. (Henceforth, the term $\epsilon_0 c$ will be suppressed). Because v_0 is on the order of several terrahertz, equation (2.3) is well approximated by an infinite time average. This equation can be expanded into its component parts:

$$I(\theta, \phi) = \qquad\qquad\qquad\qquad\qquad\qquad\qquad\qquad\qquad (2.4)$$
$$\Big\langle E_x(t)E_x^*(t)\cos^2\theta + E_y(t)E_y^*(t)\sin^2\theta$$
$$+ \left(E_x(t)E_y^*(t)e^{j\phi} + E_x^*(t)E_y(t)e^{-j\phi}\right)\cos\theta\sin\theta\Big\rangle,$$

After applying several well known trigonometric identities:

$$I(\theta, \phi) = \qquad\qquad\qquad\qquad\qquad\qquad\qquad\qquad\qquad (2.5)$$
$$\Big\langle E_x(t)E_x^*(t)\tfrac{1+\cos(2\theta)}{2} + E_y(t)E_y^*(t)\tfrac{1-\cos(2\theta)}{2}$$
$$+ \left(E_x(t)E_y^*(t)\left(\cos\phi + j\sin\phi\right) + E_x^*(t)E_y(t)\left(\cos\phi - j\sin\phi\right)\right)\tfrac{\sin(2\theta)}{2}\Big\rangle$$

and collecting like terms:

$$I(\theta, \phi) = \qquad\qquad\qquad\qquad\qquad\qquad\qquad\qquad\qquad (2.6)$$
$$\frac{1}{2}\Big\langle E_x(t)E_x^*(t) + E_y(t)E_y^*(t)\Big\rangle$$
$$+ \frac{1}{2}\Big\langle E_x(t)E_x^*(t) - E_y(t)E_y^*(t)\Big\rangle\cos(2\theta)$$
$$+ \frac{1}{2}\Big\langle E_x(t)E_y^*(t) + E_x^*(t)E_y(t)\Big\rangle\sin(2\theta)\cos\phi$$
$$+ \frac{j}{2}\Big\langle E_x(t)E_y^*(t) - E_x^*(t)E_y(t)\Big\rangle\sin(2\theta)\sin\phi,$$

the Stokes parameters are specified to be:

$$S_0 = \left\langle E_x(t)E_x^*(t) + E_y(t)E_y^*(t) \right\rangle \tag{2.7a}$$

$$S_1 = \left\langle E_x(t)E_x^*(t) - E_y(t)E_y^*(t) \right\rangle \tag{2.7b}$$

$$S_2 = \left\langle E_x(t)E_y^*(t) + E_x^*(t)E_y(t) \right\rangle \tag{2.7c}$$

$$S_3 = j \left\langle E_x(t)E_y^*(t) - E_x^*(t)E_y(t) \right\rangle \tag{2.7d}$$

such that the signal at the detector array is given by:

$$I(\theta, \phi) = \frac{1}{2}(S_0 + S_1 \cos 2\theta + S_2 \cos \phi \sin 2\theta + S_3 \sin \phi \sin 2\theta). \tag{2.8}$$

The Stokes parameters are therefore the intensity observables of the polarization state of electro-magnetic radiation. Because it is convenient for mathematical manipulation, the Stokes parameters are often represented in vector notation:

$$\underline{S} = \left[\begin{array}{cccc} S_0 & S_1 & S_2 & S_3 \end{array} \right]^T \tag{2.9}$$

It is important to point out that the Stokes parameters were derived with respect to a specific x and y coordinate system. As a result, agreement between the raw measurements from a pair of observers is wholly dependent on the orientation of their reference frame. If the observers agree upon a common coordinate system in advance then their measurements can be brought into agreement by applying the proper transformation (to be described later by equation (2.17)). Throughout this work, the x-axis, or primary axis, will be oriented parallel to the ground plane with the y-axis, or secondary axis, perpendicular to it. In this way, measurements on the ground or in the air will have a common reference plane.

2.2 Interpretation of the Stokes Parameters

By itself, the result in equation (2.8) provides little indication of how the Stokes parameters should be interpreted. Consequently, the purpose of this section is to introduce the relevant properties of the Stokes parameters as they pertain to this research.

Beyond the utility of describing polarization in terms of intensity, the preceding derivation of the Stokes parameters also implies a number of other important properties. The use of the analytic signal representation of polychromatic electro-magnetic radiation in equation (2.1) demonstrates that the Stokes parameters are equally well defined for radiation of any bandwidth. Consequently, the effective bandwidth limit of a Stokes measurement is determined by the experimenter's ability to impose the same phase shift and directional attenuation at every wavelength in the passband. The analytic signal representation also demonstrates that the polarization state of the superposition of two incoherent fields is given by the sum of their Stokes parameters.

The physical interpretation of each of the Stokes parameters is also of interest. Equation 2.7 reveals S_0 to be the total intensity of the incident radiation. In other words, S_0 is the intensity that would be observed if the polarizing elements were removed from the system. As a result, no other Stokes parameter can be greater in magnitude than S_0. The remaining Stokes parameters form a basis in intensity space spanning all possible polarization states. Table 2.1 summarizes the principle direction for each of the remaining Stokes parameters. Implied in this table is that fact that S_1, S_2, and S_3 are signed quantities; S_0, being the total intensity, is strictly positive.

In addition to describing the orientation of polarized radiation, the Stokes parameters also describe the extent to which the radiation is polarized. Radiation with no preferred polarization state is said to be unpolarized. If unpolarized light were to be described using equation (2.1), $E_x(t)$ and $E_y(t)$ would be rapidly varying,

11

Table 2.1: Summary of the Stokes Parameters

Normalized Stokes vector	Type of polarization
$\begin{bmatrix} 1 & 1 & 0 & 0 \end{bmatrix}^T$	linear horizontal
$\begin{bmatrix} 1 & -1 & 0 & 0 \end{bmatrix}^T$	linear vertical
$\begin{bmatrix} 1 & 0 & 1 & 0 \end{bmatrix}^T$	linear $+45^o$
$\begin{bmatrix} 1 & 0 & -1 & 0 \end{bmatrix}^T$	linear -45°
$\begin{bmatrix} 1 & 0 & 0 & 1 \end{bmatrix}^T$	right hand circular
$\begin{bmatrix} 1 & 0 & 0 & -1 \end{bmatrix}^T$	left hand circular

independent random processes. This variation is so fast that, during the period of any practical measurement, the instantaneous polarization state of the radiation would pass though every possible polarization state many times. Hecht refers to this state as randomly polarized or natural light [16] and points out, along with [42], that unpolarized light must be polychromatic to achieve this rapid variation in field amplitude. A consequence of this rapid amplitude variation is that the net effect of the retarder and polarizer pair in (2.8) is the same regardless of their orientation. By inspection, this condition requires that S_1, S_2, and S_3 be zero. Hence the Stokes vector of unpolarized light is:

$$\mathbf{S} = \begin{bmatrix} S_0 & 0 & 0 & 0 \end{bmatrix}^T \tag{2.10}$$

Partially polarized light can be considered to be the sum of equation (2.10) with another Stokes vector that represents fully polarized radiation. In all cases (total, partial, or unpolarized), the following relationship between Stokes parameters is valid:

$$S_0^2 \geqslant S_1^2 + S_2^2 + S_3^2 \tag{2.11}$$

This expression is bounded on two sides: total polarization exists when both sides of the expression are equal and radiation is said to be unpolarized when the right hand side is zero. Partial polarization occurs in every intermediate state. Equation (2.11) leads to a natural expression for the extent of polarization:

$$P = \frac{\sqrt{S_1^2 + S_2^2 + S_3^2}}{S_0} \qquad (2.12)$$

P is referred to as the degree of polarization and is bounded between zero (unpolarized light) and one (fully polarized light). When measurements of S_3 are unavailable, its value is assumed to be zero and (2.12) is referred to as the degree of *linear* polarization. Unlike the Stokes parameters themselves, P is equivalent in all reference frames.

Additionally, it is also often useful to express the angle of linear polarization, ψ, directly from the Stokes parameters:

$$\psi = \frac{1}{2} \tan^{-1} \frac{S_2}{S_1} \qquad (2.13)$$

which stems directly from that fact that:

$$\begin{aligned} S_1 &= P S_0 \cos 2\psi \\ S_2 &= P S_0 \sin 2\psi \end{aligned} \qquad (2.14)$$

Assuming linearly polarized light, this last pair of relationships allows for decomposition of I into linearly polarized and unpolarized components (with intermediate steps worked out in Appendix A.2):

$$\begin{aligned} I &= \frac{1}{2}(1-P) S_0 + \frac{1}{2} P S_0 \left(1 + \cos 2\psi \cos 2\theta + \sin 2\psi \sin 2\theta\right) \\ &= \frac{1}{2}\lambda_u + \lambda_p \cos^2(\psi - \theta) \end{aligned} \qquad (2.15)$$

where $\lambda_u = (1 - P)S_0$ is the unpolarized component of the signal and $\lambda_p = PS_0$ is the polarized component; both quantities are always greater than or equal to 0. The idea of decomposing a source into polarized and unpolarized Stokes vectors goes back to Stokes himself. A recent paper by Wolf explains the conditions under which this decomposition is viable [49]. Wolf's conditions are always met when the target is illuminated by natural light. In Chapter IV, the polarized/unpolarized irradiance representation (rather than the Stokes vector representation) is employed to ensure the statistical compatibility of the data model with the measurements.

2.3   Muller Matrix Transformations

This section introduces the mathematical operations used to describe the interaction of a Stokes vector with matter. These operators are called the Mueller matrices. Given a 4×4 Mueller matrix, T, the relationship between the incident Stokes vector, $\mathbf{S}$, and the transformed Stokes vector, $\mathbf{S}'$, is given by $\mathbf{S}' = T\mathbf{S}$. Mueller matrices have been defined for all manner of optical elements, however, this discussion will be limited to the the operators that appear in this research: the polarizer and the rotator [5].

A linear polarizer, or polarization analyzer, is an optical element that absorbs radiation at rate that is dependent on the orientation of the incident electric field. This field dependence is defined in terms of α and β which are the field transmission coefficients along the primary and secondary transmission axes as defined previously in this chapter. Since α was selected to be the transmission coefficient for radiation along the primary axis, the following convention will be adopted henceforth: $\alpha \geq \beta$.

The Mueller matrix of a linear polarizer, T, is given by:

$$T = \frac{1}{2} \begin{bmatrix} \alpha^2 + \beta^2 & \alpha^2 - \beta^2 & 0 & 0 \\ \alpha^2 - \beta^2 & \alpha^2 + \beta^2 & 0 & 0 \\ 0 & 0 & 2\alpha\beta & 0 \\ 0 & 0 & 0 & 2\alpha\beta \end{bmatrix} \tag{2.16}$$

Polarizers are the central optical element in this research and are, therefore, worthy of a more detailed discussion. α and β appear in (2.16) as second order terms (e.g α^2 or $\alpha\beta$) because the Stokes parameters have units of intensity which is proportional to the square of the mean electric field. Laboratory quality polarizers often have secondary axis transmission coefficients, β, very near zero over the bandpass of the filter. Conversely, a "polarizer" with $\alpha = \beta$ is a neutral density filter.

An optical element that rotates the electric field vector through an angle θ is called a rotator. Besides describing an actual optical element, the rotator is also a useful mathematical tool for translating Stokes parameters between reference frames. It is assumed that a rotator does not attenuate the signal in any way during rotation (i.e. it is an ideal rotator). That being said, the Mueller matrix of an attenuating rotator can be described by the matrix product of the ideal rotator with a polarizer. The ideal rotation operator is given by:

$$R(\theta) = \begin{bmatrix} 1 & 0 & 0 & 0 \\ 0 & \cos(2\theta) & \sin(2\theta) & 0 \\ 0 & -\sin(2\theta) & \cos(2\theta) & 0 \\ 0 & 0 & 0 & 1 \end{bmatrix} \tag{2.17}$$

Thus the rotation operator also provides the mathematical means to describe rotation of a polarizer by θ:

$$T(\theta) = R^{-1}(\theta) T R(\theta), \tag{2.18}$$

which is useful in practice because the problem of characterizing a polarizer in a optical system can be decoupled into the easier problems of measuring the transmission coefficients and, separately, determining the orientation of the device.

2.4 Mathematical Treatment of Polarization Imaging

The relationship between the at-aperture Stokes parameters and the intensity sensed at each channel in an imaging polarimeter is described in this section. This derivation applies to any polarimetric imager that records each channel simultaneously. The results provided here are used extensively throughout the remainder of this document.

In general, measurement of the Stokes parameters requires four intensity measurements with θ and ϕ chosen such that four unique instances of (2.8) are realized. In practice, the S_3 term is approximately zero (or, more precisely, $\phi = 0^o$) in remote sensing applications (see section 2.5). Consequently, only unique measurements are required to extract the relevant Stokes parameters and, as shown below, the optical element responsible for the phase shift in (2.2) may be dropped.

A channel model provides the transformation between the incident Stokes vector image (or simply, Stokes image), S, and intensity on the detector array, represented by I_θ. In this arrangement, θ is the orientation of the channel polarization filter measured with respect to the axis of the first channel. After this transformation is complete, only the total intensity reaching the detector, (i.e. the S_0 term after transmission through the polarizing element) is of interest. Together, the total intensities of each channel are represented by an $N \times 1$ vector, $\mathbf{I}$. Mathematically, if

$$\mathbf{S}'\left(\theta\right) = T\left(\theta\right)\mathbf{S} \qquad (2.19)$$

16

then

$$S_0'(\theta) = \frac{1}{2}\left[\left(\alpha^2 + \beta^2\right)S_0 + \left(\alpha^2 - \beta^2\right)\cos\left(2\theta\right)S_1 + \left(\alpha^2 - \beta^2\right)\sin\left(2\theta\right)S_2\right] \quad (2.20)$$

and

$$\begin{aligned}
\mathbf{I} &= \left[\begin{array}{cccc} S_0'(0) & S_0'(\theta_1) & ... & S_0'(\theta_{N-1}) \end{array}\right]^T \\
&= \left[\begin{array}{cccc} I_0 & I_{\theta 1} & ... & I_{\theta(N-1)} \end{array}\right]^T
\end{aligned} \quad (2.21)$$

where the change of variables from $S_0'(\theta_1)$ to $I_{\theta 1}$ is simply to avoid confusion later on between the Stokes vector of the at-aperture signal and the actual intensity that reaches the focal plane. The reader may compare this result to the ideal case in equation (2.8).

Using equation (2.20), a matrix transformation, M, can be defined to calculate $\mathbf{I}$ directly from $\mathbf{S}$:

$$M = \frac{1}{2}\left[\begin{array}{ccc}
\alpha_1^2 + \beta_1^2 & \left(\alpha_1^2 - \beta_1^2\right)\cos\left(2\theta_1\right) & \left(\alpha_1^2 - \beta_1^2\right)\sin\left(2\theta_1\right) \\
\vdots & \vdots & \vdots \\
\alpha_N^2 + \beta_N^2 & \left(\alpha_N^2 - \beta_N^2\right)\cos\left(2\theta_N\right) & \left(\alpha_N^2 - \beta_N^2\right)\sin\left(2\theta_N\right)
\end{array}\right] \quad (2.22)$$

such that $\mathbf{I} = M\mathbf{S}$. Note that subscripts have to been added to α and β to indicate that they can, in general, vary from polarizer to polarizer (though the convention remains that $\alpha > \beta$). Naturally, the inverse (or pseudoinverse) of M can also be used to calculate $\mathbf{S}$ directly from $\mathbf{I}$:

$$\mathbf{S} = M^{-1}\mathbf{I} \quad (2.23)$$

α and β represent a channel analyzer in a less than ideal case. That is to say, the preferred signal may be partially attenuated while, at the same time, the remaining signal is not completely suppressed. As a practical matter, the intensity equation is better represented with weights on the Stokes parameters that are determined via

17

lab calibration rather than separate measurements of α and β:

$$M = \begin{bmatrix} a_{10} & \cdots & a_{12} \\ \vdots & \ddots & \vdots \\ a_{N0} & \cdots & a_{N2} \end{bmatrix} \qquad (2.24)$$

2.5 Polarization in Remote Sensing

The purpose of this section is to provide an overview of polarimetric remote sensing in practice. Besides providing a general feel for the discipline, a primary goal of this section is to emphasize the point that naturally occurring objects with a high degree of polarization are unusual. This is the motivation for using polarization in targeting and reconnaissance.

Polarimetric imagery is highly dependent on the relative orientation of the source, target, and sensor. Referring to figure 2.2, the maximum polarization response for natural materials tends to occur when the phase angle, ρ, is near 100° [7]. Likewise, polarization is more likely to occur in the principal plane (the plane that passes through the source and target surface normal) than out of it. Broadening out at bit, stronger polarization response is more likely to occur in the forward scattering direction than in the back scattering (source side) direction.

Plane (i.e. linear) polarization is more likely to occur in nature than elliptical polarization [6,7]. Consequently, S_3 is approximately zero and, as such, is generally not measured in remote sensing applications. To help visualize this point, consider the common case of reflection at a smooth dielectric surface. Using the familiar Fresnel equations, Collett [5] shows that the Mueller matrix transformation of this physical process is identical in form to equation (2.16), the Mueller matrix of a linear polarizer. In this case, α and β are determined by the angle of incidence and the indices of refraction of the materials at their boundary. Reflection on bare metals, on the other hand, can produce elliptical polarization under the right conditions;

18
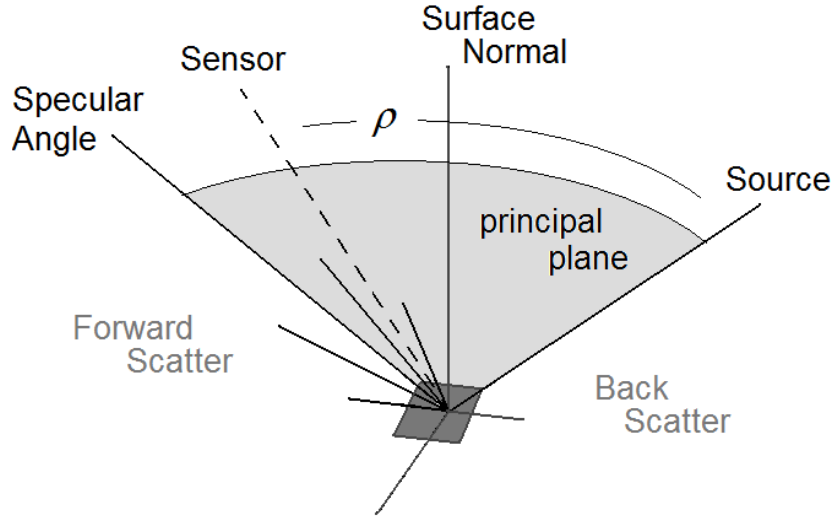
Figure 2.2: The geometry of polarimetric imaging

however, this and other birefringent materials are the exception rather than the rule.

Multiple scattering processes reduce the extent to which light is polarized [8, 16]. Multiple scattering processes in a gas or aerosol cloud can be thought of as the random absorption, re-emission, and recombination of light. For solid surfaces, especially those that are semi-transparent, multiple scattering can be thought of as the net result of many individual reflections from randomly oriented surfaces. Consequently, smooth surfaces produce higher polarization states than diffuse surfaces [6]. Scattering off of a blackbody, which is the ultimate diffuse surface, has no preferred polarization state even when illuminated with polarized light. Because man-made materials tend to have smooth, machined surfaces, they tend to reflect higher polarization states than their surroundings (water is an obvious exception to this rule).

2.6 Atmospheric Effects

The purpose of this section is to briefly introduce the effects of the atmosphere on polarimetric imaging sensors. Atmospherically induced polarization and depolar-

ization are discussed qualitatively to provide awareness of the issues. Second, the effects of the atmosphere on image formation are provided as a primer for the chapter on blind deconvolution.

Rayleigh scattering in the atmosphere produces polarized sky shine [16]. On a molecular level, this scattering induces a preferred polarization that increases with increasing angle away from the original direction of propagation. When viewed from the ground, the net effect of this molecular scattering is that the sky takes on a preferred polarization that is at a maximum along azimuths that are perpendicular to the azimuth of the sun. Simultaneously, multiple scattering due to atmospheric aerosols and haze tend to act as depolarizing agents. In remote sensing, this polarized sky shine can be reflected off of the ground and into the sensor. The most dramatic example of this effect can be found in the polarized reflection from ground targets in shadows.

In the same way that they effect sky shine, aerosols, dust, and haze also tend to diminish target polarization signatures as seen from an airborne sensor. The details of this interaction are beyond the scope of this dissertation; however, the extent of aerosol depolarization is determined by the type, depth, and number of aerosol species in the intervening atmosphere.

Though not a polarization effect per se, the atmosphere plays an important role in the formation of any incoherent image. In the absence of atmospheric effects, image formation is given by a convolution operation:

$$i(x) = [o \otimes h] (x) \tag{2.25}$$

where $h(x)$ is the sensor induced point spread function and $o(x)$ is the magnified (or minified) target image as defined by geometric optics. The summation form of (2.25) can be found at (4.1). The point spread function, even under ideal conditions, acts as a low pass filter on the geometric image and is a strong function of wavelength and

aperture diameter. When the atmosphere is introduced, uneven air temperature distributions cause spatially varying fluctuations in index of refraction which, in turn, modify the wavefront of the image reaching the sensor. The net result of this perturbation is a modified image formation equation:

$$i(x) = [o \otimes (h \otimes h_{atm})](x) \tag{2.26}$$

where h_{atm} is the atmospheric operator on the image. The grouping of the point spread function with the atmospheric operator is mathematically unnecessary but, physically, it highlights the notion that the atmosphere acts on the image in the same manner that the point spread function does.

Mathematically, the atmospherically corrupted wavefront is represented as a surface of relative wavefront phase delays, sometimes referred to as a phase screen, φ:

$$[h \otimes h_{atm}](x) = \left| \sum_u A(u) e^{i\varphi(u)} e^{-i2\pi kux} \right|^2 \tag{2.27}$$

where A is a complex function that represents the sensor aperture and any sensor dependent phase errors. For a diffraction limited system, $A(u) = 1$ for all u in the aperture and $A(u) = 0$ otherwise. An explanation of what constitutes a typical atmospheric phase screen can be found in [34].

These spatial variations in refraction index change over time. Consequently, h_{atm} has a characteristic correlation time, the duration of which is determined by the turbidity in the atmosphere. Realizations of h_{atm} are independent of each other from one correlation time to the next. When the exposure time of an image is one correlation time or less, these index variations are effectively stationary. In this regime, referred to as short exposure imaging, the dominant effect of the atmosphere is to shift the image, though this is also accompanied by other forms of degradation.

A physical model of polarization imaging has been described in this chapter. In the following two chapters, this model will be placed in a statistical context through which the contributions of this research are described.

III. Fundamental Estimation Bounds for Polarimetric Imagery

Precise channel-to-channel registration is a prerequisite for effective exploitation of passive polarimetric imagery. In this chapter, the Cramer-Rao bound is employed to determine the limits of registration precision in the presence of scene polarization diversity, channel noise, and random translational registration errors between channels. The effects of misregistration on Stokes image estimation are also explored in depth. Algorithm bias is discussed in the context of the bound, without being estimator specific. Finally, case studies are presented for polarization insensitive imagery (a special case) and linear polarization imaging systems with three and four channels. An optimum polarization channel arrangement is proposed in the context of the bound.

This work was originally published in [24]. Some additional research on the CRLB appears in Appendix B. Included in this appendix is a discussion of external measurement versus joint estimation, an interpretation of the bound using correlations, and a method for transforming the bound derived here so that it may be applied to the model in Chapter IV.

3.1 Polarimetry in the Context of the Cramer-Rao Bound

When derived from imagery, target polarization state estimates are inherently prone to both channel noise and registration errors. In this chapter, we examine the combined effects of misregistration and channel noise in the statistical framework of the CRLB.

For the present purpose, systems responsive to linear polarization are considered. Persons et al. noted that, among common means of collecting polarimetric imagery, translational and rotational registration errors between channels are most prevalent [32]. In this context, Persons and others [23, 48] have made limited attempts to characterize the effects of registration errors on polarimetric imagery us-

ing established (but polarization insensitive) registration algorithms. In addition, a recent registration study has also been conducted for the related problem of Mueller matrix imaging [14]. The results of these studies range from successful registration within stated tolerances to complete failure. Each of these efforts is a useful reference point, however, they lack the depth required to make complete comparisons across algorithms or imaging scenarios. Indeed, what is most lacking is a theoretical context in which to place these results.

The first step in providing this context is to identify the problem of estimating the polarimetric signature of a target scene as a joint estimation of the misregistration between channels and of the scene itself. Second, channel noise and misregistration are random variables, therefore, this framework must be statistical in nature. Finally, this framework must account for the influence of deterministic parameters such as channel orientation and spacing as well as polarization diversity in the scene. In this paper, the CRLB is derived for this joint estimation problem and expounded as a theoretical framework that meets all of these criteria.

The CRLB determines the lower limit on the variance of any estimator. The form of the bound is different for biased and unbiased cases. With the exception of section 3.5, this research focuses mainly on bounds for unbiased estimators. The utility of the CRLB for unbiased estimators is well described by Kay [18]; his arguments may also be tailored to this specific case: if a new estimator is devised, it is more efficient to compare it to a single bound rather than to attempt to simulate results for many different existing estimators. Alternatively, the bound can be used to determine if any existing algorithm meets this best case scenario. If no such algorithm exists, the bound can motivate the search for a better estimator. Similar studies via simulation (e.g. Monte Carlo methods) lack the theoretical foundation which the CRLB readily provides. In the present work, the bound is also shown to provide insight into the relationship between the sensor, target scene, and estimator.

Inspiration for applying this approach to the polarimetric imagery estimation problem comes from two recent works. Robinson and Milanfar [33] applied the CRLB to the problem of estimating the translational misregistration between pairs of (polarization insensitive) images in cases where the underlying scene is not estimated as a parameter. Yetik and Nehorai expanded this work to describe limits for other common misregistration issues (e.g. rotation, affine transformation) and for both feature based and intensity based registration algorithms [50]. Aside from insensitivity to polarization effects, the underlying scene assumption shared by both sets of authors obviates the need for a joint estimator and is therefore inadequate for the present purpose.

The bound derived in this work is most applicable to so called "feature matching, area-based" or "template matching" registration estimators. Common among these methods is that registration is achieved by comparing image intensities without regard to specific objects in the scene. A survey of these methods can be found in [52].

The newly derived bound determines the minimum achievable variance on estimates of the translational misregistration between channels and of the polarization state at each point in the scene. The inclusion of polarization effects and removal of the known image assumption from Robinson and Milanfar leads to a bound calculation that is computationally impractical using direct methods. As such, matrix theory is applied to the newly derived bound so that extraction of the relevant terms becomes tenable. Additionally, many well known polarization insensitive image registration algorithms exhibit bias and, in fact, some biased estimators have been shown to outperform unbiased estimators in theory and in practice. Though no such study has been conducted with polarimetric imagery, a biased estimator form of the CRLB is provided in anticipation of a similar eventual result.

The bound stands on its own as an algorithm evaluation metric, however, it may also be used in a quantitative evaluation of system design criteria. To this end,

the bound is used to determine the conditions under which it is necessary to generate the channel registration parameters externally (as opposed to including them in the estimator). Furthermore, the polarization insensitive case is actually a special case of this new bound. As a consequence, Robinson and Milanfar's bound is generalized to the case where the underlying image is unknown.

Finally, the bound can also be used to suggest optimal channel configurations. Several researchers have shown that optimum configuration (in terms of maximizing SNR) is achieved by distributing the channels evenly across all possible polarization states. In the most recent of these attempts, Tyo improved on this theory by considering the optimization problem in the presence of random channel calibration errors [46]. In perhaps the most directly related research, Tyo also showed that channels that are evenly spaced across all linear polarization states are optimal in a principal components sense [45]. The analysis presented here complements this body of research in that it demonstrates the same conclusion under different sets of assumptions and using different metrics.

3.1.1 A Quick Example. Building upon the previous section, the results of a simple laboratory experiment are presented in order to illustrate some issues regarding the registration of polarimetric imagery. The underlying assumption in many registration algorithms of the aforementioned "template matching" category (e.g. cross-correlation and variants) is that the images under test contain the same scene content but are translated and corrupted by noise. Other methods in this category, such as registration via mutual information, are perhaps more suited toward the registration of polarimetric imagery in that a statistical dependence between intensity values in each image is assumed rather than a direct correspondence in intensity. To illustrate these differences, the following example was contrived to show how a registration algorithm can utterly fail when strong polarization content violates its underlying assumptions.

Figure 3.1 contains the result of an attempt to register the three channels of an imaging polarimeter using cross-correlation. The target scene contains two fully polarized bars from a resolution target oriented such that the bars have orthogonal polarization states. The channels are spaced such that each is most sensitive to polarization at 0°, 60°, or -60°. The target polarization is rotated slightly ($\approx 10^o$) out of the sensor reference frame so that each bar appears (to a greater or lesser extent) in each channel. False color and an arrow are used to accentuate the weak signal of the top bar in the 0° channel.

(a) The misregistered 0° channel   (b) The 60° channel   (c) The -60° channel
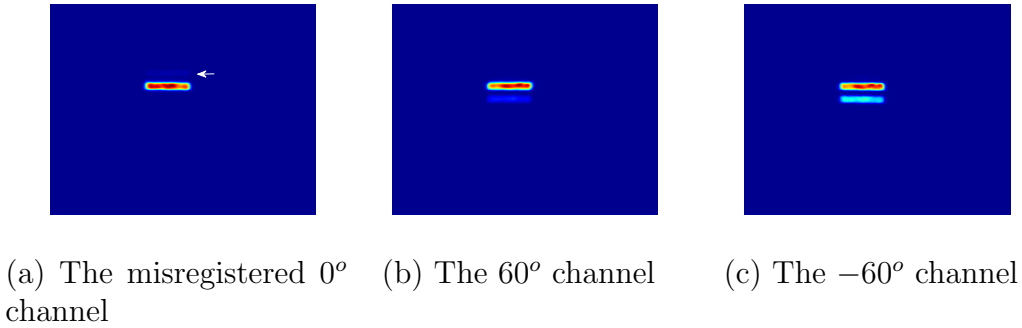
Figure 3.1: The misregistered polarimetric images.

Clearly, these three channels do not contain the same scene content which is in violation of the assumptions built into the cross-correlation algorithm. As a consequence, the bottom bar in channel 0° has been misregistered to the top bars in the 60° and -60° channels. The Stokes parameter images of this scene (figure 3.2) provide an explanation of this behavior.

Recall that S_1 and S_2 can take on negative values; the reader should interpret the dark regions in the S_1 and S_2 images in this way. This behavior is unlike S_0, which is strictly positive. The comparatively higher contrast in the S_1 image occurs because the signal in S_2 is much weaker than in S_1. If the sensor were not sensitive to polarization then the captured image in each channel would be the S_0 image.

Comparing the Stokes images in figure 3.2 with the intensity equation (2.4), the bottom bar in the 0° channel image is bright because its preferred polarization

(a) Bars in S_0 (b) Bars in S_1 (c) Bars in S_2
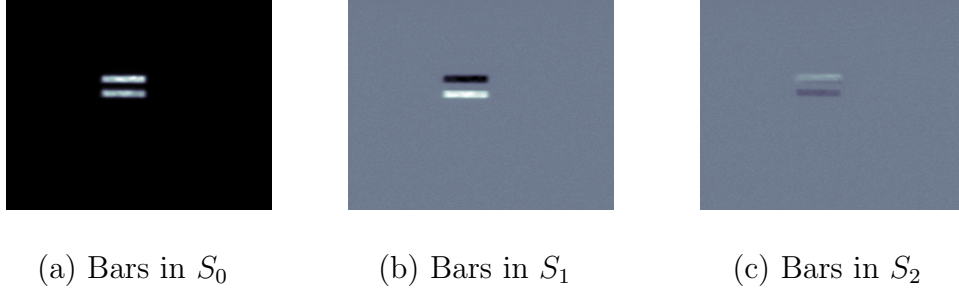
Figure 3.2: The Stokes parameter images of the bar target.

state is nearly parallel to the preferred polarization state of the channel. In this region $I \approx \frac{1}{2}(S_0 + S_1)$ where S_1 is a positive quantity. The small contribution from S_2 in this channel is ignored. The top bar is orthogonally polarized to channel 0° and in this region the form of the intensity equation is the same but S_1 is *negative*. A similar analysis could be conducted for the remaining channels but the point of this section has already been made: the phenomenology of polarization imagery is different than that of traditional intensity imagery and as such, the rules developed for image registration must be reevaluated in this new context.

3.2   Bound Definition and Data Model

In this section, the CRLB is defined and the components required to calculate the bound are identified. These components are then specified for the specific problem of calculating the bound for a joint registration and Stokes parameter estimator.

3.2.1   Definition of the Cramer-Rao Bound.   Let $\mathbf{Z}$ be a vector of random variables that is parameterized by vector θ. Define $\hat{\theta}$ to be any unbiased estimate of these parameters and $\mathbf{z}$ to be one realization of $\mathbf{Z}$. The Cramer-Rao inequality provides the lower bound on this estimator's error covariance matrix in terms of the Fisher Information Matrix (FIM), J:

$$Cov[\hat{\theta}] \geq J^{-1}, \tag{3.1}$$

28

where

$$J = -E\left[\frac{\partial}{\partial\theta}\left(\frac{\partial}{\partial\theta}L(\theta, \mathbf{z})\right)^T\right] \tag{3.2}$$

and $L(\theta, \mathbf{z})$ is the data log-likelihood function [36]. Note that $E[\ldots]$ represents the expected value operation over $\mathbf{Z}$. The minimum variance for the estimate of each parameter in θ is given by the diagonal elements of J^{-1}. When J is not positive definite the CRLB is not defined.

The concept of a log-likelihood function may require some elaboration. A likelihood function describes how the probability density for a given measurement changes as θ changes. Hence, calculation of the likelihood function requires knowledge of the probability density function for $\mathbf{Z}$, $p_\theta(\mathbf{z})$, at each measured $\mathbf{z}$. The log-likelihood function is simply the natural log of the likelihood function

$$L(\theta, \mathbf{z}) = \ln p_\theta(\mathbf{z}). \tag{3.3}$$

3.2.2 Data Model. The bound described in the previous section is defined in terms of a set of random variables $\mathbf{Z}$, parameter vector, θ, and their corresponding log-likelihood function, $L(\theta, \mathbf{z})$. The purpose of this section is to define these items for the specific problem of generating polarimetric imagery from noisy, misregistered data.

In this scenario, the collected images are realizations of $\mathbf{Z}$. Consistent with [33] and [50], the images to be registered are modeled as sampled, noisy versions of the continuously varying underlying target scene. Channel-to-channel point spread function variations are assumed to be minimal, sampling is at the Nyquist frequency or better, and noise in the scene is zero-mean, Gaussian and IID. The sampled coordinates in the (arbitrarily selected) first imaging channel, f_1, are taken to be the reference by which the remaining channels, f_2 to f_N, are specified. Mathematically, the collected image z_i for channel i at pixel $\mathbf{m_n}$ is given by:

$$z_i(\mathbf{m}_n) = f_i(\mathbf{m}_n) + \varepsilon_i(\mathbf{m}_n), \tag{3.4}$$

where $\mathbf{m}_n$ is the 2-dimensional coordinates of a given pixel in the image plane and $\varepsilon_i(\mathbf{m}_n)$ is a realization of the channel noise. The boundaries of $\mathbf{m}_n$ are determined by the region over which the collected images overlap. This overlap is assumed to be square ($1 \leq n \leq p^2$ for a $p \times p$ image). In a departure from the cited research, the image content in each channel is determined by a shared Stokes parameter mapping rather than a common intensity mapping:

$$
\begin{aligned}
f_1(\mathbf{m}_n) &= \sum_{j=0}^{2} a_{1j} S_j(\mathbf{m}_n) \\
f_i(\mathbf{m}_n) &= \sum_{j=0}^{2} a_{ij} S_j(\mathbf{m}_n - \mathbf{v}_i),
\end{aligned}
\tag{3.5}
$$

where $\mathbf{v}_i$ is the 2-dimensional translational misregistration between $\mathbf{f}_i$ and $\mathbf{f}_1$ and the parameter weights $a_{i}j$ come from equation 2.24.

For each channel, there is a one-to-one correspondence between the 2-dimensional image and a 1-dimensional vector:

$$
\begin{aligned}
\mathbf{z}_i &= [z_i(\mathbf{m}_1) \dots z_i(\mathbf{m}_{p^2})]^T \\
\mathbf{f}_i &= [f_i(\mathbf{m}_1) \dots f_i(\mathbf{m}_{p^2})]^T,
\end{aligned}
\tag{3.6}
$$

which, in turn, allows for a very compact expression of the following results.

As previously stated, the per-pixel channel noise is zero mean, IID and Gaussian; consequently, the data log-likelihood function is given by:

$$L(\theta, \mathbf{z}) = \frac{-1}{2\sigma^2} \sum_{i=1}^{N} (\mathbf{z}_i - \mathbf{f}_i)^T (\mathbf{z}_i - \mathbf{f}_i) + \xi \tag{3.7}$$

where σ^2 is the noise variance and ξ is a constant term that is not dependent on θ. It is clear from this equation that the log-likelihood is dependent on the region of overlap defined by the intersection of all images $\mathbf{f}_i$. This region of intersection is,

in turn, dependent on the relative misregistration between the images. Following the lead of Yetik, this overlap region is assumed to be constant. The efficacy of this assumption is greatest when the relative misregistration between images is small when compared to the dimensions of the overlap region; it is reasonable to assume that a multi-channel polarimeter will be operating in this regime.

Additionally, calculation of the Fisher information matrix requires an unambiguous ordering in the parameter vector θ. Since the goal is to place a bound on a joint estimator of the translational shifts between images *and* the values of the Stokes parameters at each pixel in the image, this parameter vector will be very large indeed:

$$\theta = \left[\begin{array}{cc} \mathbf{v}_2^T \ldots \mathbf{v}_N^T & \mathbf{S}_0^T \cdots \mathbf{S}_2^T \end{array} \right]^T, \tag{3.8}$$

where, analogous to the vectorized form of the channels mean images, $\mathbf{f}_i$, each Stokes parameter vector is given by:

$$\mathbf{S}_i = [S_i(\mathbf{m}_1) \ldots S_i(\mathbf{m}_{p^2})]^T. \tag{3.9}$$

Scharf [36] provides an expression for the Fisher information matrix for m observations of an multivariate, normally distributed random vector with covariance matrix, R, and mean, $\mathbf{f}$:

$$J_{ij} = m \frac{\partial \mathbf{f}^T}{\partial \theta_i} R^{-1} \frac{\partial \mathbf{f}}{\partial \theta_j} \tag{3.10}$$

As shown in (3.7), there is one observation (i.e. $m = 1$) for each of N random images. Each image i has a covariance matrix $R = \sigma^2 I$ and mean $\mathbf{f}_i$. It is straightforward to show that the FIM in this case is simply a sum of N instances of (3.10):

$$J_{ij} = \frac{1}{\sigma^2} \sum_{n=1}^{N} \frac{\partial \mathbf{f}_n^T}{\partial \theta_i} \frac{\partial \mathbf{f}_n}{\partial \theta_j} \tag{3.11}$$

3.3 Fisher Information for the Joint Estimator

The Fisher information matrix from (3.11) is developed in this section by partitioning J into submatrices. Matrix partitioning is used to exploit the inherent symmetry in the Fisher information matrix and to lend insight into the physical interpretation of J. In [35], Scharf and McWhorter show that a FIM in the form of (3.11) may be partitioned so that the subset FIMs of the parameter space may be considered individually. In this work, it is useful to partition the parameter space such the sub-FIM V describes covariances amongst the translational registration parameters and the sub-FIM S describes covariances between Stokes parameters. Define:

$$J = \begin{bmatrix} V & H^T \\ H & S \end{bmatrix} \tag{3.12}$$

where H, to use Scharf and McWhorter's parlance, relates the intercorrelations between the registration and Stokes partitions in θ. In what follows, each of V, H, and S are described in detail.

The first matrix, V, is actually the FIM for an unbiased estimator of the misregistration between channels when the underlying Stokes images are known a priori. The inverse of V is the CRLB for the registration estimator under this "known prior" condition. In the two channel polarization insensitive case, V is the bound from Robinson and Milanfar. V is composed of $(N-1)^2$ submatrices of the form:

$$V_{ij} = \begin{cases} \frac{1}{\sigma^2} \left(\frac{\partial}{\partial \mathbf{v}_i} \mathbf{f}_i^T \right) \left(\frac{\partial}{\partial \mathbf{v}_j} \mathbf{f}_j^T \right)^T & \text{if } i = j, \\ \mathbf{0}_{2 \times 2} & \text{if } i \neq j \end{cases} \tag{3.13}$$

where $\mathbf{0}_{\mathbf{2\times2}}$ is a 2×2 zero matrix. Though it does not appear explicitly in (3.12), it is also useful to define $\tilde{V}$ with the same form as V but with entries:

$$\tilde{V}_{ij} = \begin{cases} \mathbf{0}_{2\times2} & \text{if } i = j, \\ \frac{1}{\sigma^2} \left(\frac{\partial}{\partial \mathbf{v}_i} \mathbf{f}_i^T \right) \left(\frac{\partial}{\partial \mathbf{v}_j} \mathbf{f}_j^T \right)^T & \text{if } i \neq j \end{cases} \tag{3.14}$$

The role of $\tilde{V}$ will be demonstrated in the following section. For now, consider that the form of V demonstrates that errors in the estimates of the misregistration parameters are uncorrelated between channels when perfect knowledge of the underlying scene exists. When this perfect knowledge does not exist, $\tilde{V}$ will be used to describe the nature of the correlation between channels.

In the lower right quadrant of (3.12) is the $3p^2 \times 3p^2$ matrix S. Note that S is the FIM that would be used to estimate the bound on a unbiased Stokes estimator if the relative shifts between the collected images were known a priori. S divides into 3×3 submatrices of size $p^2 \times p^2$ corresponding to combinations of Stokes parameters (images).

$$S_{jk} = \frac{1}{\sigma^2} \left(I_{p^2 \times p^2} \right) \sum_{i=1}^{N} a_{ij} a_{ik} \tag{3.15}$$

where $I_{p^2 \times p^2}$ is an identity matrix of rank p^2. The block symmetry in S allows for substantial further simplification by defining the matrix:

$$C = \begin{bmatrix} c_{00} & \cdots & c_{02} \\ \vdots & \ddots & \vdots \\ c_{20} & \cdots & c_{22} \end{bmatrix}, \quad c_{jk} = \sum_{i=1}^{N} a_{ij} a_{ik} \tag{3.16}$$

in which case:

$$S = \tfrac{1}{\sigma^2} C \otimes I_{p^2 \times p^2} \tag{3.17}$$

where $\otimes$ is the Kronecker product [13]. This Kronecker product representation significantly simplifies inversion of the S matrix.

$$S^{-1} = \sigma^2 C^{-1} \otimes I_{p^2 \times p^2} \qquad (3.18)$$

In other words, the inversion of the $3p^2 \times 3p^2$ matrix S is solved by simply inverting the 3×3 matrix C.

Connecting the matrices V and S is the $3p^2 \times 2(N-1)$ matrix H. Physically, if H were the zero matrix then the bounds on the registration and Stokes parameters could be determined independently of each other. Proof of this statement is provided in section (3.4). In the process of defining H, it becomes obvious that this independence condition is never met. H is composed of $3 \times (N-1)$ readily identifiable submatrices:

$$H_{ij} = \frac{a_{ji}}{\sigma^2} \left(\frac{\partial}{\partial \mathbf{v}_j} \mathbf{f}_j^T \right)^T . \qquad (3.19)$$

Unless the collected image is constant everywhere (i.e. the derivative of the image is zero everywhere) then H is non-zero and the covariance bounds must be determined jointly. More on the relationship between H, V and $\tilde{V}$ can be found in Appendix B.1.

3.4   Bound Derivation

The Fisher information matrix has been shown to contain $[2(N-1) + 3p^2] \times [2(N-1) + 3p^2]$ entries. To put the enormity of this matrix into perspective, consider the bound calculation for a four channel polarimeter used to estimate the first three Stokes parameters. Assuming a 512×512 overlap region, the corresponding FIM has approximately 6.18×10^{11} entries. Inversion of such a large matrix is prohibitive. In this section, the partitioning of the Fisher information matrix from the previous section is exploited to make this inversion problem tractable.

3.4.1 Block Matrix Inversion. As previously discussed, the variance bound for each parameter in θ is given by the diagonal entries of J^{-1}. Consequently, computational expense can be significantly reduced by avoiding the unnecessary calculation of many of the off diagonal terms in the inverse. A trivial rearrangement of the partitioned inverse of a block matrix in [15] provides the following:

$$B_v = \left(V - H^T S^{-1} H\right)^{-1} \tag{3.20}$$

and

$$B_S = S^{-1} + S^{-1} \left(H B_v H^T\right) S^{-1} \tag{3.21}$$

where B_v and B_S, which are submatrices of J^{-1}, identify the bounding covariance matrices on the shift parameters and Stokes images. As an aside, if $H = \mathbf{0}$ then $B_v = V^{-1}$ and $B_S = S^{-1}$, thus demonstrating the physical interpretation of H put forth in the previous section.

Equations (3.20) and (3.21) readily demonstrate how uncertainty in the misregistration between channels impacts uncertainty in the Stokes image estimates and vice versa. Similar to the $H = \mathbf{0}$ case, if the underlying Stokes images are known perfectly then the CRLB on the misregistration estimates would simply be $B_v = V^{-1}$. Likewise, if perfect knowledge of the registration parameters existed then $B_S = S^{-1}$. Consequently, it is clear that B_v and B_S are always larger than V^{-1} and S^{-1} in the absence of perfect knowledge.

3.4.2 Simplified Registration Parameter Bound. Matrix B_v is addressed first because it is required to calculate B_S. As preliminary work, note that:

$$H^T S^{-1} H = \sigma^2 H^T \left(C^{-1} \otimes I_{p^2 \times p^2}\right) H. \tag{3.22}$$

Consequently, $H^T S^{-1} H$ can itself be partitioned into a matrix, D, such that:

$$D_{hk} = \sigma^2 \sum_{i=0}^{2} \sum_{j=0}^{2} C_{ij}^{-1} H_{ih}^T H_{jk}. \tag{3.23}$$

which provides the opportunity to profitably apply equations (B.1) and (B.2) from Appendix B.1:

$$D_{hk} = \begin{cases} \sum_{i=0}^{2} \sum_{j=0}^{2} C_{ij}^{-1} a_{hi} a_{hj} V_{hh} & \text{if } h = k, \\ \sum_{i=0}^{2} \sum_{j=0}^{2} C_{ij}^{-1} a_{hi} a_{kj} \tilde{V}_{hk} & \text{if } h \neq k \end{cases} \tag{3.24}$$

Furthermore, it is mathematically expedient to add and then subtract V into the definition of D such that:

$$D = -W_v \bullet \left(V + \tilde{V} \right) + V \tag{3.25}$$

where $\bullet$ is the Hadamard product and all sensor dependent terms have been bundled into:

$$W_v = \left(\mathbf{I}_{(N-1) \times (N-1)} - A C^{-T} A^T \right) \otimes \mathbf{1}_{2 \times 2} \tag{3.26}$$

The matrix A is formed of the 2 to N rows of M, the matrix of per channel Stokes weighting parameters from (2.24). The bound on the shift estimates can now be expressed concisely:

$$B_v = (V - D)^{-1} = \left[W_v \bullet \left(V + \tilde{V} \right) \right]^{-1} \tag{3.27}$$

As anticipated, $\tilde{V}$ has indeed provided the constituents for the cross-covariance terms in B_v.

3.4.3 Simplified Stokes Parameter Bound. The impetus behind much of the preceding section was to avoid having to manipulate an unwieldy Fisher information matrix directly while still achieving the CRLB on the registration parameters. The

goal in this section is to do the same for the bound on the Stokes image estimators, B_S. We propose that the variance bound on the Stokes parameter estimate for any one pixel in the image is of less interest than the average bound across the image. In turn, this calculation is significantly simplified by applying properties of the trace and of the Kronecker product as shown in Appendix B.2, where the bound is derived in detail. What follows are the highlights of this derivation.

Define B_{Si}, the covariance matrix for an estimator of Stokes image $\mathbf{S}_i$, to be a submatrix of B_S. Equivalently, let Γ_i be the submatrix of S corresponding to the Stokes image $\mathbf{S}_i$:

$$\Gamma_i^{-1} = \sigma^2 C_{ii}^{-1} \otimes \mathbf{I}_{p^2 \times p^2} \tag{3.28}$$

and define:

$$\Phi_i^{-1} = \sigma^2 C_i^{-1} \otimes \mathbf{I}_{p^2 \times p^2} \tag{3.29}$$

where

$$C_i^{-1} = \begin{bmatrix} C_{i0}^{-1} & \cdots & C_{i2}^{-1} \end{bmatrix} \tag{3.30}$$

then the average bound for Stokes image $\mathbf{S}_i$ is defined to be:

$$\langle B_{Si} \rangle = \frac{1}{p^2} tr\left(B_{Si} \right) \tag{3.31}$$

Expanded out, the trace term is:

$$tr\left(B_{Si} \right) = tr\left(\Gamma_i^{-1} \right) + tr\left[\Phi_i^{-1} \left(H B_v H^T \right) \Phi_i^{-T} \right] \tag{3.32}$$

and because of the implicit symmetry of V and $\tilde{V}$:

$$\begin{aligned} tr\left[\Phi_i^{-1} \left(H B_v H^T \right) \Phi_i^{-T} \right] &= \sigma^2 vec\left[W_{Si} \bullet \left(V + \tilde{V} \right) \right]^T vec\left(B_v \right) \\ &= \sigma^2 tr\left[W_{Si} \bullet \left(V + \tilde{V} \right) B_v \right] \end{aligned} \tag{3.33}$$

where

$$W_{Si} = A \left(C_i^{-T} C_i^{-1} \right) A^T \otimes \mathbf{1}_{2 \times 2} \tag{3.34}$$

this result can be folded back into (3.31) to produce:

$$\langle B_{Si} \rangle = \sigma^2 C_{ii}^{-1} + \frac{\sigma^2}{p^2} tr \left[W_{Si} \bullet \left(V + \tilde{V} \right) B_v \right] \tag{3.35}$$

Hence, substantial simplification of the bound calculation is achieved. The similarities between $\langle B_{Si} \rangle$ and B_v are clear. The terms in B_S that are not contained in B_{Si} can be ignored because they do not influence the trace. Also, it is interesting to note how the sensor itself (realized by W_{Si} and W_v in B_v) plays opposing roles in equation (3.35) analogous to multiplication and division if this were a purely scalar case.

3.5   Biased Estimators

A study of estimator bias in the registration of polarimetric imagery has not been addressed in the literature. However, there are several well known examples of estimator bias in traditional, polarization insensitive registration algorithms. In anticipation of this future work, what follows is a discussion of incorporating bias into the results from sections 3.4.2 and 3.4.3.

According to Scharf [36], the CRLB on the covariance matrix of a biased estimator is given by:

$$Cov \left[\hat{\theta} \right] \geq \Delta^T J^{-1} \Delta \tag{3.36}$$

where, J, is the Fisher information matrix (identical to the unbiased case), $\hat{\theta}$ is the estimate of θ and

$$\Delta = \frac{\partial}{\partial \theta} E \left[\hat{\theta} \right]^T \tag{3.37}$$

is the partial derivative of the expected value of the estimator. The expected value of $\hat{\theta}$ is estimator specific (i.e. registration algorithm specific) and, furthermore,

the CRLB of a biased estimator may be higher or lower than that of an unbiased estimator. Note that in the unbiased case, $\Delta = \mathbf{I}$ and equation (3.36) reduces to equation (3.1). In what follows, a specific partition of Δ is defined via subscript. For instance, Δ_v refers to a partition of Δ dealing strictly with estimates of the registration parameters whereas Δ_{S_0} refers to estimates of the Stokes image S_0.

The biased estimator bound for the registration parameters, $\tilde{B}_v$, is easily achieved by combining (3.27) with (3.36):

$$\tilde{B}_v = \Delta_v^T \left[W_v \bullet \left(V + \tilde{V} \right) \right]^{-1} \Delta_v \tag{3.38}$$

which is made possible by exchanging J^{-1} in (3.36) with its submatrix B_v (from the unbiased case). In what appears to be a very small step, this equation shows that the CRLB can be decomposed into an scene specific part, $V + \tilde{V}$, a sensor specific part W_v, and an estimator specific part, Δ_v. This separation may not be complete in that the channel spacing effects $V + \tilde{V}$ and, more than likely, bias in the estimator will be to some extent affected by scene polarimetric content.

Without the context of a specific registration algorithm, interpretation of the biased CRLB for a Stokes estimator is less straightforward. Combining (3.32) with (3.36) reveals that the trace on the biased Stokes bound is:

$$tr \left(\tilde{B}_{Si} \right) = tr \left(\Delta_{Si}^T \Gamma_i^{-1} \Delta_{Si} + \Delta_{Si}^T \Phi_i^{-1} \left(H B_v H^T \right) \Phi_i^{-T} \Delta_{Si} \right) \tag{3.39}$$

which may be reduced somewhat by substituting $\Delta_{Si}^T \Phi_i^{-1}$ in for Φ_i^{-1} in Appendix B.2 and noting that:

$$\Phi_i^{-T} \Delta_{Si} \Delta_{Si}^T \Phi_i^{-1} = \sigma^4 C_i^{-T} C_i^{-1} \otimes \Delta_{Si} \Delta_{Si}^T \tag{3.40}$$

resulting in:

$$tr\left(\tilde{B}_{Si}\right) = tr(\Delta_{Si}^{T}\Gamma_{i}^{-1}\Delta_{Si}) + \sigma^{4}tr\left(H^{T}\left(C_{i}^{-T}C_{i}^{-1} \otimes \Delta_{Si}\Delta_{Si}^{T}\right)HB_{v}\right) \qquad (3.41)$$

which is, if not quite as simple as the registration parameter case, certainly more computationally efficient than directly inverting the FIM. In terms of interpretation, the trace is composed of the sum of two terms, the first of which depends only on the estimator and the sensor. Later, in section 3.6.2, it is shown that the equivalent to this term in the unbiased case dominates the solution to the problem of an optimum channel spacing. It will be left to future work to show that this is the case for specific biased estimators.

Though there are currently no studies of bias in the registration of polarimetric imagery, the interested reader will be well served by referring to [33] for an in depth discussion of bias in gradient based registration algorithms for polarization insensitive imagery.

3.6 Example Bound Calculations

In the examples that follow, an unbiased estimator is assumed throughout.

3.6.1 Bounds on Polarization Insensitive Imagery. Bounds on polarization insensitive imagery are presented here as a special case of the results derived in section 3.4. This case serves as both a practical example of how the CRLB can be applied effectively and as a bridge between this work and the work of Robinson and Milanfar.

We seek the bound on a joint estimator of a scene and the registration parameters amongst N noisy samples of this image. Recall that S_0 represents total scene intensity, therefore, S_0 is the only Stokes image of interest. In this scenario, the matrix in equation (3.16) reduces to a scalar, $C = N$, because there is only one parameter per pixel to be estimated. The channel transmission coefficient, a_{i0}, is

40

assumed to be unity for each channel. In that case, $M = \mathbf{1}_{(\mathbf{N-1})\times\mathbf{1}}$. Therefore, each of W_v and W_{S_0} are the $2(N-1) \times 2(N-1)$ matrices:

$$(W_v)_{ij} = \begin{cases} 1 - \frac{1}{N} & \text{if } i = j, \\ -\frac{1}{N} & \text{if } i \neq j \end{cases} \tag{3.42}$$

and

$$W_{S_0} = \frac{\sigma^2}{N^2} \otimes \mathbf{1}_{2(N-1)\times 2(N-1)}. \tag{3.43}$$

To reiterate an important point, both V and $\tilde{V}$ are image dependent. That being said, the overall bound's behavior with increasing N can be predicted by the behavior of W_v and W_{S_0} for any image. Equation (3.42) shows that $B_v = 2V^{-1}$ in the two channel case and $B_v = V^{-1}$ in the limit of N. Essentially, the $\tilde{V}$ matrix is suppressed by the $1/N$ terms in W_v as N increases. These suppressed terms represent the decreasing influence of each individual image as the true underlying image emerges. In this limit, the bound parameters for each image asymptotically achieve the bound predicted by Robinson and Milanfar in their 2004 work. Assuming a few images do not differ substantially from the rest of the ensemble (e.g. due to a large translational error or parallax) then the results follow a $\left(1 - \frac{1}{N}\right)^{-1}$ progression.

Likewise, the progression of the estimated image toward the true image can be ascertained from the behavior of $\langle B_{S_0} \rangle$. Again, we consider the endpoints. In the two channel case:

$$\langle B_{S_0} \rangle|_{N=2} = \frac{\sigma^2}{p^2} + \frac{\sigma^2}{2} \tag{3.44}$$

and the large N case:

$$\langle B_{S_0} \rangle|_{N\rightarrow large} = \frac{\sigma^2}{p^2} \frac{2(N-1)}{N^2} + \frac{\sigma^2}{N} \tag{3.45}$$

It would appear that the behavior of the this bound is dominated by $\frac{\sigma^2}{N}$. As shown in figure 3.3, the broad applicability of the preceding observations can be verified experimentally.

Twenty realizations of two test images, each with unique spatial characteristics, are generated with white Gaussian noise statistics and an uniformly distributed random shift error between ± 5 pixels in any direction. The scene average signal-to-noise ratio is 3. The bound on the average pixel value estimates, $\langle B_{S_0} \rangle$, and the average misregistration bound (i.e. $tr(B_v)/(N-1)$) are normalized and plotted against the number of frames, N. Normalization is carried out to illustrate the $\frac{1}{N}$ behavior of the intensity variance bound and the $\left(1 - \frac{1}{N}\right)^{-1}$ behavior of the shift estimator bound. For comparison, each of these predicted curves are shown as a red dashed line underneath the data.

The expected behavior of the bound with increasing N is confirmed for these disparate examples. The deviation of average registration parameter bound in the G.G. Stokes image from the expected trend demonstrates the slight influence of changes in image overlap area on the results.

3.6.2 The Four Channel, Three Stokes Case. Unambiguous determination of a linear polarization state requires three or more polarization imaging channels. In the following section, we demonstrate that a minimum of four channels is required for the joint registration and Stokes parameter estimation problem. In this section, example Cramer-Rao bounds are calculated as a function of polarization channel orientation for three distinct imaging scenarios. The purpose of this exercise is to illustrate the effects of channel orientation on the CRLB and, in this context, to describe the optimum channel configuration.

Along with scene content, the orientation of each polarization channel can be expected to affect the bound of the estimated Stokes parameters. As discussed in the introduction, Tyo has shown that an optimum combination of polarization channels

(a) George Gabriel Stokes
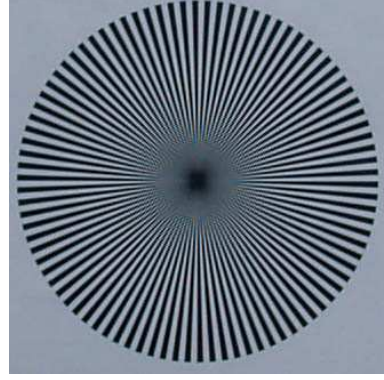
(b) Geometric pattern
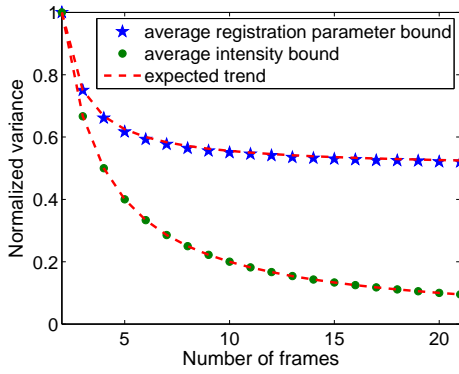
(c) G.G. Stokes portrait normalized bounds
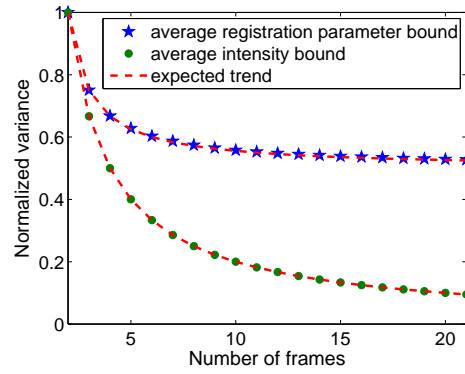
(d) Geometric pattern normalized bounds

Figure 3.3: Polarization insensitive imagery and its estimation bounds

exists in a principal components sense for monochromatic, fully polarized radiation that is uniformly distributed over all states of linear polarization (e.g. not image specific) [45]. Tyo's optimum combination of channels, in the four channel case, corresponds to a spacing of 45°. Since his work was brought about from different assumptions and desired outcomes, it is of interest to compare this result to the optimum configuration as defined by the CRLB.

Examples from three real-world polarization imagers are selected to represent the diversity of polarization imaging scenarios. The first case is the bar target from figure 3.2 which was collected in the lab using a three channel imaging polarimeter in the visible regime. The ultraviolet astronomical data of galaxy Markarian 3 comes

from the (now decommissioned) Faint Object Camera that was aboard the Hubble Space telescope until 2002. Finally, the machine vision example of a printed circuit board is taken from laboratory data collected in the visible regime (using a different polarimeter than in the the bar target case). The Stokes images for the Markarian 3 and PC board cases are shown in the following figures.

(a) Markarian 3 in S_0 (b) Markarian 3 in S_1 (c) Markarian 3 in S_2

Figure 3.4: The Markarian 3 test scene

(a) PC board in S_0 (b) PC board in S_1 (c) PC board in S_2

Figure 3.5: The printed circuit board test scene

The bound characteristics are determined by varying the angular spacing between polarization elements in one degree increments. The separation angle between channels is measured with respect to the first channel, which is held fixed. Each channel is evenly spaced and, in the plots that follow, this channel spacing is used to index the bound results. For example, the reader can infer that a channel spacing of 5° corresponds to an orientation of 5°, 10°, and 15° for the second, third, and fourth channels with respect to the first. Figure (3.6) shows the average bound on

the Stokes parameters for each of the three test cases. Each plot is normalized by σ^{-2} since it may be divided out of equation (3.35).

As should be expected, the largest variances in Stokes image estimates occur when the polarization channels are closely spaced. Somewhat less expected is the observation that scene content appears to have little influence on individual results for the Stokes estimator in terms of the overall trends. Though there are small scale differences, the Stokes parameter bounds for all images closely follow the evolution of C_{ii}^{-1} with increasing channel spacing. This result is significant for two reasons. First, there appears to be global agreement as to which channel spacing is most preferable, at least for the test cases sampled here. Second, it would appear that each B_{Si} is very well approximated by direct interrogation of S^{-1}, at least in an average sense. In other words, the Stokes parameter bounds are effectively scene independent with respect to channel spacing. Recall that S^{-1} is, by itself, the CRLB on the Stokes estimates when perfect knowledge of the misregistration parameters is available, consequently, these observations apply equally to that scenario.

The bound for the S_1 and S_2 estimates meet at Tyo's predicted optimal channel spacing of 45°, however, S_1 has a minimum bound at a somewhat closer channel spacing. Consequently, there is no global minimum bound for all Stokes parameters. Rather, the 45° spacing is the point where there is no preferred parameter. This point is significant because, as stated previously, the Stokes parameters are defined with respect to some coordinate system and, as this system changes in relation to the target (e.g. through camera motion) then scene content can shift between S_1 and S_2. With this qualifier, a 45° channel spacing can be said to be optimal for a four channel system.

Figure (3.6) also contains a plot of the average registration parameter bound for each of the three channels. As before, σ^2 has been normalized out. Unlike the bounds on the Stokes parameters, these bounds depend both on scene content and channel orientation. Consistent with the Robinson and Milanfar analysis of V in

the polarization insensitive two channel case, the difference in bound magnitude correlates with the amount of high spatial frequency content in the test images. The PC board image, with its multi-faceted geometric features, generates the lowest bound while the galaxy Markarian 3, which has largely diffuse features, generates the highest bound.

(a) Markarian 3 Stokes bounds

(b) Bar target Stokes bounds

(c) PC board Stokes bounds

(d) Average registration parameter bounds for all scenes
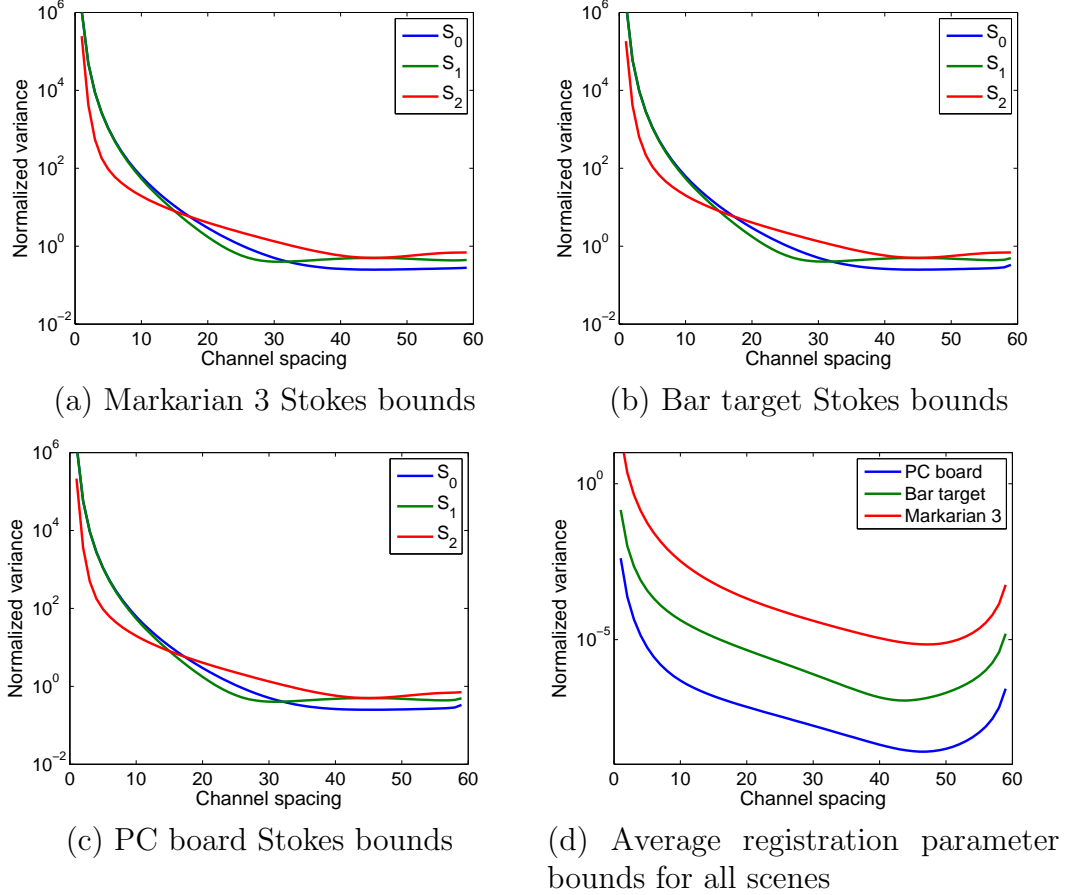
Figure 3.6: Bound results for the four channel case

3.6.3   The Three Channel, Three Stokes Case.   The three channel case is important because it is the minimum number of channels required to completely describe linear polarization (i.e. S_0, S_1, S_2). The interested reader may easily verify this three channel prerequisite for themselves by attempting to calculate B_S with only two channels. Three channel polarimeters are also common in practice; all

examples in the previous section were originally collected by different three channel systems. In this section, the three channel polarimeter is examined from a joint estimation perspective.

First, consider the bound matrix B_v for some combination of three polarimeter channels represented by weight matrix A. Immediately, a mathematical difficulty arises:

$$W_v = \mathbf{0_{4 \times 4}} \tag{3.46}$$

in which case equation (3.27) is uninvertible or, in other words, the CRLB for the joint estimator (biased or unbiased) is infinity.

At first glance, the result in (3.46) appears to be inconsistent with the fact that, three channel polarimeters are routinely employed in practice. The key difference, however, is that the data from these systems are not reduced using *joint* estimation algorithms. Rather, shift estimation and Stokes estimation are treated as separate problems. In other words, external measurement of the registration parameters is always required in the three channel case.

In terrestrial remote sensing applications, it is often the case that much of the scene is dominated by weakly polarized content (an obvious exception is a target scene composed over the water). In this case, the channel-to-channel registration problem for each pair of images is well approximated by the two channel polarization insensitive case described in section (3.6.1).

Assuming external measurement of the registration parameters by whatever means, there is likely a regime where S^{-1} will dominate equation (3.21), analogous to the four channel joint estimation examples. Following the prescribed method in the previous section, the diagonal terms in J_S^{-1} will be jointly minimized for S_1 and S_2 when the angular separation between channels is 60°. In this sense, the CRLB for the Stokes estimates can be compared across the three and four channel cases.

Table 3.1: Average bounds on Stokes parameter estimates in the S^{-1} dominant regime

Parameter	3-channel case	4-channel case
S_0	$\frac{1}{3}\sigma^2$	$\frac{1}{4}\sigma^2$
S_1	$\frac{2}{3}\sigma^2$	$\frac{1}{2}\sigma^2$
S_2	$\frac{2}{3}\sigma^2$	$\frac{1}{2}\sigma^2$

Note from table 3.6.3 that S_0 follows the $\frac{1}{N}$ pattern established for the polarization insensitive case while S_1 and S_2 go by $\frac{2}{N}$.

3.7 Chapter Summary

In this chapter, the Cramer-Rao lower bound is derived for the problem of jointly estimating Stokes images and random misregistration parameters in the presence of channel noise. Direct inversion of the prohibitively large Fisher information matrix is bypassed by applying matrix theory to express the resulting bounds in a tractable form. The effects of estimator bias on the bound are discussed up to the point where it becomes necessary to identify a specific estimator. The bound is then used to describe three and four channel polarimetric imaging systems as well as the special case of registering N polarization insensitive images. The bound itself is a useful evaluation metric because it incorporates both sensor and estimation algorithm effects and can be used to describe these effects theoretically in a way that pure simulation can not. In addition, the following general conclusions can be drawn from the results:

- The minimum achievable estimator variance is scene and channel orientation dependent in the unbiased case. The estimator itself also effects the bound in the biased case.

- The bounds on the registration and Stokes parameters are dependent.

Furthermore, specific conclusions can be drawn from the section 3.6 case studies:

- In the polarization insensitive case, the CRLB derived by Robinson and Milanfar [33] is shown to be the asymptotic limit of the joint estimation bound as the number of frames approach infinity.

- In the three channel case, the CRLB for any joint estimator is infinity. Consequently, the registration parameters and Stokes images must be estimated separately.

- The form of the bound suggests that the optimum channel spacing is 60° and 45° respectively in the three and four channel cases. Optimum, in this context, refers to a joint minimum bound for S_1 and S_2. These arrangements do not guarantee that the bound on the registration estimator is minimized.

IV. Blind Deconvolution of Polarimetric Imagery

A maximum likelihood blind deconvolution algorithm is derived for incoherent polarimetric imagery using expectation maximization. In this approach, the unpolarized and fully polarized components of the scene are estimated along with the corresponding angles of polarization and channel point spread functions. The scene state of linear polarization is determined unambiguously using this parameterization. Results are demonstrated using laboratory data and simulation.

The preponderance of this chapter was originally published in [25]. In an expansion of this original work, sections 4.6 and 4.7 include an algorithm comparison and an attempt to better understand polarization angle estimation, both in the context of simulation. To bridge this chapter with the last, the Cramer-Rao bound for the ML estimator derived here can be found in the appendix, section B.5.

4.1 Polarimetric Image Restoration

However polarization information is conveyed, it is generally the result of a fusion of multiple latent images, each collected through a different polarization analyzer. In the presence of strong polarization features, these channels may generate images with substantial content variations between them. In this sense, the fusion of polarization imagery is similar to fusion across spectral regimes or perhaps among medical imaging modalities. To some extent, these analogies are imperfect because the relationship between channels in polarimetric imagery can be accurately modeled without knowledge of the target itself.

Like all imaging systems, the sensor limits the ability of the image to faithfully reproduce the intended target. These limits are manifested by noise and by the blurring effects of the channel point spread function. Additionally, it is often the case in remote sensing that the response of each channel varies due to the wavefront corrupting effects of the atmosphere. The problem of estimating the true target image

in the presence of unknown atmospheric corruption is known as blind deconvolution and has been studied extensively in the traditional imaging (i.e. polarization insensitive) case. An excellent overview of the discipline can be found in references [21, 22]; however, there are also more recent examples in the literature. In this paper we derive and test a maximum likelihood blind deconvolution algorithm for incoherent polarimetric imagery.

The proposed blind deconvolution algorithm is a generalization of the work of Schulz on multiframe blind deconvolution [38, 39] in the polarization insensitive case. In the present case, the joint-likelihood of the combined polarization channels is parameterized by the linear polarization state of the underlying scene and the channel point spread functions. This likelihood function is recast using the generalized expectation maximization (GEM) algorithm which, in turn, decouples the estimators amongst the parameters of interest.

Before proceeding, it is worth mentioning some other recent advances in polarization imagery estimation. In [51], a maximum a posteriori Stokes parameter estimator is derived and tested. Unlike the present case, the estimator is not intended to account for sensor or atmospheric point spread function (PSF) variations between imaging channels and, furthermore, relies up prior knowledge that is not assumed here. In his dissertation, Strong derives a blind maximum likelihood estimator of a target scene and a lumped polarization parameter [43]. This estimator combines observations from one polarization channel and one polarization insensitive channel and is loosely based on an expectation maximization approach. This differs significantly from the present work in that, here, the polarization state of the target scene is determined without ambiguity in degree or angle of polarization and in that any number of polarization channels may be combined to improve the estimate.

The chapter begins with a brief introduction to the GEM algorithm and a mathematically description of polarized light in section 4.2. In section 4.3, the polarization image estimator is derived and the case is made for estimating channel

51

point spread functions using Schulz's original method. For completeness, a brief overview of the PSF estimator is also included. Finally, the algorithm is tested using a laboratory imaging polarimeter in section 4.4.

4.2 Preliminary Notes

The purpose of this section is to introduce and motivate the use of the GEM algorithm for this estimation problem. In addition, a model is produced for polarized radiation that best compliments the GEM approach.

4.2.1 The GEM Algorithm.

In maximum likelihood (ML) estimation, one or more parameters of an assumed probability distribution for variable X are estimated directly from observations of X. The generalized expectation maximization algorithm is an iterative method for achieving an ML estimate. The present problem is well served by the GEM approach because an ML approach that directly estimates the desired parameters is impractical to implement. The seminal paper on the GEM algorithm is found at [1] and a very readable overview at [29]. In what follows, some basic steps are outlined to the extent necessary to understand the GEM implementation in the sections that follow.

As the name suggests, the GEM algorithm consists of two parts: an expectation step and a maximization step. In the build up to the expectation step, the measured data (henceforth referred to as the incomplete data) is represented as the aggregate of some underlying random variables (the complete data). The complete data may or may not have physical significance but, in every case, the aggregated complete data have the same probability distribution as the incomplete data. In the expectation step (E-step), the expected value of the likelihood of the complete data is determined when conditioned upon both the incomplete data and the estimate from the previous iteration. In the maximization step (M-step), each estimated parameter is selected such that it either maximizes the expected likelihood (i.e. the

52

result from the E-step) or at least increases its value over the previous iteration. The algorithm is stopped when the latest iteration of the algorithm meets some predetermined stopping criteria.

In section 4.3, Schulz's complete data for the polarization insensitive case is decomposed into polarized and unpolarized constituents for each polarimeter imaging channel. As such, the Poisson distributed incomplete data (photons counted at the detector array) are found to be the sum of many independent Poisson distributed polarized and unpolarized parts. In the following section, the physical model for this decomposition is described.

4.3 Estimator Derivation

In this section, the broad concepts introduced in section 4.2.1 are applied to the polarimetric blind deconvolution problem. The section begins with the incomplete data log likelihood to demonstrate the difficulties encountered when attempting to achieve an ML estimate directly from the probability distribution of the measured data.

4.3.1 The Complete Data Log-likelihood.
The incomplete data are the collected images themselves, d. Define $d_c(y)$ to be an element in d where the subscript c specifies the channel in question and y specifies a location in the imaging space. Each $d_c(y)$ is modeled as an independent Poisson random variable. Using the same convention, the mean of d is i which is a function of the scene, o, and the collection of channel point spread functions, h. Consequently, the mean of each $d_c(y)$ is $i_c(y)$, given by the convolution of o_c and h_c:

$$i_c(y) = \sum_x o_c(x) h_c(y - x) \tag{4.1}$$

which is simply the summation form of equation (2.25). To capture the variation between channels due to scene polarization content, each o_c is decomposed into its

53

polarized constituents:

$$o_c(x) = \frac{1}{2}\lambda_u(x) + \lambda_p(x)\cos^2\left(\alpha(x) - \theta_c\right) \tag{4.2}$$

Equation (4.2) demonstrates how polarization information is shared between channels in the log-likelihood. Now we postulate a formulation for the polarized and unpolarized components of the complete data, $\tilde{d}_{uc}(y,x)$ and $\tilde{d}_{pc}(y,x)$, which will alleviate the mathematical difficulties incurred by maximizing the likelihood of $d_c(y)$ directly. To meet the requirements of the GEM algorithm, the complete data are also Poisson random variables such that:

$$d_c(y) = \sum_x \tilde{d}_{uc}(y,x) + \sum_x \tilde{d}_{pc}(y,x) \tag{4.3}$$

and

$$E\left[\tilde{d}_{uc}(y,x)\right] = \frac{1}{2}\lambda_u(x)h_c\left(y - x\right) \tag{4.4a}$$

$$E\left[\tilde{d}_{pc}(y,x)\right] = \lambda_p(x)\cos^2\left(\alpha(x) - \theta_c\right)h_c\left(y - x\right) \tag{4.4b}$$

Hence the complete data log-likelihood, L^{CD}, is:

$$L^{CD}\left(\lambda_u, \lambda_p, \alpha, h\right) = \sum_c \sum_y \sum_x \left\{\tilde{d}_{uc}(y,x)\ln\left[\frac{1}{2}\lambda_u(x)h_c\left(y - x\right)\right] - \frac{1}{2}\lambda_u(x)h_c\left(y - x\right)\right\} +$$

$$\sum_c \sum_y \sum_x \left\{\tilde{d}_{pc}(y,x)\ln\left[\lambda_p(x)\cos^2\left(\alpha(x) - \theta_c\right)h_c\left(y - x\right)\right] - \lambda_p(x)\cos^2\left(\alpha(x) - \theta_c\right)h_c\left(y - x\right)\right\} \tag{4.5}$$

plus a term that does not depend on λ_u, λ_p, α or h_c and is therefore of no consequence to the estimator.

4.3.2   The E-step.   The expectation step, or E-step, defines the objective function that is to be maximized by careful selection of arguments in the following

54

maximization step. Consequently, there is an obvious analogy between the role of this objective function and that of the likelihood function in traditional maximum likelihood estimation. For iteration $n + 1$, this objective function, Q^{n+1}, is the conditional expectation of the complete data log likelihood. This expected value over the complete data is conditioned upon the measurements (i.e. the incomplete data) and the most recent estimates of h, λ_u, λ_p and α:

$$Q^{n+1}\left(\lambda_u, \lambda_p, \alpha, h\right) = E\left[L^{CD}\left(\lambda_u, \lambda_p, \alpha, h\right) | d, \lambda_u^n, \lambda_p^n, \alpha^n, h^n\right] \qquad (4.6)$$

and, for convenience, define:

$$\psi_{kc}^{n+1}(y, x) = E\left[\tilde{d}_{kc}(y, x) | d_c, \lambda_k^n, \alpha^n, h_c^n\right] \qquad (4.7)$$

where k refers to either u or p depending on whether the unpolarized or polarized components are under test. As shown by [40] for a related problem, the complete data with these conditions are binomially distributed even though the complete data with no conditions are Poisson. The means of these distributions are therefore:

$$\psi_{pc}^{n+1}(y, x) = \frac{d_c(y)}{i_c^n(y)} \lambda_p^n(x) \cos^2\left(\alpha^n(x) - \theta_c\right) h_c^n\left(y - x\right) \qquad (4.8a)$$

$$\psi_{uc}^{n+1}(y, x) = \frac{1}{2} \frac{d_c(y)}{i_c^n(y)} \lambda_u^n(x) h_c^n\left(y - x\right) \qquad (4.8b)$$

The form of Q^{n+1} may be written out explicitly by substituting the $\psi_{kc}^{n+1}(y, x)$ terms for the $\tilde{d}_{kc}$ terms in (4.5).

4.3.3   The M-step.   The dividends of maximizing Q^{n+1} in lieu of the incomplete data log likelihood are realized in this section. First, the expected likelihood of the polarization components at pixel x_0 are maximized by finding the zero of the

first partial derivatives:

$$\frac{\partial Q^{n+1}}{\partial \lambda_p(x_0)} = \sum_c \sum_y \frac{\psi_{pc}^{n+1}(y, x_0)}{\lambda_p(x_0)} - \sum_c \cos^2\left(\alpha(x_0) - \theta_c\right) = 0 \qquad (4.9a)$$

$$\frac{\partial Q^{n+1}}{\partial \lambda_u(x_0)} = \sum_c \sum_y \frac{\psi_{uc}^{n+1}(y, x_0)}{\lambda_u(x_0)} - \frac{C}{2} = 0 \qquad (4.9b)$$

$$\frac{\partial Q^{n+1}}{\partial \alpha(x_0)} = -2\sum_c \sum_y \psi_{pc}^{n+1}(y, x_0) \tan\left(\alpha(x_0) - \theta_c\right) + \sum_c \lambda_p(x_0) \sin\left[2\left(\alpha(x_0) - \theta_c\right)\right] = 0$$

$$(4.9c)$$

where C is the number of available channels. Buried in each of these results is the assumption that $\sum_y h_c(y) = 1$ for all c and y; the conditions for this statement will be explained in section 4.3.4. At this point, the proper selection of channel orientation angles, θ_c, is critical. When θ_c is evenly distributed over all possible linear polarization states (e.g. 0°, 60°, -60° for a three channel system or 0°, 45°, -45°, 90° in the four channel case) the following trigonometric identity holds for all possible $\alpha(x_0)$:

$$\sum_c \cos^2\left(\alpha^{n+1}(x_0) - \theta_c\right) = \frac{C}{2} \qquad (4.10a)$$

$$\sum_c \sin\left[2\left(\alpha^{n+1}(x_0) - \theta_c\right)\right] = 0 \qquad (4.10b)$$

As a result, equations (a) and (c) in (4.9) are simplified and the estimators *decouple entirely* across the parameters. Hence the estimators for λ_u, λ_p are of the form:

$$\lambda_k^{n+1}(x_0) = \frac{2}{C} \sum_c \sum_y \psi_{kc}^{n+1}(y, x_0) \qquad (4.11)$$

where k is u or p for the unpolarized and polarized components respectively and the $n + 1$ superscript is added to signify that the estimate has been updated.

The reader may easily verify that each ψ_{pc}^{n+1} is actually the fully polarized component of image c. As such, it is appropriate to introduce an intermediate

Stokes vector $\mathbf{S}^{n+1}$:

$$\mathbf{S}^{n+1} = M^{-1}\Psi_p \tag{4.12}$$

such that

$$\alpha^{n+1}(x_0) = \frac{1}{2}\tan^{-1}\frac{S_2^{n+1}(x_0)}{S_1^{n+1}(x_0)} \tag{4.13}$$

where Ψ_p represents the vector of fully polarized components ψ_{pc}^{n+1}. Equation (4.13) agrees with intuition but the proof is nontrivial; the details for the three channel case are worked out in Appendix C. The second derivative test may be applied to the equations in (4.9) to verify that these estimates do indeed maximize Q^{n+1}.

4.3.4 Incorporating Schulz's GEM PSF Estimator. What remains then is to estimate the point spread function for each channel. The first partial derivative of Q^{n+1} with respect to an individual channel PSF at pixel $z = y - x$ is:

$$\frac{\partial Q^{n+1}}{\partial h_c(z)} = \sum_y \frac{\psi_{pc}^{n+1}(y, y-z) + \psi_{uc}^{n+1}(y, y-z)}{h_c(z)} - \sum_y o_c^{n+1}(y-z) \tag{4.14}$$

which is identical to the partial derivative with respect to the PSF of the objective function in the polarization insensitive case. Consequently, we may directly incorporate Schulz's PSF estimator (specifically, in [39] section 5) into the present case. What follows are the salient points of the original estimator with notes on some minor modifications; the reader is referred to the original article for a thorough derivation and an explanation of the advantages of this approach. Define:

$$h_c(x, \varphi_c^{n+1}) = \left| \sum_u A(u) \exp\left[i\varphi_c^{n+1}(u)\right] e^{-i2\pi kux} \right|^2 \tag{4.15}$$

where $A(u)$ is the aperture function of the imaging system (constrained such that $\sum_u A(u) = 1$), k is a constant related incorporating both wavelength and sampling effects, and φ_c^{n+1} is the current estimate of the atmospherically induced phase func-

tion at the aperture for channel c. In the case of a circular aperture with radius r, $A(u) = 0$ when $\|u\| > r$.

This definition of h_c, which varies from Schulz's original, allows for $\sum_y h_c(y) = 1$ in equation (4.9). Though this is a necessary step before successfully invoking the trigonometric identities in (4.10), it comes with drawbacks. In the Schulz model, channel to channel gain variations, a_c, such that $\sum_y h_c(y) = a_c$, are accounted for in the joint estimator. Here, an a_c term would be useful for modeling total transmission variations between channels. Total transmission, in this context, is equivalent to the action of an unknown neutral density filter. Modification of the estimator to allow for these variations is left to future work.

Since the aperture function is known in advance, the PSF estimation problem is recast into estimation of the phase screen, φ_c via one (or more) iterations of the Gerchberg-Saxton (GS) phase retrieval algorithm [11]:

$$\varphi_c^{n+1} = \begin{cases} \tilde{\varphi}_c & \text{if } \sum_x \xi(x) \ln h_c(x, \tilde{\varphi}_c) \geq \sum_x \xi(x) \ln h_c(x, \varphi_c^n), \\ \varphi_c^n & \text{otherwise} \end{cases} \tag{4.16}$$

where

$$\xi(x) = \frac{h_c(x, \varphi_c^n)}{D_c} \sum_y \frac{d_c(y)}{i_c^n(y)} o_c^n(y - x) \tag{4.17}$$

given

$$D_c = \sum_x o_c^{n+1}(x) = \sum_y d_c(y) \tag{4.18}$$

and one iteration of the GS algorithm:

$$\tilde{\varphi}_c = \text{ph}\left\{ \mathscr{F}^{-1}\left[\sqrt{\xi(x, \varphi_c^n)} \exp\left(i \cdot \text{ph}\left(h_c(x, \varphi_c^n)\right)\right) \right] \right\} \tag{4.19}$$

where $\mathscr{F}^{-1}$ is the inverse Fourier transform operator and "ph" is an operator that extracts the phase angle from a complex number. Equation (4.18) is a statement

of energy conservation. This term does not exist in its present form in the original paper; instead, there was an additional constraint in Schulz's derivation: $\sum_x o(x) = 1$. The reader may easily verify, however, that this change is wholly consistent.

4.4 Test Results from Laboratory Data

In this section, the polarimetric blind deconvolution algorithm is put to the test using data from a laboratory imaging polarimeter. The test sensor consists of a Photometrics Cascade 512B camera, a single 250 mm focusing lens, and a variable polarization analyzer. The camera array is 512×512 pixels with a 16 um pitch, is cooled to -30° C, and has an approximately uniform response of 4 photons per count at 660 nm. Aside from quantization noise, the imager also exhibits "dark" noise and bias. At the irradiance levels shown below, this noise is weak compared to the photon dominated noise of the target. An average dark bias is subtracted from the data in post processing. The lens is stopped down to 3.175 mm to ensure proper sampling. In the configuration under test, the effective system magnification is 0.22.

The test target consists of two fully polarized parallel bars, 2 mm in length, and back illuminated by a red (660 nm center wavelength) diode. The polarization angles of the two bars are approximately orthogonal: 2° for the top bar and -83° for the bottom bar (all angles are in reference to the horizontal direction in the imagery). The diode light passes through a diffuse screen prior to being polarized in order to even out the illumination across the target.

The collected data consists of three images, each collected at a different analyzer orientation: 0°, 60°, and -60°. The 60° and -60° collections are corrupted by a random plastic phase screen placed at the aperture. This plastic screen is weakly birefringent. Between the 60° and -60° collections, the orientation of the phase screen is rotated. In this way, each channel is presented with a different PSF analogous to the atmospheric short exposure imaging case. Before processing, the

images were cropped down to 200×200 pixels and coarsely registered. These data are shown in figure 4.1.

(a) the 0° channel   (b) the 60° channel   (c) the -60° channel
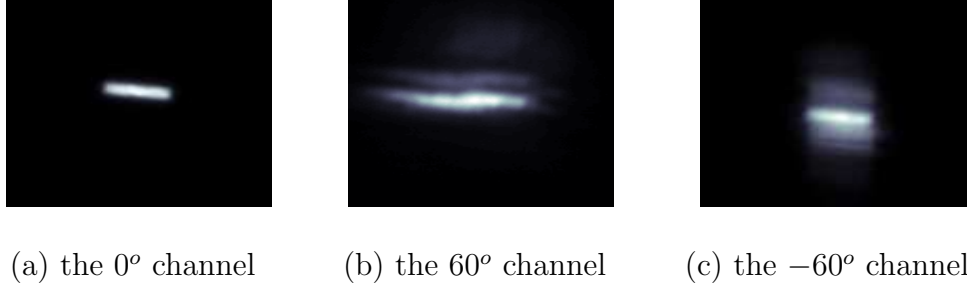
Figure 4.1: The estimator test data.

In the 0° case, only one bar appears in the image because the -83^0 bar is almost fully suppressed by the channel analyzer. In the other cases, phase error dominates. For comparison to 3.1b and 3.1c, the aberration free data for the 60°, and -60° channels are shown in figure 4.2.

(a) the 60° channel   (b) the -60° channel
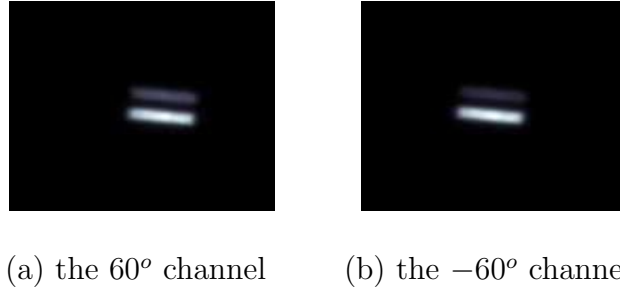
Figure 4.2: The 60°, and -60° channels in focus.

From the data in figure 4.1 the algorithm derives an initial guess at the polarized and unpolarized parts of the scene, as shown in figure 4.3a and 4.3b. The remaining images in figure 4.3 show the results of the algorithm after 500 iterations (at which point the algorithm stagnates).

Recall that the true target image is fully polarized. Consequently, the restored λ_u should contain essentially no signal; as shown in figure 4.3c, this appears to be

60

the case. Quantitatively, λ_u contains 9.34×10^7 photons in the initial estimate, and only 1.09×10^5 photons in the final estimate.

(a) initial λ_u estimate   (b) initial λ_p estimate

(c) final λ_u estimate   (d) final λ_p estimate
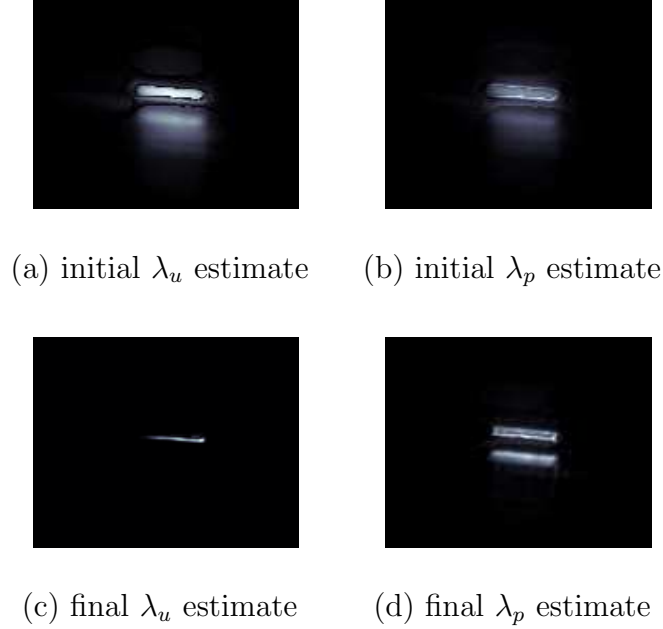
Figure 4.3: The unpolarized and polarized scene components before and after restoration.

Restoration of the fully polarized bar targets is achieved. What remains then, is to consider the restored angle of polarization. From equation (4.13), we see that an angle is estimated for every pixel whether or not the pixel contains meaningful polarization content. As an interpretably aid, figure 4.4 shows the on-target estimated angles masked off with the image in 4.3d. The estimated angles are -8° for the top bar and -72° for the bottom bar.

The ultimate cause of this angle bias, which has been observed across a multitude of measurements with different phase screens, is elusive. One possible cause for this discrepancy is that several real world effects are not taken into account in the model. For instance, the polarizers are less than ideal (extinction ratio of $\approx 10^6$). In addition, unmitigated optical activity, Fresnel losses, or unmodeled signal attenuation at the phase screen may be bias contributors as well. In the latter case,

Figure 4.4: The recovered target angle of polarization (on target pixels only).

inclusion of a Schulz a_c like term could possibly be helpful. It is certainly possible that the remaining photons in the unpolarized image, if restored properly, could possibly compensate for this bias.

Finally, it is of interest to present the estimated point spread functions (figure 4.5). Sub-figure 4.5a contains the initial guess PSF for all channels, arb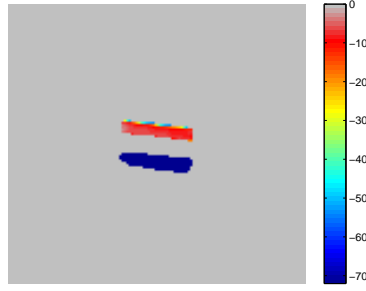itrarily selected to contain 1 wavelength of defocus aberration. The remaining figures show the final estimates of the channel PSFs at the conclusion of the restoration. Each PSF in this figure is magnified $\times 2$ compared to the scale in figure 4.1. Note that the rotation of the phase screen is evident between the 60° and -60° channels. The 0° channel, which is essentially unaberrated, tends toward a diffraction limited PSF.

4.5 Technique Variations: Prior Knowledge and Multiple Frames

Many variations of this estimator are readily achieved by incorporating priors. For instance, prior knowledge of the channel point spread functions would be particularly useful in terms of speeding up algorithm convergence and increasing the overall fidelity of the restored images. In this case, section 4.3.4 would be ignored and the given PSFs could be substituted directly into (4.11). In a sense, this known PSF case provides a polarimetric, multichannel version of the Richardson-Lucy algorithm.

There may also be the case where the intended target is known to be fully polarized or unpolarized (against a dark background). In the fully unpolarized case

(a) initial h_c estimate (all (b) final 0° PSF estimate
channels)

(c) final 60° PSF estimate (d) final -60° PSF esti-
mate
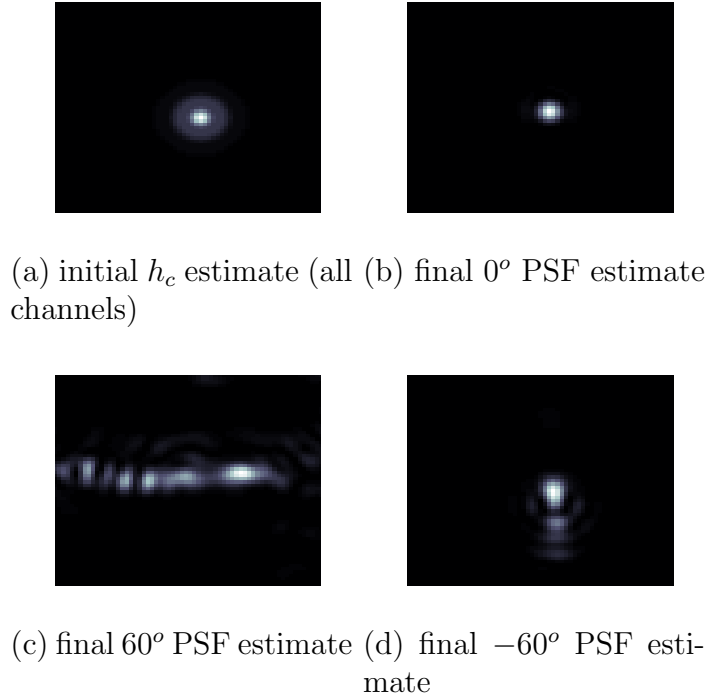
Figure 4.5: Close up of the estimated point spread functions.

(i.e. $\lambda_p(x) = 0$ for all x), the estimator reduces to Schulz's estimator. In the fully polarized case, the rule $\lambda_u(x) = 0$ for all x is enforced and only λ_p, α, and h are estimated. In more exotic variations, prior distributions could be imposed on the angle or degree of polarization based on source-target-sensor geometry.

In perhaps the most obvious extension, multiple frames could be collected for each channel. The added noise and PSF diversity (assuming the PSF is non-stationary) would "sharpen" the likelihood function and could be expected to improve the estimator. Implementation of this improvement is achieved by summing over an additional index of frames in (4.11) with an appropriately modified per-frame weighting (i.e. for N frames per channel, $\frac{2}{NC}$ instead of $\frac{2}{C}$).

4.6 Improvements Over Single Channel Deconvolution

The results in the previous section demonstrate the viability of the polarimetric blind deconvolution algorithm. What remains then, is to determine how the

algorithm compares to the alternatives. Though this estimator has no peer in the literature, it is possible to estimate each channel image and point spread function individually (i.e. without knowledge of the other channels) and then combine the result in the end to estimate λ_u, λ_p and α or any equivalent representation. In this section, simulated polarimetric imagery is used to compare the new joint estimator with Schulz's polarization insensitive blind deconvolution algorithm applied on a per-channel basis.

As a historical note, Schulz did not address the problem of estimating an image and a point spread function from a single frame of data in his original work. However, in the single channel case, the image estimator in the Schulz algorithm is indistinguishable from the Richardson-Lucy algorithm which has been applied to the single channel blind problem (see, for instance, [10]). The difference between these two approaches lies in how the PSFs are estimated. Since there is no obvious advantage to choosing one PSF estimator over the other, the Schulz PSF estimator is used here for consistency.

4.6.1 Target Simulation. Similar to the laboratory data, the simulated target consists of two fully polarized bar targets that are each 20 pixels in length, 3 pixels in width, and separated by 3 pixels. The bars appear against a dark field of 128×128 pixels. Each illuminated pixel contains 10^4 photons before it is blurred by the PSF, attenuated by the channel polarizers, and corrupted by Poisson noise. The angle of polarization for each bar is pulled from a uniform distribution of all possible polarization angles. The phase for each channel point spread function is generated from a random combination of the first 9 Zernike polynomial coefficients [34]. Each Zernike coefficient is normally distributed with zero mean and a variance of 1 wavelength (i.e. a phase of 2π radians). The blurring and channel attenuation action of the simulated sensor results in a wide variety of image signal-to-noise ratios even without varying the illumination rate. The sensor itself is in the previously

described 0°, 60°, and -60° configuration. Example simulated channels are shown in figure 4.6.

(a) the 0° channel   (b) the 60° channel   (c) the -60° channel
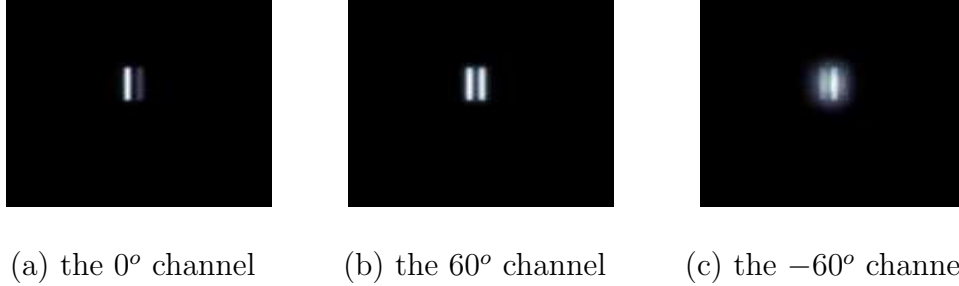
Figure 4.6: Example simulated channels.

4.6.2 Deconvolution Algorithm Implementation.   Recall that the polarimetric deconvolution algorithm reduces to Schulz's algorithm in the case where the target is known to be fully unpolarized a priori. This is also true when only a single channel image and PSF are estimated. In this case, the channel images are estimated individually from equation (4.11) for λ_u with $c = 1$. The PSF estimator is as shown in section 4.3.4. After each algorithm iteration is complete, the Stokes vectors are formed from (2.23). Similarly, the Stokes parameters at each iteration can be calculated from λ_u, λ_p, and α for each iteration of the multichannel estimator:

$$S_0 = \lambda_u + \lambda_p \tag{4.20a}$$

$$S_1 = \frac{\lambda_p}{\sqrt{1 + \tan^2 \alpha}} \cdot \begin{cases} 1 & -45^o < \alpha < 45^o \\ -1 & otherwise \end{cases} \tag{4.20b}$$

and, given this result, S_2 can be calculated from (2.13).

Both the single and multichannel algorithms are given the same aperture size and initial PSF guess (arbitrarily selected to be 1 wave of defocus). Both algorithms are run for 100 iterations for 1500 separate realizations of the target and noise.

4.6.3 Results. Normalized Mean Squared Error ($NMSE$) is routinely used as a image deconvolution evaluation metric [21]. For a true image intensity, f, and an estimated image, $\hat{f}$, NMSE is defined to be:

$$NMSE = \frac{\sum\limits_{x} \left[f(x) - \hat{f}(x) \right]^2}{\sum\limits_{x} f^2(x)} \tag{4.21}$$

where x is the 2-dimensional coordinates in the image plane. It is clear from (4.21) that a smaller NMSE represents a better estimate of f. Typically, the NMSE is plotted against iteration number to convey both the accuracy and rate of convergence of the estimator. In the present case, it is desirable to convey the accuracy and rate of convergence for both the image itself and its polarimetric properties. In previous sections, image polarization content is conveyed through λ_u, λ_p, and α. Clearly, NMSE applied to an α "image" would be uninterpretable. Instead, the Stokes parameters (which all have units of intensity) are fed into the NMSE equation for consistent representation. Finally, the goal is to represent the aggregate results of many simulated targets; therefore, the following plots contain the *median* (second quartile) NMSE with error bars representing the first and third quartiles of these data. Quartiles are used in lieu of mean and standard deviation to avoid error bars with negative values at low NMSE. The NMSE is shown for each Stokes parameter in figure 4.7.

It is clear from these results that the multichannel estimator provides both a better median restoration of the target (in all cases) and a substantially smaller interquartile range on the restoration in the S_1 and S_2 cases. Recall that parameters S_1 and S_2 carry all the polarization information about the scene. Figures 4.7b and 4.7c for the single channel estimator show that, after around 25 iterations, the NMSE actually increases slightly for S_1 and S_2; in other words, the single channel algorithm produces a median estimate that is getting farther from the truth with additional iterations.
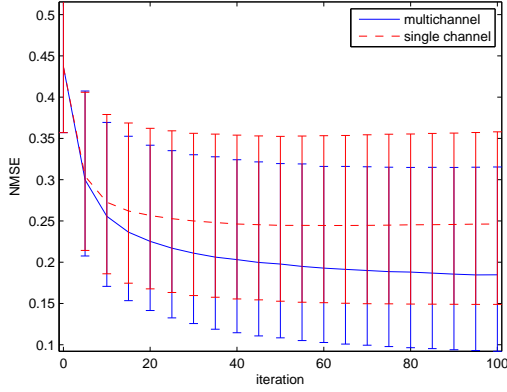
(a) S_0
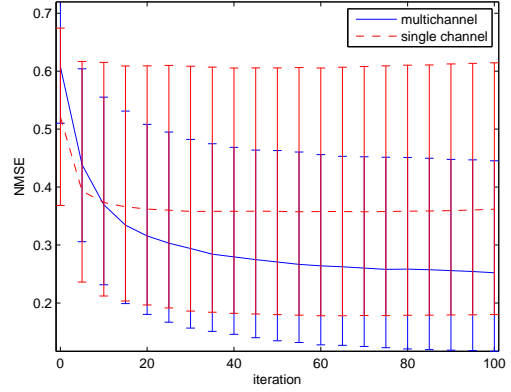
(b) S_1
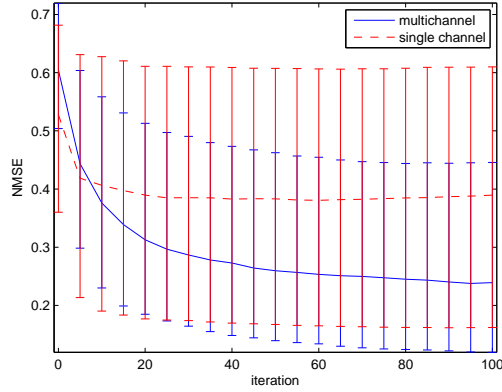
(c) S_2

Figure 4.7: NMSE quartiles for the Simulated Stokes images.

Equation (4.9) helps to explain the observed behavior. In the multichannel case, information is shared between channels via the estimates of λ_u, λ_p, and α. Mathematically, this information transfer occurs during the sum over c in (4.9). The result of this transfer is a more constrained estimator. These image constraints also indirectly translate into improved PSF estimates even though the PSFs themselves do not share information across channels. In the single channel case, without this shared information, the number of possible combinations of PSFs and images that maximize Q increases, resulting in more estimator error on average. One obvious

extrapolation of this argument is that the restoration would be improved further if additional channels were added to the estimator.

4.7   Further Analysis of the Angle Bias Issue

In this section, simulation is used to determine whether or not the linear polarization angle error shown in section 4.4 is a symptom of an actual bias in a statistical sense. The simulated data is as described in section 4.6. In this case, the multichannel deconvolution algorithm is run for 200 iteration over 1500 realizations of the data. (200 iterations are used is this case to ensure near convergence of the results.) The restored target polarization angles, $\hat{\alpha}$, are taken to be the average over the true bar target area and the bias is defined as:

$$b = \alpha - \hat{\alpha} \tag{4.22}$$

where b is defined between -90° and 90° (example: $\alpha - \hat{\alpha} = 120^o \Rightarrow b = -60^o$). The simulation results show an average bias of 0.5^0 with a standard deviation of 16.3^0. Consequently, even in the absence of calibration and unmodeled noise errors, the laboratory results in section 4.4 are typical, at least in the sense that the reported angle errors are within a standard deviation of the mean error in this simulated case. A histogram of the angle bias results (bin width: 3.66^o) is shown in figure 4.8.
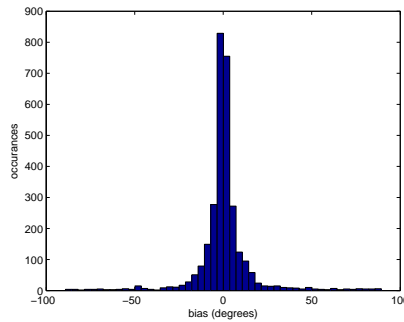
Figure 4.8: Results of the angle bias simulation.

4.8 Chapter Summary

In this chapter, a maximum likelihood multichannel blind deconvolution estimator is developed from the generalized expectation maximization algorithm. The efficacy of the algorithm is demonstrated using test data from a three channel imaging polarimeter in a laboratory setting and in simulation. The laboratory reconstructed test imagery is very close to the true underlying target scene in terms of the estimated total polarized and unpolarized content though somewhat biased in terms of angle of polarization. Though it is difficult to identify the cause precisely, this type of error has been observed across several such experiments with different phase screens. In simulation, the polarization angle estimator is shown to be unbiased under ideal image acquisition conditions. Possible error sources include unmodeled noise and calibration errors in the target, phase screen, or sensor.

V. Detection through Obscurations Using Optimized Temporal Polarization Imaging

In this chapter, temporal fluctuations in polarization signature are maximized by forming linear combinations of polarization-sensitive intensity channels. These combination channels, which are the result of a principal components analysis, are also reduced in rank and therefore optimized for further processing. Temporal fluctuations are emphasized as a means to detect polarizing objects under substantial but weakly polarizing obscurations that would otherwise preclude detection in a traditional intensity image. The theoretical work, which is an expansion of previously published research, is demonstrated for three and four channel polarization imaging systems. Finally, the theory is tested through simulated examples using an empirical target obscuration model.

5.1 Target Detection in Obscurations

Several remote sensing techniques have been applied to the problem of target detection in the presence of heavy obscurations. Recent examples of modes applied to this problem include radar [30], hyperspectral imaging [17], and LIDAR [37] among others. The present work takes the first steps toward addressing the obscured target detection problem by exploiting temporal fluctuations in target polarization signature due to time varying obscurations. What follows is a description of a methodology believed to optimize a polarization imaging system to tackle this obscured target problem.

Consider a passive incoherent imaging system with any number of distinct channels. Each channel is most responsive to a different orientation of linear polarization. Under these constraints, a sensing modality is developed to detect polarizing targets through weakly polarized or unpolarized obscurants. A realistic example of this scenario would be detection of vehicles under heavy forest canopy from an air-

borne polarization imaging system. Canopy motion or the movement of the aircraft will provide the sensor with small, transient, polarized reflections off the target. Taken individually (i.e. from a single frame), these transient events may be statistically indiscernible from the obscurants in the space around them. Now consider an ensemble of these frames, all registered to the same scene. The obscured target pixels should have an appreciably larger variance than those pixels filled with obscured natural background (which is also largely unpolarized). The premise of this research is realized by determining the configuration of the polarization imager that is best suited to detect this target variance in polarization state while suppressing other sources of scene fluctuation (for instance, variance in total intensity) and correlation between channels.

J.S. Tyo published a method for optimizing a multi-channel polarization imaging system using principal components analysis [45]. His work provides the foundation for this research, but not without modification. Specifically, Tyo's derivation requires all incident radiation to be monochromatic. In doing so, this work is applicable to all permutations of elliptically and linearly polarized light but not, unfortunately, to unpolarized light, which is of specific interest here (unpolarized light is, among other things, polychromatic [42]). To reconcile this deficiency, section 5.2 applies this Stokes model to Tyo's optimization strategy. This result is then extended further to define the optimum combination of channels for detecting temporal fluctuations in polarization state. Section 5.3 applies this strategy to two notional polarization imaging systems including one of Tyo's examples, which is shown to be equivalent in this new formulation. Section 5.4 describes an empirical obscured target model which is employed in a simulated case study.

5.2 Channel Optimization

As in each of the previous chapters, the polarization imaging system is composed of N channels, each of which is most responsive to a different orientation of

linearly polarized light. Optimized combinations of these channels are generated (either through hardware or software implementation) and passed onto an image accumulator where a to-be-determined number of frames are stored until statistical relevance is achieved. In this case, the stored images are then used to form a standard deviation image for each of the optimized combination channels.

Equipped with a Stokes description of intensity at the detector array, Tyo's method, which is presented below, can be employed to construct a set of channel combinations that are uncorrelated, possibly reduced in rank, and hence simplified for further processing. These uncorrelated combination channels are then further optimized for maximum response to temporal fluctuations in polarization state.

5.2.1 Tyo's Method. The total intensity measured for each channel is represented by an $N \times 1$ vector, $\mathbf{I}$. The correlation matrix for an N channel polarization imaging system is given by:

$$C = E_\xi[\mathbf{I} \cdot \mathbf{I^T}] \tag{5.1}$$

where $E_\xi[\cdot]$ is the expected value taken over all possible polarization states. Following Tyo's prescription, decorrelation of these channels is achieved by solving for a matrix X such that

$$X^T C X = \left\{ \begin{array}{cc} \lambda_k & i = j \\ 0 & i \neq j \end{array} \right\} \tag{5.2}$$

where λ_k are the N eigenvalues of C and i, j are the row and column coordinates of $X^T C X$. In other words, $X^T C X$ is a diagonal matrix whose diagonal entries are the eigenvalues of C. In this arrangement, these eigenvalues are also the second moment of the (yet to be formed) uncorrelated combination channels. This fact will be useful later on. To achieve the required solution for (5.2), the columns of X are taken to

be the N normalized eigenvectors of C, $\mathbf{v_k}$:

$$X = [\mathbf{v_1}...\mathbf{v_N}] \tag{5.3}$$

Having determined X, the transformed channels (eigenchannels), $\mathbf{Z}$, are given by:

$$\mathbf{Z} = X^T\mathbf{I} \tag{5.4}$$

The channels $\mathbf{Z}$ are uncorrelated over the ensemble of possible linear polarization states thus an expansion of Tyo's original work is achieved. What remains is to find a subset of $\mathbf{Z}$ that is most sensitive to temporal fluctuation in polarization state.

5.2.2 Temporal Polarization Expansions. If this were a true principal components analysis, the next step would be to select a subset of $\mathbf{Z}$ to form a basis of possibly reduced rank to represent all of $\mathbf{I}$. Selection for this new basis would be determined from the magnitude of the associated eigenvalues [28]. Instead, channels in $\mathbf{Z}$ are selected based on their ability to maximize signal variance due to temporal fluctuations in degree of polarization. More succinctly, if γ, some minimum allowable variance threshold, is set, then an eigenchannel in $\mathbf{Z}$ is retained if:

$$E_\xi \left[E_P \left[\left(Z_i - \overline{Z_i} \right)^2 \right] \right] > \gamma \tag{5.5}$$

where

$$\overline{Z_i} = E_P \left[Z_i \right] \tag{5.6}$$

where the subscript P indicates expectation over degree of polarization. Recalling that

$$\lambda_i = E_\xi \left[Z_i^2 \right] \tag{5.7}$$

equation (5.5) can be simplified by rearranging the order of expectations:

$$E_P\left[\lambda_i\right] - E_\xi\left[\overline{Z}_i^2\right] > \gamma \tag{5.8}$$

This expectation rearrangement is acceptable because there is no reason to believe that angle of polarization and degree of polarization are statistically dependent quantities.

Methods for choosing γ can vary, especially if a priori knowledge of the distribution in P is available. Without this knowledge of P however, it will be shown that selecting $\gamma = 0$ is sufficient in several useful cases.

5.3 Example Polarization Imaging Sensors

The previously described methodology is completely general. The following examples contain a number of simplifications that are not required to gain a solution but do allow for more compact results. Each polarizer is assumed to be ideal. Additionally, it will be assumed that all incident radiation is linearly polarized, unpolarized or partially linearly polarized. In other words, there is no elliptically polarized light and $S_3 = 0$. Next, it is assumed that the distribution in total intensity is independent from the distribution of linear polarization states (this assumption is always true for unobscured targets).

Since there is now only linear polarization to consider, the angle of linear polarization, ξ, will be defined as in Chapter II. Finally, it is assumed that the polarized channels are evenly spaced on the same interval as ξ. In addition to be being a simplifying step, this assumption also ensures that one of the eigenchannels in $\mathbf{Z}$ is the sum of all the original intensity channels (as shown by Tyo).

5.3.1 The 3-Channel Case.   The 3-channel case is presented here for two reasons; the first is because it reduces the number of steps required to attain informative results and, second, it provides an example of how the derivation in [45] is equivalent to the case presented here.

74

Intensity detected by our 3-channel imaging polarimeter is given by substitution into equation (2.8):

$$I_0 = \frac{S_0}{2}\left(1 + \mathrm{P}\cos2\xi\right) \tag{5.9a}$$

$$I_{60} = \frac{S_0}{2}\left(1 - \mathrm{P}\frac{\cos2\xi - \sqrt{3}\sin2\xi}{2}\right) \tag{5.9b}$$

$$I_{-60} = \frac{S_0}{2}\left(1 - \mathrm{P}\frac{\cos2\xi + \sqrt{3}\sin2\xi}{2}\right) \tag{5.9c}$$

where the subscripts 0, 60 and -60 indicate the angle of polarization (in degrees) preferred for transmission through the channel polarizer. To reiterate a previous point, the orientations of these filters are not arbitrary, they are selected such that they are evenly spaced on the interval of ξ.

Given i and j as indices of the row and column entries in the 3×3 correlation matrix:

$$C_{ij} = \frac{1}{\pi}\int_{-\pi/2}^{\pi/2} I_i I_j d\xi \tag{5.10}$$

such that i or $j = 1$ corresponds to I_0, i or $j = 2$ corresponds to I_{60}, and so on. The matrix C has eigenvalues

$$\begin{aligned}\lambda_1 &= \frac{3S_0^2}{4}\\\lambda_2 = \lambda_3 &= \frac{3P^2 S_0^2}{16}\end{aligned} \tag{5.11}$$

and (normalized) eigenvectors

$$v_1 = \frac{1}{\sqrt{3}}\begin{bmatrix}1\\1\\1\end{bmatrix} \quad v_2 = \frac{1}{\sqrt{2}}\begin{bmatrix}-1\\0\\1\end{bmatrix} \quad v_3 = \frac{1}{\sqrt{6}}\begin{bmatrix}1\\-2\\1\end{bmatrix} \tag{5.12}$$

Note that several other eigenvectors with eigenvalues equal to λ_2 are possible, but all are equivalent. This eigenvector result is in agreement with the special case of the 3-channel derivation in [45].

Moving on, the eigenchannels are given by substitution of (5.9) into (5.3) and (5.4):

$$Z = \begin{bmatrix} \frac{1}{\sqrt{3}} \left(I_0 + I_{60} + I_{-60} \right) \\ \frac{1}{\sqrt{2}} \left(I_{-60} - I_0 \right) \\ \frac{1}{\sqrt{6}} \left(I_0 - 2I_{60} + I_{-60} \right) \end{bmatrix} \tag{5.13}$$

Since there is no a priori knowledge about how these eigenchannels are distributed with respect to P, the test from equation (5.8) will be executed with $\gamma = 0$. First, note that

$$\begin{aligned} \overline{Z_1} &= E_p \left[\frac{1}{\sqrt{3}} \left(I_0 + I_{60} + I_{-60} \right) \right] \\ &= E_p \left[\frac{\sqrt{3}S_0}{2} \right] = \frac{\sqrt{3}S_0}{2} \end{aligned} \tag{5.14}$$

hence, for the first uncorrelated channel at least, the exact distribution of the degree of polarization is irrelevant. This result can be readily substituted into the test from equation (5.8):

$$E_p \left[\frac{3S_0^2}{4} \right] - E_\xi \left[\left(\frac{\sqrt{3}S_0}{2} \right)^2 \right] = 0 \tag{5.15}$$

Interestingly, even though this channel would be the largest contributing principal component in a traditional sense (by virtue of its dominating eigenvalue), it fails to exceed the $\gamma = 0$ variance threshold and therefore must be discarded.

The eigenvalues of the two remaining channels are equal and both dependent on P so, for any meaningful distribution on P, their variance will exceed a threshold of $\gamma = 0$. Consequently, both of these channels are retained as part of the scheme to maximize temporal variation in degree of polarization.

5.3.2   The 4-Channel Case.   A 4-channel imaging polarimeter (with equally spaced polarization channels) is of interest because three of the Stokes parameters

76

can be calculated directly using addition and subtraction on combinations of the channel outputs [5]:

$$S_0 = I_0 + I_{90}$$
$$S_1 = I_0 - I_{90} \qquad (5.16)$$
$$S_2 = I_{45} - I_{135}$$

In this case, the eigenvalues of the correlation matrix are given by:

$$\lambda_1 = S_0^2$$
$$\lambda_2 = 0 \qquad (5.17)$$
$$\lambda_3 = \lambda_4 = \frac{P^2 S_0^2}{4}$$

and corresponding eigenchannels:

$$Z = \begin{bmatrix} \frac{1}{\sqrt{4}} \left(I_0 + I_{45} + I_{90} + I_{135} \right) \\ \frac{1}{\sqrt{4}} \left(I_0 - I_{45} + I_{90} - I_{135} \right) \\ \frac{1}{\sqrt{2}} \left(I_{135} - I_{45} \right) \\ \frac{1}{\sqrt{2}} \left(I_{90} - I_0 \right) \end{bmatrix} \qquad (5.18)$$

Now the variance threshold test in (5.8) is applied to $\mathbf{Z}$. No additional manipulation is required to show that the sum channel ($\lambda_1 = S_0^2$) will not pass the threshold test for the same reasons that the sum channel did not pass in the 3-channel case. Furthermore, the channel corresponding to $\lambda_2 = 0$ contains no useful information and would be discarded by both a traditional principal components analysis and the temporal variance maximization analysis presented here.

The channels corresponding to λ_3 and λ_4 remain. Observation of (5.18) shows that these channels are actually just scaled versions of the Stokes parameters S_2 and S_1 as seen in (5.16). This result may suggest that it is only required to cast the measurements into S_2 and S_1 to maximize sensitivity to fluctuations in degree of polarization. Proof of this assertion is left to future work.

5.4 Analysis Using Simulated Data

The purpose of this section is to demonstrate the utility of the imaging scheme derived in section 5.3 using simulation. The simulation consists of a two plane obscured target model that varies in time in a statistically predictable way. The test data are presented along with the results from each eigenchannel.

5.4.1 Obscured Target Model. The simulation consists of a simple empirical obscuration model for a Stokes vector image in the object plane and an image plane model found using an arbitrary point spread function. Each point in the object plane, $S'(u, n)$, can be decomposed into two basis planes: $f(u, n)$, the front or obscuration plane, and $b(u, n)$, the back or target plane. Here, u is the two-dimensional coordinates in the object plane and n is the frame number. Each point in both f and b is described by a 4-dimensional Stokes vector corresponding to the case where each basis plane is directly illuminated by the source. Whenever the scene is illuminated by natural light, each point in S' can be represented as a linear combination of f and b. Specifically:

$$S'(u, n) = t(u, n)f(u, n) +$$
$$[1 - t(u, n)]\, r(u, n)b(u, n)$$

(5.19)

where f and b are scaled by $t(u, n)$, the fraction of a pixel obscured by f, and $r(u, n)$, the fraction of the maximum possible b that is actually reflected. At each position u, S' is a realization of a random process defined by the four underlying processes: f, b, t and r. Processes f and b are each assumed to have two components. The larger component varies slowly with the respect location of the illumination source (i.e. the sun) while the smaller component varies rapidly with small changes in surface orientation. The slowly varying components of f and b are treated as constants. Conversely, t and r vary with each frame and depend partially on the density of the obscurant. In cases where the obscurant is a natural media (e.g. a forest canopy),

the obscurant is assumed to be weakly polarized when compared to the underlying target.

Having previously established a requirement for incoherent illumination, the Stokes image at the detector is given by

$$S(x, n) = [h \otimes S'] (x, n) \tag{5.20}$$

where h is the sensor specific point spread function. Equation (5.20) can be readily derived for each entry in S. Consider the formation of an incoherent image, I, without regard to the polarization of the incident light:

$$I = h \otimes S'_0 \tag{5.21}$$

where, borrowing from the definition of the Stokes vector, S'_0 is the total intensity of the scene as predicted by geometrical optics. S'_0 can be decomposed into parts that represent orthogonal polarization states and, since convolution is distributive, so can I:

$$I = h \otimes \left(I_\perp + I_\parallel\right) = h \otimes I_\perp + h \otimes I_\parallel \tag{5.22}$$

By careful selection of the orthogonal components in this equation (refer to equation (5.16)), one can form any of the other terms in the Stokes vector. For instance:

$$S_1 = h \otimes I_0 - h \otimes I_{90} = h \otimes S'_1 \tag{5.23}$$

Similarly, the same process can be used to define S_2 in terms of S'_2 and so on for S_3.

Equation (5.19) is the simplest possible model for mixing two images and does not include polarization effects. Instead, polarization effects are added in later through judicious selection of Stokes vectors for different classes in the scene.

Additionally, the model in (5.19) contains no noise terms. Though not necessary to demonstrate the concepts from the previous section, a realistic noise model would be critical for establishing limits on the effectiveness of this obscuration detection scheme.

Furthermore, equation (5.19) ignores the effects of thickness and/or depth in the obscuration "plane". To illustrate the limitations on this model, consider the case where the primary obscuration is much nearer to the sensor than the target. In this case, the obscurations would effect the formation of the average $h(x)$ as well as $\mathbf{S}'$. These effects on $h(x)$ are well described in [12]. At a minimum, the ratio of the target-to-obscuration distance over sensor-to-target distance should be $<< 1$ for model applicability in this sense. More specific bounds on model applicability are left to future work.

5.4.2 Test Data Sets. As described in the previous section, the obscured target model requires a front plane (figure 5.1), containing the primary obscuration, and a back plane figure (5.2), which contains the targets and some natural background.

Figure 5.1: The front plane or foliage image used during the simulation.

For the purposes of simulation, these images are broken down into three primary classes: targets, foliage and grass. Obviously, more classes exist in both of these

80

Figure 5.2: The unobscured back plane image containing the targets used during the simulation.

images. These additional classes have been ignored for expediency and, regardless, the ideas put forward in section 5.3 can be tested without them.

Each class is assigned an average Stokes vector:

$$
\begin{aligned}
S_{grass} &= \begin{bmatrix} 1 & -.05 & .05 & 0 \end{bmatrix}^T \\
S_{foliage} &= \begin{bmatrix} 1 & .03 & .03 & 0 \end{bmatrix}^T \\
S_{target} &= \begin{bmatrix} 1 & -.46 & 0 & 0 \end{bmatrix}^T
\end{aligned}
\tag{5.24}
$$

Each of the grass and foliage classes have an average degree of polarization of only a few percent while the target, which is made to represent a near specular reflection, is significantly higher.

The average percent pixel obscuration, $E[t(u,n)]$, is 99.9% with a standard deviation of 0.03%. In other words, even though the front plane is "flat" it almost completely obscures the back plane at all times. Likewise, the average percentage of the maximum possible reflection off the backplane, $E[r(u,n)]$ is 50% with a standard deviation of 10%. The purpose of $r(u,n)$ is to partially capture the effects of depth in the obscuration by forcing the backplane to be only partially illuminated with significant overall fluctuation.

The point spread function used to blur the composite Stokes image is shown in figure 5.3 in the same scale as the image. These parts come together under equation (5.20) to form simulated Stokes images in the detector plane.
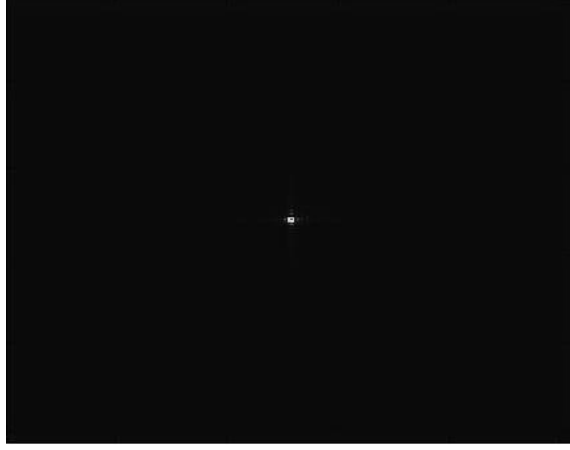

Figure 5.3: Simulated PSF.

5.4.3 Results. All simulated results are shown with a 100% linear stretch and the MATLAB default color map. Figure 5.4 shows a single simulated image from the Z_1 through Z_4 channels given by equation (5.18). Though present in the data, the locations of the obscured targets are imperceptible.

True to the predicted eigenvalues for the 4-channel case in equation (5.17); Z_1 appears to contain the most information (largest eigenvalue), Z_2 contains virtually no information (0 eigenvalue), while Z_3 and Z_4 both contain some information (but still no indication of the targets). Equation (5.24) shows that the targets are most highly polarized in S_1 so, if the targets could be detected, it would likely occur in eigenchannel Z_4 (figure 5.4d). Regardless of channel, target detection through the provided obscuration using only a single frame appears unlikely.

Figure 5.5 contains the standard deviation images of channels Z_1 through Z_4. Each standard deviation image is calculated from 25 separate realizations of an eigenchannel image. Each additional image is generated with a different randomized $t(u, n)$ and $r(u, n)$. Perfect registration between images is assumed throughout.

(a) Z_1 (b) Z_2
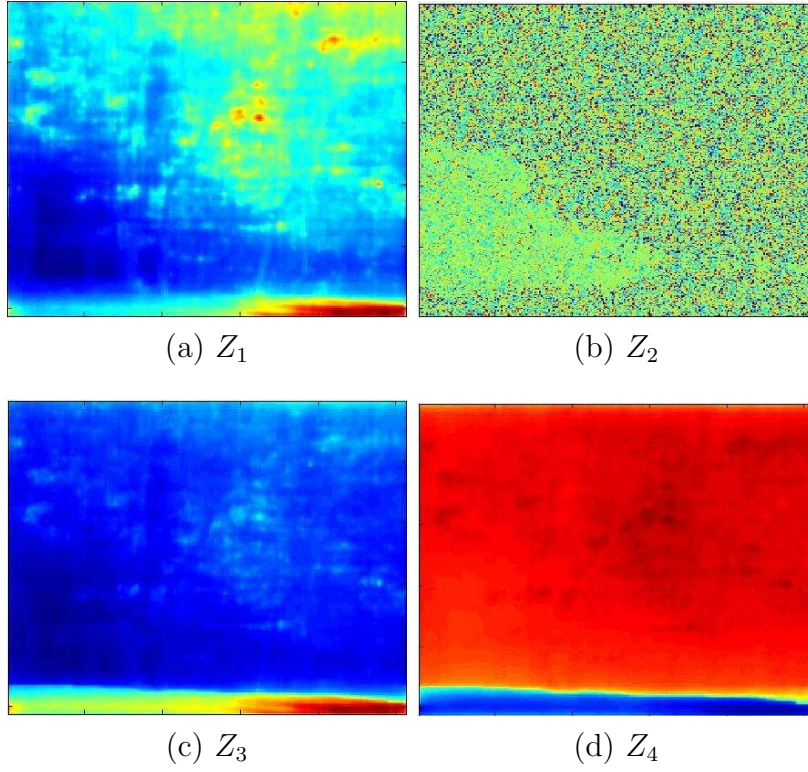
(c) Z_3 (d) Z_4

Figure 5.4: A single frame of the simulated eigenchannels.

The derivation in section 5.3 for the 4-channel case predicts that channels Z_1 and Z_2 should be discarded because their variance is 0 with respect to P, which is assumed to the variable driving fluctuation from image to image. Figures 5.5a and 5.5b, the standard deviation images of Z_1 and Z_2, appear to generally uphold this prediction with some interesting exceptions.

First, note the foreground grass in figure 5.5a. No portion of the background scene penetrates this portion of the image and, consequently, the variance across this region is very low (the regional variance is low but not zero because of point spread function effects). In other words, since the grass here is impenetrable, it violates the original assumptions made about the obscuration and hence its behavior in the standard deviation image is not predictable by this model.

Second, there is some indication of the right-most target in the Z_1 standard deviation image even though this optimization method predicts that there should be

(a) Z_1 (b) Z_2
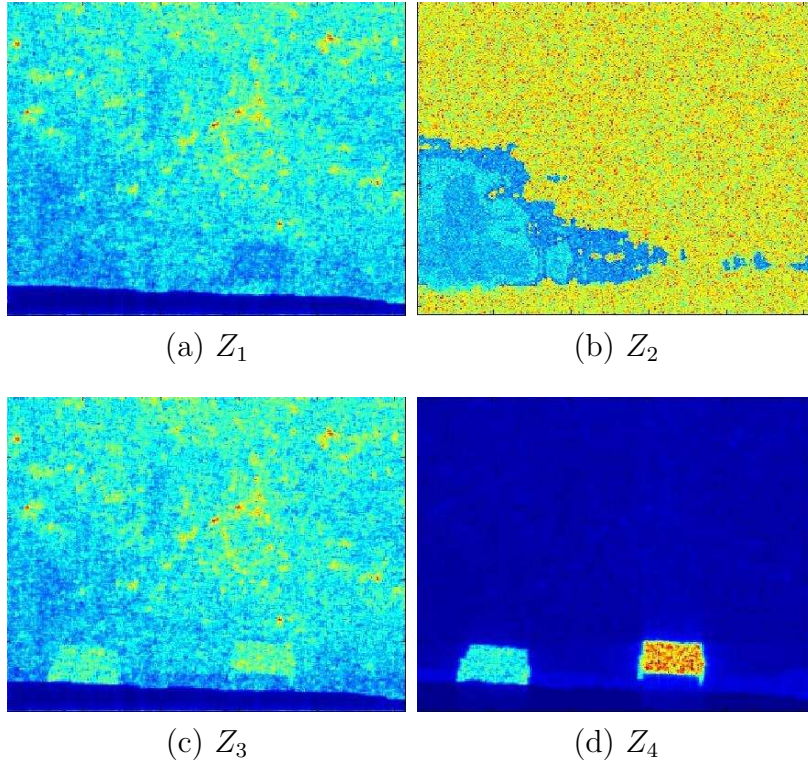
(c) Z_3 (d) Z_4

Figure 5.5: Standard deviation images of the eigenchannels.

none. To explain this apparent incongruity, recall that the distribution over all possible intensities was assumed to be separable from the distribution of possible linear polarization states. This assumption is required by equation (5.10) for formation of the multi-channel covariance matrix but is violated later when the obscured target model is defined. Additionally, variance that occurs purely due to fluctuation in total intensity is ignored throughout this development. Though clearly this assumption is not entirely accurate, it still appears to be a reasonable approximation, especially when the information content in this channel is compared with that in the Z_3 and Z_4 channels.

For the same reasons, the Z_2 channel and corresponding standard deviation image also contain some information content though none of it is apparently useful.

Little further commentary is required to show that, as predicted by this optimization method with $\gamma = 0$, channels Z_3 and Z_4 clearly contain the most informa-

tion about the obscured targets. Consequently, no target information would have been lost if channels Z_1 and Z_2 had been discarded completely.

Up to this point, no consideration has been given to the original (i.e. correlated) intensity channels. Figures 5.6 and 5.7 contain a single frame and standard deviation image for the I_{90} channel, which, for the targets as defined, should contain the most target signal.
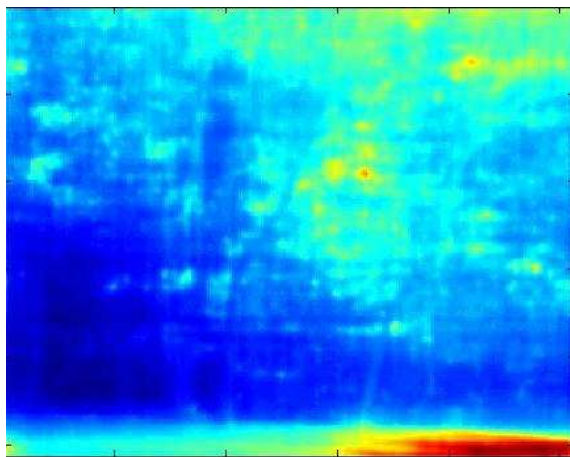

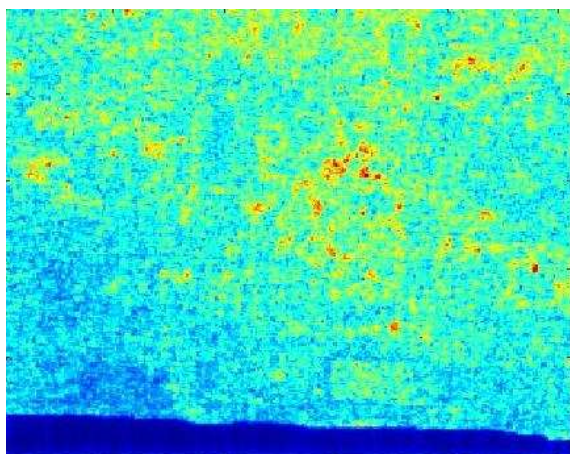Figure 5.6: A single simulated frame from the I_{90} channel.

Figure 5.7: The I_{90} standard deviation image.

The I_{90} standard deviation image does show some evidence of the targets though the quality of the information present is far inferior to that contained in

the Z_4 standard deviation image. For brevity's sake, the other intensity channels are not shown because the results are much the same as the I_{90} channel.

5.5   Summary

A principal components analysis of a polarimetric imaging system is derived for the case of polarized, partially polarized, and unpolarized radiation. This result is then applied to the problem of imaging through obscurations by discarding the eigenchannels that are likely to be insensitive to temporal fluctuations in polarization state. The optimized temporal polarization imaging method presented in this research provides a viable scheme for target detection in the presence of obscurations. Defense of this assertion is provided in the theoretical development and tested against a simulated dataset.

In the simulated example, with no prior knowledge of the target, this method reduces the number of channels required for effective target detection from 4 to 2 with relatively trivial pre- and post-processing requirements. This notional sensor was configured such that three of the Stokes parameters can be calculated directly from the measured intensities. Under these circumstances, the channel reduction result is expected since only two of the three Stokes parameters depend on degree of polarization. Referring back to the derivation at (5.18), perhaps the more interesting result from this example is that Stokes parameters are also shown to be the optimum combination channels. Finally, this example is a special case; the demonstrated method allows for calculation of the optimum combination channels for any polarization imaging sensor.

While the results are compelling, the simulation ignores three important difficulties that will arise in real world applications. First, image to image registration is assumed to be perfect for all channels at all times. Second, real targets in this scenario may be obscured in part by objects that are completely opaque at all times, effectively breaking up the target in the standard deviation image. Third, all signals

were assumed to be noiseless. Compensation for these difficulties, and more minor unnamed others, will be fleshed out in future work using field data.

VI. Conclusion

The three preceding chapters address problems involving polarimetric image registration, restoration, and analysis in the presence of noise and a non-deterministic channel. Unlike the bulk of the related literature, these problems are approached from an estimation theory perspective combined with a complete physical model of polarization. As is demonstrated, this combination is fertile with research opportunities that draw upon research in traditional, polarization insensitive image processing. In this section, the previous chapters are summarized and concluding remarks are presented.

In chapter III, the Cramer-Rao lower bound on image registration errors by Robinson and Milanfar is generalized to the case of multichannel polarimetric imagery. In doing so, the problem is posed as a joint estimation of both the translational registration errors and of the polarimetric image itself. The primary difficulty in calculating the bound directly is that the result requires inversion of an enormous (even by the standards of desktop computers) Fisher information matrix. This inversion is made tractable by applying matrix theory to the FIM. In doing so, the bounds largely decompose into components that are easily identifiable in the processing chain: target, receiver, and estimator.

The bound is also used to describe three and four channel polarimetric imaging systems and the special case of N polarization insensitive images. For N frames of polarization insensitive imagery, the Cramer-Rao bound derived by Robinson and Milanfar is shown to be the limit of the bound as N becomes large. In the three channel polarization case, the Cramer-Rao bound for any joint estimator is infinity. Consequently, the registration parameters and Stokes images must be estimated separately. An additional treatment of joint estimation versus external measurement can be found in appendix B.3. Finally, the form of the bound suggests that the

optimum channel spacing is 60° and 45° respectively in the three and four channel cases.

In chapter IV, an iterative maximum likelihood blind deconvolution algorithm is derived using expectation maximization. This algorithm leverages a complete data model based on the polarized and unpolarized components of the scene and a uniform spacing between channels to decouple the joint estimator into four separate estimators of the polarized intensity, angle of polarization, unpolarized intensity, and point spread function. The resulting algorithm is shown to be viable using imagery collected in the laboratory. Simulated data is used to demonstrate the improvement gained using this multichannel approach when compared to the only viable alternative, blind deconvolution of each channel individually. Finally, the estimated errors in polarization angle from the laboratory data are shown to be typical of results found in simulation.

In chapter V, a principal components analysis of polarization imagery is combined with temporal variation thresholding for polarimetric imagery. The goal of this effort is to reduce the number of channels required to detect potential targets in the presence of obscurations. Results are demonstrated theoretically for the three and four channel cases. In the three channel case, the PCA optimized channels are shown to agree with previous research in which only fully polarized radiation is considered. In the four channel case, the PCA and temporal variation optimized channels are shown to be the Stokes parameters S_1 and S_2. This four channel case is then validated using simulation and a simple random obscuration model.

6.1 *Research Extensions*

The Cramer-Rao bound research opens the possibility for substantial future work. This research could follow the lead of Robinson and Milanfar [33] and address the problem of registration estimator bias for a specific algorithm as it applies to polarimetric imagery. Additionally, Yetik and Nehorai's work could be expanded to

include a polarimetric bound for other types of image deformation (e.g. rotation, shearing, etc.) or bounding estimator error for polarimetric registration algorithms that use feature extraction techniques. Additionally, a search could be conduced for a joint estimator that meets the Cramer-Rao bound. Finally, the idea of representing bounds on image registration as a realization of underlying parameters (in this case, as the weighted sum of the Stokes parameters) may be used to derive bounds for registering multi-modal images if a similar underlying relationship exists.

In addition to the estimator variations presented in section 4.5, the blind deconvolution research should be expanded to include sensor noise and the effects of non-ideal polarization analyzers. The angle bias question may possibly be addressed by systematically eliminating calibration issues or incorporating them into the estimator. Compensation for between channel (neutral density) transmission differences is also desirable. Additionally, the algorithm is readily expanded to included sensitivity to elliptical states of polarization. Finally, it may be of interest to the astrophysical community to reevaluate polarization imagery from the Hubble Faint Object Camera in the context of this new tool.

The optimized analysis research can be expanded in a number of directions. First, the PCA-thresholding research must be tested against field data to account for real-world variations in targets and obscurations. Such a test would be relatively easy to conduct and far superior to simulation. The reasons for this necessity, if not obvious, are discussed in section 5.5. Second, the distribution of possible polarization states (used to calculate the channel correlation matrix) can be improved to include knowledge of the sensor location and possibly the source with respect to the target area. In one possible scenario, the location of the aircraft mounted sensor and the position of the sun can be used to approximate likely polarization states for "flat" dielectric or metal targets underneath trees. The physical mechanisms for this distribution are discussed qualitatively in chapter II. Finally, an actual target

detector (in the classical sense) can be added to the output of the optimized channels to possibly eliminate or reduce the need for a human analyst.

Appendix A. Useful Background Derivations

The purpose of this appendix is to expand on some of the intermediate results from Chapter II.

A.1   The Field Along the Transmission Axis of an Ideal Retarder-Polarizer Pair

At first glance, the result in equation (2.2), which is the scalar sum of orthogonal electric field components after passing through a retarder and polarizer, may appear to be in error. Here, the result is shown to be accurate using the Jones matrices for polarized light. A full accounting of the Jones calculus can be found in many general optics texts (for instance: [3, 16, 31]). Jones matrices describe direct manipulation of the electric field and are therefore quite useful for building up to the definition of the Stokes parameters. After this point, the Jones matrices are abandoned and the Stokes parameters are manipulated directly.

The vector representation of the field in (2.1) is given by:

$$
\mathbf{E} = \begin{bmatrix} u_x\left(t\right) \\ u_y\left(t\right) \end{bmatrix}
\tag{A.1}
$$

At the sensor, this field passes through a retarder (or waveplate), which imposes a phase shift of ϕ between the x and y components, and then a polarizer, which has a primary transmission axis along angle θ. Each of these optical elements is represented by a 2×2 Jones matrix:

$$
\mathbf{E}' = \underbrace{\begin{bmatrix} \cos^2\theta & \cos\theta\sin\theta \\ \cos\theta\sin\theta & \sin^2\theta \end{bmatrix}}_{polarizer} \underbrace{\begin{bmatrix} e^{j\phi} & 0 \\ 0 & 1 \end{bmatrix}}_{waveplate} \mathbf{E}
\tag{A.2}
$$

The resulting field, $\mathbf{E}'$, can be expressed in a rotated coordinate system (using another Jones matrix) where one of the principal axes is also the polarizer transmission

axis:

$$\mathbf{E}_t = \underbrace{\begin{bmatrix} \cos\theta & \sin\theta \\ -\sin\theta & \cos\theta \end{bmatrix}}_{rotation} \mathbf{E}' \tag{A.3}$$

such that, in this new coordinate system:

$$\mathbf{E}_t = \begin{bmatrix} u_x(t)\, e^{j\phi}\cos\theta + u_y(t)\sin\theta \\ 0 \end{bmatrix} \tag{A.4}$$

which is the result in equation (2.2).

A.2 The Decomposition of Partially Linearly Polarized Light

The decomposition of partially linearly polarized light into its constituents is of great importance in Chapter IV. Consequently, the result in equation (2.15) is derived here in detail. Partially polarized light with Stokes vector, $\mathbf{S}$, can be represented as the sum of two Stokes vectors: $\mathbf{S}_u$, the unpolarized component, and $\mathbf{S}_p$, the fully polarized component.

$$\mathbf{S} = \mathbf{S}_u + \mathbf{S}_p \tag{A.5}$$

where

$$\mathbf{S}_u = (1-P)\,S_0 \begin{bmatrix} 1 \\ 0 \\ 0 \\ 0 \end{bmatrix} \tag{A.6a}$$

$$\mathbf{S}_p = P S_0 \begin{bmatrix} 1 \\ \cos 2\psi \\ \sin 2\psi \\ 0 \end{bmatrix} \tag{A.6b}$$

93

where ψ is the angle of polarization (equation 2.13) and P is the degree of polarization in (2.12). From equation (2.7), the measured intensity for the unpolarized component is therefore:

$$I_u = (1 - P)S_0 = \lambda_u \tag{A.7}$$

and, likewise, the measured intensity for the polarized component is:

$$\begin{aligned}
I_p &= \frac{1}{2}PS_0 \left(1 + \cos 2\psi \cos 2\theta + \sin 2\psi \sin 2\theta\right) \\
&= \frac{1}{2}PS_0 \left[1 + \cos 2(\psi - \theta)\right] \\
&= PS_0 \cos^2(\psi - \theta)
\end{aligned} \tag{A.8}$$

and so, by defining $\lambda_p = PS_0$, the total intensity at the detector is given by:

$$I = I_u + I_p = \frac{1}{2}\lambda_u + \lambda_p \cos^2(\psi - \theta) \tag{A.9}$$

which is equation (2.15).

Appendix B. More on the Polarimetric Cramer-Rao Bound

The first two sections of this appendix are devoted to developing mathematically necessities for the bound derivation in Chapter III. The remaining three sections are devoted to expansions on this theme that were not part of the originally published work.

B.1 More on the V and $\tilde{V}$ Matrices

The matrices V and $\tilde{V}$ play a central role in the bound calculation. In addition, the V matrix provides the connection between the previous work by Robinson and Milanfar [33] and the generalization provided here. Consequently, some useful properties of these matrices are developed in this section.

First, there is an important connection between the V, $\tilde{V}$, and H_{ij}:

$$(H_{ij})^T H_{kj} = \frac{a_{ji}a_{jk}}{\sigma^4}\left(\frac{\partial}{\partial \mathbf{v}_j}\mathbf{f}_j^T\right)\left(\frac{\partial}{\partial \mathbf{v}_j}\mathbf{f}_j^T\right)^T = \frac{a_{ji}a_{jk}}{\sigma^2}V_{jj} \qquad (B.1)$$

and

$$(H_{lj})^T H_{ki} = \frac{a_{jl}a_{ik}}{\sigma^4}\left(\frac{\partial}{\partial \mathbf{v}_j}\mathbf{f}_j^T\right)\left(\frac{\partial}{\partial \mathbf{v}_i}\mathbf{f}_i^T\right)^T = \frac{a_{jl}a_{ik}}{\sigma^2}\tilde{V}_{ji} \qquad (B.2)$$

for all $i \neq j$.

Second, each $\mathbf{v}_i$ is established in the plane of the image. Therefore, a common direction vector, $\mathbf{x}$, for all relevant derivatives can be defined via the chain rule:

$$\frac{\partial}{\partial \mathbf{v}_i}\mathbf{f}_i^T = \frac{\partial}{\partial \mathbf{x}}\mathbf{f}_i^T. \qquad (B.3)$$

Consequently, each entry in V and $\tilde{V}$ is defined in a common coordinate system.

B.2 Detailed Derivation of the Stokes Parameter Bound

The average bound can be determined by calculating the trace of equation (3.21) via application of the following properties of the trace and the Kronecker product. For the trace [13]:

$$tr\,(A + G) = tr\,(A) + tr\,(G) \tag{B.4a}$$

$$tr\,(CGD) = tr\,(DCG) \tag{B.4b}$$

$$tr\,(EF) = vec\left(E^T\right)^T vec\,(F) \tag{B.4c}$$

where A and G are square matrices and C, D, E, and F are any matrices such that CGD and EF are square matrices. Operator tr represents the trace and, for any matrix A, $vec(A)$ is defined to be an ordered stack of the columns of A. For the Kronecker product (also from [13]):

$$vec\,(AGC) = \left(C^T \otimes A\right) vec\,(G) \tag{B.5a}$$

$$(A \otimes C)\,(G \otimes D) = (AG \otimes CD) \tag{B.5b}$$

both of which always hold whenever AGC, AG, and CD are defined. Finally, note that, in contrast to regular matrix multiplication:

$$(A \otimes G)^T = A^T \otimes G^T \tag{B.6a}$$

$$(A \bullet G)^T = A^T \bullet G^T \tag{B.6b}$$

Armed with the preceding formulae, derivation of the average bound for each Stokes image is straightforward. Starting with the second term in equation (3.32):

$$
\begin{aligned}
tr\left[\Phi_i^{-1}\left(HB_vH^T\right)\Phi_i^{-T}\right] &= tr\left[\Phi_i^{-T}\Phi_i^{-1}\left(HB_vH^T\right)\right] \\
&= vec\left(\Phi_i^{-T}\Phi_i^{-1}\right)^T vec\left(HB_vH^T\right) \\
&= vec\left(\Phi_i^{-T}\Phi_i^{-1}\right)^T \left(H\otimes H\right)vec\left(B_v\right) \\
&= vec\left[H^T\left(\Phi_i^{-T}\Phi_i^{-1}\right)H\right]^T vec\left(B_v\right)
\end{aligned}
\tag{B.7}
$$

Fortunately, expression $H^T\left(\Phi_i^{-T}\Phi_i^{-1}\right)H$ is identical in form to equation (3.22) and can therefore be simplified in the same manner:

$$
\begin{aligned}
H^T\left(\Phi_i^{-T}\Phi_i^{-1}\right)H &= \sigma^4 H^T\left(C_i^{-T}C_i^{-1}\otimes \mathbf{I}_{p^2\times p^2}\right)H \\
&= \sigma^2 W_{Si}\bullet\left(V+\tilde{V}\right)
\end{aligned}
\tag{B.8}
$$

where

$$
W_{Si} = M\left(C_i^{-T}C_i^{-1}\right)M^T \otimes \mathbf{1}_{2\times 2}
\tag{B.9}
$$

Invoking the implicit symmetry of W_{Si}, V, and $\tilde{V}$:

$$
\begin{aligned}
tr\left[\Phi_i^{-1}\left(HB_vH^T\right)\Phi_i^{-T}\right] &= \sigma^2 vec\left[W_{Si}\bullet\left(V+\tilde{V}\right)\right]^T vec\left(B_v\right) \\
&= \sigma^2 tr\left[W_{Si}\bullet\left(V+\tilde{V}\right)B_v\right]
\end{aligned}
\tag{B.10}
$$

This result can be folded back into (3.31) to produce:

$$
\begin{aligned}
\langle B_{Si}\rangle &= \frac{1}{p^2}\left[tr\left(\Gamma_i^{-1}\right)\right] + \frac{\sigma^2}{p^2}tr\left[W_{Si}\bullet\left(V+\tilde{V}\right)B_v\right] \\
&= \sigma^2 C_{ii}^{-1} + \frac{\sigma^2}{p^2}tr\left[W_{Si}\bullet\left(V+\tilde{V}\right)B_v\right]
\end{aligned}
\tag{B.11}
$$

which is identical to equation (3.35).

B.3 External Measurement Versus Joint Estimation

The bounds derived in III provide the minimum achievable variance for an unbiased estimator in each of the following cases:

- estimates of translational misregistration when the underlying Stokes parameters are known

- estimates of the Stokes images when the registration parameters between channels are known

- joint estimates of registration and Stokes parameters

What remains then is to specify a bound for the cases where misregistration and Stokes estimates are determined separately. This bound can be compared to the joint estimation bound to determine which of these paths yields the best estimator.

For the unrelated problem of bounding estimates on dispersive wave parameters, Kimball (et al.) [19] provides a definition for the total error achieved when Cramer-Rao bounds are considered in conjunction with errors in externally provided parameters. Like in the present work, Kimball employs the natural partitioning of the Cramer-Rao bound using block matrix methods. Going a step further, Kimball then replaces the Cramer-Rao bound for a subset of the parameters with a externally measured covariance matrix. In this way, errors in externally provided parameters can be propagated into the expression for errors in the estimates of the remaining parameters.

To apply Kimball's ideas to the present problem, define ϵ_v^2 to be an externally determined covariance matrix for the channel registration parameters. Note that ϵ_v^2 may be less than V if the misregistration between images has a strong deterministic component. The "total error" matrix for the Stokes image estimates is determined by replacing V with ϵ_v^2 in equation (3.21):

$$\epsilon_S^2 = S^{-1} + S^{-1} H \epsilon_v^2 H^T S^{-1} \tag{B.12}$$

which, in turn, may be simplified using the matrix methods presented in section 3.4.3:

$$\left\langle \epsilon_{Si}^2 \right\rangle = \sigma^2 C_{ii}^{-1} + \frac{1}{p^2} tr \left[W_{Si} \bullet \left(V + \tilde{V} \right) \epsilon_v^2 \right] \tag{B.13}$$

where the i subscript indicates which Stokes parameter is under test.

Equation (B.13) provides the means for evaluating the impact of alternate forms of misregistration correction on Stokes image estimation. This analysis can be used when considering design trade-offs in conjunction with other factors such as cost, processing power, weight, and so on.

B.4 Interpreting the CRLB Using Correlations

Assume that the collected images are bandlimited, sampled at the Nyquist frequency or higher, and periodic. Under these conditions Robinson and Milanfar show that, in the two image case, the terms in the matrix V are independent of the translational error between the images. Proof of this fact is accomplished in the spatial frequency domain via Parseval's theorem. This result can be readily generalized to the present N channel case. Consider Parseval's theorem applied to a non-zero submatrix in V:

$$\frac{1}{\sigma^2} \left(\frac{\partial}{\partial \mathbf{x}} \mathbf{f}_k^T \right) \left(\frac{\partial}{\partial \mathbf{x}} \mathbf{f}_l^T \right)^T = \frac{1}{2\pi\sigma^2} \int\limits_{-\infty}^{\infty} \left[j\omega F_k\left(\omega\right) e^{-j\left(\mathbf{v}_k^T \omega\right)} \right] \left[-j\omega^T F_l^*\left(\omega\right) e^{j\left(\mathbf{v}_l^T \omega\right)} \right] d\omega$$

$$\tag{B.14}$$

where $F_i(\omega)$ is the Fourier transform of image f_i at frequency coordinates ω. The $j\omega$ terms in the right hand side are a result of differentiation in the left hand side and the $e^{-j\left(\mathbf{v}_k^T \omega\right)}$ terms are the Fourier shift theorem representation of the registration errors. Unlike the two image case, it is not immediately clear from this result that the Fisher information matrix is independent of the unknown translations between the images, $\mathbf{v}_k$ and $\mathbf{v}_l$. To resolve the issue, the integral on the right hand side of

(B.14) can be rearranged,

$$= \frac{1}{2\pi\sigma^2} \int\limits_{-\infty}^{\infty} \omega\omega^T F_k(\omega) F_l^*(\omega) \mathrm{e}^{-j\left(\mathbf{v}_k^T - \mathbf{v}_l^T\right)\omega} d\omega \tag{B.15}$$

and treated as an inverse Fourier transform evaluated at the origin of $\mathbf{x}$:

$$= \frac{1}{2\pi\sigma^2} \int\limits_{-\infty}^{\infty} \omega\omega^T F_k(\omega) F_l^*(\omega) \mathrm{e}^{-j\left(\mathbf{v}_k^T - \mathbf{v}_l^T\right)\omega} e^{-j\mathbf{x}^T\omega} d\omega \Bigg|_{\mathbf{x}=\mathbf{0}_{2\times1}} . \tag{B.16}$$

Bringing this all together:

$$\frac{1}{\sigma^2} \left(\frac{\partial}{\partial\mathbf{x}}\mathbf{f}_k^T\right) \left(\frac{\partial}{\partial\mathbf{x}}\mathbf{f}_l^T\right)^T = \frac{-1}{\sigma^2}\frac{\partial}{\partial\mathbf{x}} \left(\frac{\partial}{\partial\mathbf{x}}[f_k \star f_l](\mathbf{x})\right)^T \Bigg|_{\mathbf{x}=\mathbf{v}_k - \mathbf{v}_l} \tag{B.17}$$

where $\star$ is the correlation operation. Evaluation of the correlated images at $\mathbf{x} = \mathbf{v_k} - \mathbf{v_l}$ is equivalent to evaluation of the registered images at the origin; in other words, the Fisher Information matrix does not depended on the translation between images and the generalization of the two image case is confirmed.

The observation that V and $\tilde{V}$ can be calculated from the second order derivatives of the cross-correlation is also of interest. First, correlation is not a one-to-one mapping over all possible image pairs. As such, two unique ensembles of images have the same Fisher information matrix if their cross-correlations are the same. Indeed, the cross-correlations need only to be equal near $\mathbf{x} = \mathbf{v_k} - \mathbf{v_l}$ since only the second derivative behavior at this point is of consequence. Heuristically, this result means that images with similar second order statistics, for instance imagery over similar terrain, will result is similar bounds.

For the joint Stokes restoration problem, the cross-correlation between images can be recast in terms of the Stokes vectors:

$$\frac{\partial}{\partial \mathbf{x}} \left(\frac{\partial}{\partial \mathbf{x}} \left[f_k \star f_l \right] (\mathbf{x}) \right)^T = \frac{\partial}{\partial \mathbf{x}} \left(\frac{\partial}{\partial \mathbf{x}} \left[\sum_i \sum_j a_{ki} a_{lj} \left(S_i \star S_j \right) \right] (\mathbf{x}) \right)^T \qquad \text{(B.18)}$$

It is therefore clear that polarization channel orientation may serve to suppress or reenforce the contribution to the correlation amongst the individual Stokes images.

B.5 A CRLB for the Blind Deconvolution Polarization Parameterization

As demonstrated throughout this dissertation, it is often useful to switch between parameterizations of polarization state in order to best suit a particular problem. In Chapter IV, the Stokes vector parameterization was replaced with an intensity and angle parameterization in order to meet the requirements of the complete data model. As a bridge between these two chapters, this section describes a mechanism for transforming the Stokes parameterized CRLB into one using the intensity-angle parameterization.

Recall that the original Stokes image parameter vector has the form:

$$\theta = \left[\ \mathbf{v}_2^T \ldots \mathbf{v}_N^T \quad \mathbf{S}_0^T \cdots \mathbf{S}_2^T \ \right]^T, \qquad \text{(B.19)}$$

where vectors $\mathbf{v}_x$ are registration parameters and $\mathbf{S}_x$ are the true Stokes parameter values for each point in the image. Similarly, a likelihood parameterization must be defined for the intensity-angle parameterization:

$$\mathbf{w} = \left[\ \mathbf{v}_2^T \ldots \mathbf{v}_N^T \quad \lambda_u^T \quad \lambda_p^T \quad \alpha^T \ \right]^T \qquad \text{(B.20)}$$

where the $\mathbf{v}_x$ vectors are the same as before and each of λ_u, λ_p, and α^T represent the unpolarized intensities, polarized intensities, and angles of polarization for each point in the image. Note that both θ and $\mathbf{w}$ have the same dimensions. Using

these parameter vectors, the transformed Fisher information matrix, J', is defined by Scharf [36] as:

$$J' = GJG^T \tag{B.21}$$

where J is the FIM in equation (3.1) and the elements of G are given by:

$$G_{ij} = \frac{\partial \theta_j}{\partial w_i} \tag{B.22}$$

where i, j are the row and column indices of G. As before, the CRLB in the unbiased case is given by the inverse of J'.

What remains then is to define the entries in G. First, note that the registration terms are the same in both parameterizations; in that case:

$$\frac{\partial \mathbf{v}_j^T}{\partial \mathbf{v}_i} = \begin{cases} I_{2\times 2} & \text{if } i = j, \\ 0_{2\times 2} & \text{if } i \neq j \end{cases} \tag{B.23}$$

which, together over $i, j = 2$ to N, form a submatrix of G, henceforth referred to as g_1.

Next we note that the translation parameters and the intensity parameters (in either form) are not dependent on each other. Thus the partial derivatives of any of these parameters with respect to any translational parameter is zero (e.g. $\frac{\partial S_0^T}{\partial v_2} = 0_{2\times p^2}$, $\frac{\partial \alpha^T}{\partial v_2} = 0_{2\times p^2}$, etc).

The remainder of the terms describe the transformation between the Stokes and intensity-angle parameters. At each point $\mathbf{m}_n$, the Stokes parameters can be

described as:

$$S_0(\mathbf{m}_n) = \lambda_u(\mathbf{m}_n) + \lambda_p(\mathbf{m}_n) \tag{B.24a}$$

$$S_1(\mathbf{m}_n) = \frac{\lambda_p(\mathbf{m}_n)}{\sqrt{1 + \tan^2 \alpha(\mathbf{m}_n)}} \Upsilon(\alpha(\mathbf{m}_n)) \tag{B.24b}$$

$$S_2(\mathbf{m}_n) = S_1(\mathbf{m}_n) \tan(2\alpha(\mathbf{m}_n)) \tag{B.24c}$$

where

$$\Upsilon(\alpha) = \begin{cases} 1 & -45^o < \alpha(\mathbf{m}_n) < 45^o \\ -1 & otherwise \end{cases} \tag{B.25}$$

which, all together, can be used to populate the remaining components of G. A number of these derivative terms can be expressed analytically. Assuming $n = k$, for the unpolarized component:

$$\frac{\partial S_0(\mathbf{m}_n)}{\partial \lambda_u(\mathbf{m}_k)} = 1 \tag{B.26a}$$

$$\frac{\partial S_1(\mathbf{m}_n)}{\partial \lambda_u(\mathbf{m}_k)} = \frac{\partial S_2(\mathbf{m}_n)}{\partial \lambda_u(\mathbf{m}_k)} = 0 \tag{B.26b}$$

the polarized component:

$$\frac{\partial S_0(\mathbf{m}_n)}{\partial \lambda_p(\mathbf{m}_k)} = 1 \tag{B.27a}$$

$$\frac{\partial S_1(\mathbf{m}_n)}{\partial \lambda_p(\mathbf{m}_k)} = \frac{\Upsilon[\alpha(\mathbf{m}_n)]}{\sqrt{1 + \tan^2 \alpha(\mathbf{m}_n)}} \tag{B.27b}$$

$$\frac{\partial S_2(\mathbf{m}_n)}{\partial \lambda_p(\mathbf{m}_k)} = \frac{\partial S_1(\mathbf{m}_n)}{\partial \lambda_p(\mathbf{m}_k)} \tan[2\alpha(\mathbf{m}_n)] \tag{B.27c}$$

and the polarization angle:

$$\frac{\partial S_0(\mathbf{m}_n)}{\partial \alpha(m_k)} = 0. \tag{B.28}$$

Note that $\frac{\partial S_1(m_n)}{\partial \alpha(m_k)}$ and $\frac{\partial S_2(m_n)}{\partial \alpha(m_k)}$ do not have a simple, closed form solution. Finally, in all cases with $n \neq k$, the partials in B.26, B.27, and B.28 are all zero. This region of

103

G is collectively referred to as g_2. Thus:

$$G = \begin{bmatrix} g_1 & 0_{2(N-1) \times 3p^2} \\ 0_{3p^2 \times 2(N-1)} & g_2 \end{bmatrix} \tag{B.29}$$

Appendix C. Derivation of the polarization angle estimator for the three channel case

Here we derive the polarization angle estimator for the case of polarization analyzers oriented at 0°, 60°, and -60°. Three trigonometric identities are required:

$$\tan(\alpha - \theta_c) = \frac{\tan \alpha - \tan \theta_c}{1 + \tan \alpha \tan \theta_c} \tag{C.1a}$$

$$\tan 2\alpha = \left(\frac{1}{\cos 2\alpha} + 1\right) \tan \alpha \tag{C.1b}$$

$$\sin 2\alpha = \frac{2 \tan \alpha}{\tan^2 \alpha + 1} \tag{C.1c}$$

Apply the first identity to equation (4.9) part (c), divide out the common denominator, and evaluate the result at each θ_c:

$$\sqrt{3}\left(\Psi_3 - \Psi_2\right)\left[\tan^2 \alpha + 1\right] + 4\left(\Psi_1 + \Psi_2 + \Psi_3\right)\tan \alpha - 3\Psi_1 \tan \alpha \left[\tan^2 \alpha + 1\right] = 0 \tag{C.2}$$

where for compactness, $\Psi_k = \sum_y \psi_{pk}^{n+1}(y, x_o)$ and $\alpha = \alpha^{n+1}(x_0)$. This result is reduced further by applying (4.12):

$$S_0^{n+1} = \frac{2}{3}\left(\Psi_1 + \Psi_2 + \Psi_3\right) \tag{C.3a}$$

$$S_1^{n+1} = \frac{2}{3}\left(\Psi_1 - \Psi_2 - \Psi_3\right) \tag{C.3b}$$

$$S_2^{n+1} = \frac{2}{\sqrt{3}}\left(\Psi_2 - \Psi_3\right) \tag{C.3c}$$

such that (C.2) becomes:

$$-\frac{3}{2}S_2^{n+1} + 3S_0^{n+1}\frac{2 \tan \alpha}{\tan^2 \alpha + 1} + \frac{3}{2}\left(S_0^{n+1} + S_1^{n+1}\right)\tan \alpha = 0. \tag{C.4}$$

Now apply (2.14), along with the remaining identities to achieve:

$$-\frac{3}{2}S_2^{n+1} + 3S_2^{n+1} + \frac{3S_1^{n+1}}{2}\tan 2\alpha = 0 \tag{C.5}$$

which, when solved for α, becomes equation (4.13).

Appendix D. Practical Laboratory Polarimetric Imagers

Laboratory collected imagery plays an important role in the bound examples from chapter III and in the validation of the deconvolution algorithm in Chapter IV. For completeness and as an aid to future progression of this work, the laboratory system are described in detail in this appendix. The constructed sensors fall into two categories based on how the data are collected: serial (each channel is collected sequentially) and parallel (all channels are collected simultaneously). The tradeoffs between these configurations will be discussed in the sections that follow. Obviously, there are many practical polarimetric imaging collection schemes other than those addressed here; these particular configurations represent two simple and effective approaches that can be obtained with minimal cost and time investment.

D.1   The Serial Imager

The serial imager consists of a variable analyzer, focusing lens, aperture stop, and focal plane array (field stop). The basic setup is shown in figure D.1. The required sequence of images is collected by manipulating the analyzer between frames.
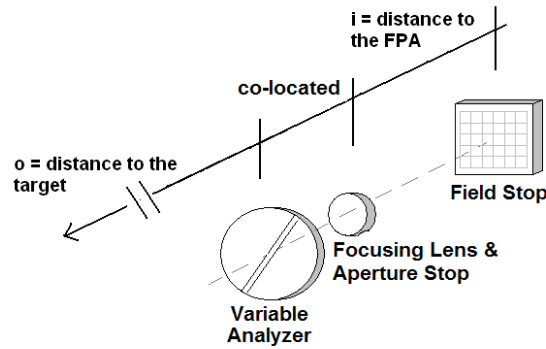
Figure D.1: Diagram of the single channel polarimetric imager.

The variable polarization analyzer, aperture stop, and focusing lens are all co-located. The front and back of this assembly are shown in figure D.2. The variable

analyzer determines the orientation of the preferred angle of polarization with respect to some reference (in this case, the plane of optical bench). The preferred orientation is adjusted by mechanically rotating the polarizing element between images.
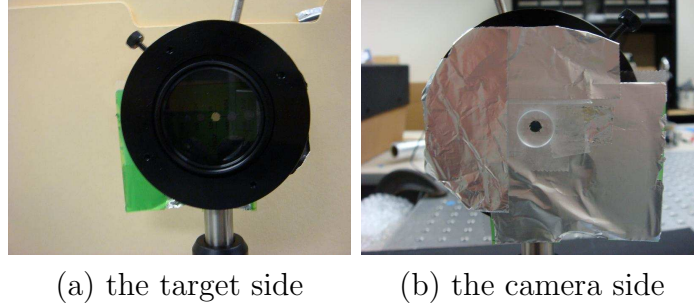

(a) the target side   (b) the camera side

Figure D.2: The serial imager analyzer-stop-lens assembly.

For a convex focusing lens with focal length f, the thin lens equation gives us:

$$\frac{1}{f} = \frac{1}{o} + \frac{1}{i} \tag{D.1}$$

where o is the distance from the focusing lens to the target and f is the focal length of the lens. Overall target magnification, m_T is given by:

$$m_T = \frac{i}{o} \tag{D.2}$$

In this scenario, the image at the focal plane will be real and inverted.

The aperture stop is located between the variable analyzer and the focusing lens. In this scenario, the primary purpose of the aperture stop is to ensure proper sampling of the point spread function. Somewhat counter-intuitively, proper sampling of the PSF in the image plane is ensured by only considering the sampling in the aperture. In the quasi-monochromatic Fresnel diffraction regime, sampling in the aperture plane, Δu, is related to sampling in the frequency space of the image, $\Delta \zeta$, and is given by [9]:

$$\Delta u = \Delta\zeta\lambda z = \frac{\lambda z}{N\Delta x} \tag{D.3}$$

where λ is the center wavelength of the illumination, z is the distance between the exit pupil and the imaging plane, N is the number of samples across the imaging plane, and Δx is the sampling in the image plane (fixed by choice of the FPA). It is worth noting that, unless the optics in question are very large or z is very short, this imager will always be operated in the Fresnel regime. Furthermore, it is assumed that the FPA is square. In this setup, the exit pupil is always the aperture stop itself and $z = i$ in figure D.1.

For incoherent image formation, the PSF is proportional to the magnitude squared of the Fourier transform of the aperture function (see equation 4.15). From [9], the maximum spatial frequency passed by this optical system (i.e. the cutoff frequency) in this scenario is:

$$\zeta_c = \frac{2R}{\lambda z} \tag{D.4}$$

where R is the radius of the aperture stop. Hence, to exceed the Nyquist threshold for sampling, $N\Delta\zeta > 2\zeta_c$ or, in other words:

$$R < \frac{\lambda z}{4\Delta x} \tag{D.5}$$

It is also often convenient to express this result as $N > 4\frac{R}{\Delta u}$.

Finally, the aperture stop and focusing lens together also determine the irradiance that reaches the FPA (throughput). According to [31], the irradiance at the FPA is proportional to $\left(\frac{2R}{f}\right)^2$ (i.e. the inverse of the f-number squared). For a fixed focal length, reducing the aperture radius by a factor of 2 means that only $\frac{1}{4}$ of the photons reach the FPA. Therefore, the camera integration time must be 4 times as long to achieve the same photon (and noise) levels.

Table D.1: A workable serial polarimetric imager.

f	o	i	R	Δx
25 cm	29 cm	133 cm	1.588 mm	16 um

The choice of focusing lens and aperture stop is a trade-off between the space available for the laboratory setup, the desired target magnification, the sampling requirements imposed by the FPA, and throughput. The polarization analyzer itself plays no particular role in this analysis. As a guideline, the greatest system flexibility is achieved by choosing the largest possible aperture given the available FPA, lenses and lab space. Magnification is a secondary issue (unless the image exceeds the space on the FPA) and one may always reduce the size of the aperture without violating the sampling requirements in (D.5). An additional benefit to selecting larger apertures is that larger apertures are easier to aberrate (which is useful primarily for testing blind deconvolution algorithms). Table D.1 contains the design used to produce the laboratory example in Chapter IV.

D.1.1   Advantages and Disadvantages.   Besides ease of setup, the other advantages of the serial imager include precise and easily verifiable angular channel positioning without speciality machined parts. Additionally, each channel may be focused and/or stopped individually with minimal extra effort. Assuming the same focal plane is used in both configurations, more pixels are available per channel which translates into improved resolution or increased field of view depending on the specific configuration.

There are also disadvantages to the serial imager. First, the variable polarizer must be adjusted between collections for each channel. This substantially increases time spent in the laboratory and often requires that collected images be registered in post processing. Second, the target must remain static between collections.

D.2 The Parallel Imager

The imaging polarimeter described in this section captures both target intensity and polarization state simultaneously. The optical system consists of three primary components: the channel lens array, an image reducing optic, and field stop. The aperture stop and channel analyzers are co-located with the lens array. These components are arranged as shown in figure D.3.
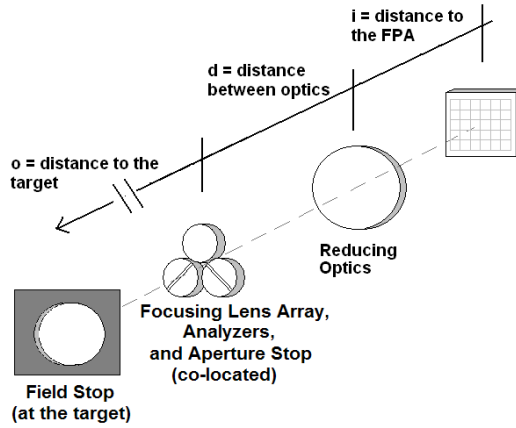

Figure D.3: Diagram of the parallel polarimetric imager.

The target scene, defined by the limits of the field stop, is imaged separately by each of the lenses in the channel lens array. Each channel is most sensitive to polarization in a different way. Consequently, the intermediate images formed by the lens array communicate different target polarization information. The intermediate images are spatially separated from each other by the diameter of the lenses themselves. This composite of images is made to fit onto the focal plane array via the reducing optic. Once digitized, the composite image is processed to form a single polarization image.

The channel lens array is an optical component that produces three separate images of the target scene each of which responds to polarized light in a different way. Each of three channels consist of an aperture stop, polarizing filter (analyzer) and a small diameter lens. Baffling is placed around the array and in the small

111

region in the array center to reject unintended illumination from the target. Each channel is identical except for the orientation of the analyzer (0°, 60°, and -60°). The radius of the stop is determined again by (D.5) to meet sampling requirements, though calculation of z is somewhat more complicated (as shown below). The front and back of this array are shown in figure D.4.

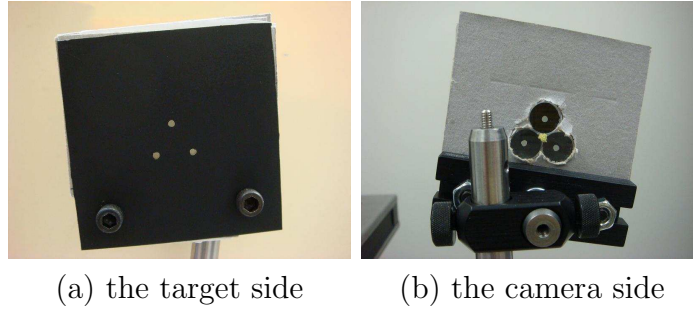(a) the target side   (b) the camera side

Figure D.4: The parallel imager channel lens assembly.

The three images formed by the lens array alone (along with the empty space between images) are much too large to fit on a typical CCD array therefore a reducing optic is required to achieve the requisite size. The reducing optic is used to minify the composite image formed by the channel lens array such that it fits entirely within the confines of the focal plane array. The reducing optic must be large enough (compared to the size of the focal plane array) to ensure that the reducing optic does not inadvertently define the system field stop.

The field stop defines the limits of the target scene for each channel image on the FPA. As shown in figure D.3, the channel stop is implemented in the target plane. This stop can be realized physically by either placing an aperture in front of the illuminating source or by placing an aperture between the target and lens array (though still in the target plane). The former option allows for either front or back illumination of the target and is therefore the preferred method. Target illumination is provided by an LED source. Though LEDs are highly directional, target illumination will be uniform so long as the solid angle defined by the limiting

aperture is small compared to the LED viewing angle (which is, by convention, the angle between half intensity points on either side of direct viewing).

D.2.1 System Design Restrictions. Despite the relatively small number of components involved, there are a number of important restrictions considered during the design process. These restrictions include the location and size of the system stops, the size and spacing of the composite image on the FPA, and the space available in the lab for layout of the system end to end. The following section describes each of these restrictions in detail.

As mention previously, each stop in the channel array is intended to serve as an aperture stop. The image of the optical element in object space that subtends the smallest angle at the on-axis position of the target is the entrance pupil. The physical element that corresponds to the entrance pupil is the aperture stop [31]. This criterion is satisfied when:

$$D_s < \frac{\left| \frac{f_c}{d-f_c} \right| D_r o}{o - \frac{df_c}{d-f_c}} \tag{D.6}$$

where D_r and D_s are the diameters of the reducing lens and channel stops, f_c is the focal length of the channel lenses, and o and d are as defined in figure D.3. In actual application this criterion is almost always met because the stops in the channel array are of a much smaller diameter than the reducing lens. The upper limit on D_s is the width of a channel lens.

Additionally, the focal plane array must serve as the composite image field stop. The image in object space of the optical element that subtends the smallest angle at the on axis position of the entrance pupil is the entrance window. The physical element that corresponds to the entrance window is the field stop [31]. Consequently, the reducing lens meet the following condition:

$$D_r > \frac{d}{o}\frac{W_{FPA}}{M} \tag{D.7}$$

where W_{FPA} is the width of the focal plane array, M is the overall system magnification, and D_r is the diameter of the reducing lens. Implicit in equation (D.7) is the assumption that the channel array is, in fact, the location of the aperture stop.

The sensor design requires that all channels be imaged simultaneously on a single focal plane array. As shown in figure D.5, several new quantities are required to mathematically define this requirement in addition to those already defined: the width of the field stop, D_{fs}, and the magnification of the channel lens alone, M_c.
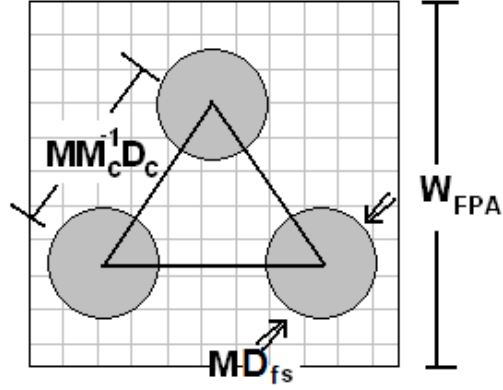

Figure D.5: The projected image on the FPA.

Figure D.5 demonstrates two obvious restrictions on the optical setup. First the longest dimension of the composite image must be less than the width of the focal plane:

$$MM_c^{-1}D_c + MD_{fs} \leq W_{FPA} \tag{D.8}$$

where D_c is the diameter of a channel lens (which is, in general, different than the diameter of the aperture stop). Second, the images themselves must not overlap:

$$\frac{D_c}{D_{fs}} \geq M_c \tag{D.9}$$

Ideally, M_c should be made as large as possible to ensure a maximum number of samples across the target image (i.e. the most efficient use of available detectors on the focal plane array.)

The sensor as described is primarily intended to be a lab instrument therefore compact packaging requirements are not as restrictive as those for field instruments. Regardless, lengthy optical systems are more difficult to align and lab space is often lacking. As such, overall system length, L, is an important design criterion.

$$L = o + d + i \tag{D.10}$$

where o, d, and i are defined in figure D.3. Given the requirement for a specific system magnification and an object distance, both i and d can be solved for by repeated application of the thin lens equation as shown in [16]:

$$
\begin{aligned}
M &= \frac{f_c i}{d(o-f_c)-of_c} \\
i &= \frac{f_r d - \frac{f_c f_r o}{o-f_c}}{d - f_r - \frac{f_c o}{o-f_c}}
\end{aligned}
\tag{D.11}
$$

where the only thing yet to be defined is f_r, the focal length of the reducing lens.

Within these confines, it is best to maximize the total system magnification (once the required field stop diameter is determined) to ensure a maximum number of pixels across the target. This step should not be confused with the PSF sampling requirements from D.5, which are still necessities. Recall that PSF sampling depends on the radius of the aperture stop and can be made quite small at the cost of reduced throughput. Table D.2 contains the design used to produce the laboratory example in Chapter IV.

Table D.2: A workable parallel polarimetric imager

f_c	D_c	D_s	f_r	D_r
25 cm	12.5 mm	2.38 mm	10 cm	5.08 cm
o	i	d	D_{fs}	Δx
55 cm	8 cm	5 cm	2.5 cm	16 um

D.2.2   Advantages and Disadvantages.   The primary advantage of this system, which should not be understated, is the fact that all channels image simultaneously. The primary disadvantages are added complexity and reduced field of view (when compared to a single channel imager) and the necessity of placing the field stop at the target. This design could readily be improved by incorporating a field stop into the optical system. To do so, a stopped, intermediate image could be formed at the location of the target in the current design.

Bibliography

1. et al., Dempster, A. P. "Maximum likelihood from incomplete data via the EM algorithm". *J.R. Stat. Soc. B*, 39:1–37, 1977.

2. Aron, Y. and Y. Gronau. "Polarization in the LWIR: a method to improve target aquisition". B. F. Andresen and G. F. Fulop (editors), *Infrared Technology and Applications XXXI. Edited by Andresen, Bjorn F.; Fulop, Gabor F. Proceedings of the SPIE, Volume 5783, pp. 653-661 (2005).*, volume 5783 of *Presented at the Society of Photo-Optical Instrumentation Engineers (SPIE) Conference*, 653–661. May 2005.

3. Born, M. and E. Wolf. *Principles of Optics: Electromagnetic Theory of Propagation, Interference and Diffraction of Light.* Cambridge University Press, 2000.

4. Capetti, A., F. Macchetto, D. J. Axon, W. B. Sparks, and A. Boksenberg. "Hubble Space Telescope Imaging Polarimetry of the Inner Nuclear Region of NGC 1068". *apjl*, 452:L87+, October 1995.

5. Collett, Edward. *Polarized Light: Fundamentals and Applications.* Marcel Dekker, Inc., New York, 1992.

6. Egan, W. G. "Polarization in Remote Sensing". *Proc. SPIE Vol. 891, p. 2-9, Polarization Considerations for Optical Systems*, volume 891 of *Presented at the Society of Photo-Optical Instrumentation Engineers (SPIE) Conference*, 2–9. 1988.

7. Egan, W. G. "Polarization in remote sensing". W. G. Egan (editor), *Polarization and remote sensing; Proceedings of the Meeting, San Diego, CA, July 22, 23, 1992 (A93-30026 11-35), p. 2-48.*, volume 1747 of *Presented at the Society of Photo-Optical Instrumentation Engineers (SPIE) Conference*, 2–48. December 1992.

8. Egan, Walter. *Photometry and Polarization in Remote Sensing.* Elsevier, New York, 1985.

9. Ersoy, O.K. *Diffraction, fourier optics, and imaging.* Hoboken, NJ: Wiley-Interscience, 2007.

10. Fish, D.A. et al. "Blind deconvolution by means of the Richardson-Lucy algorithm". *J. Opt. Soc. Am. A*, 12(1):58–65, 1995.

11. Gerchberg, RW and WO Saxton. "A practical algorithm for the determination of phase from image and diffraction plane pictures". *Optik*, 35(2):237–246, 1972.

12. Goodman, Joseph. *Statistical Optics.* John Wiley and Sons, New York, wiley classics library edition edition, 2000.

13. Graham, A. *Kronecker Products and Matrix Calculus With Applications.* Wiley, New York, 1982.

14. Guyot, Steve, Makrina Anastasiadou, Eric Deléchelle, and Antonello De Martino. "Registration scheme suitable to Mueller matrix imaging for biomedical applications". *Opt. Express*, 15(12):7393–7400, 2007. URL http://www.opticsexpress.org/abstract.cfm?URI=oe-15-12-7393.

15. Healy, MJR. *Matrices for Statistics.* Oxford University Press, USA, 1986.

16. Hecht, Eugene. *Optics.* Addison Wesley, San Fransisco, 4th edition edition, 2002.

17. Jones, K.J. "Wavelet image processing applied to hyperspectral images for foliage penetration". *Proceedings of SPIE*, 5102:56, 2003.

18. Kay, S.M. *Fundamentals of statistical signal processing: estimation theory.* 1993.

19. Kimball, CV, P. Lewicki, NI Wijeyesekera, S.D. Res, and CT Ridgefield. "Error analysis of maximum likelihood estimates of physical parameters from one or more dispersive waves". *Signal Processing, IEEE Transactions on [see also Acoustics, Speech, and Signal Processing, IEEE Transactions on]*, 43(12):2928–2936, 1995.

20. Kishimoto, M., L. E. Kay, R. Antonucci, T. W. Hurt, R. D. Cohen, and J. H. Krolik. "Ultraviolet Imaging Polarimetry of the Seyfert 2 Galaxy Markarian 3". *apj*, 565:155–162, January 2002.

21. Kundur, D. and D. Hatzinakos. "Blind image deconvolution". *Signal Processing Magazine, IEEE*, 13(3):43–64, 1996.

22. Kundur, D. and D. Hatzinakos. "Blind image deconvolution revisited". *Signal Processing Magazine, IEEE*, 13(6):61–63, 1996.

23. LeMaster, D.A. "A Comparison of Template Matching Registration Methods for Polarimetric Imagery". *Aerospace Conference, 2008 IEEE*, volume 1, 1–9. 2008.

24. LeMaster, D.A. "Fundamental estimation bounds for polarimetric imagery". *Opt. Express*, 16:12018–12036, 2008.

25. LeMaster, D.A. and S.C. Cain. "Multichannel blind deconvolution of polarimetric imagery". *J. Opt. Soc. Am. A*, 25:2170–2176, 2008.

26. LeMaster, Daniel A. "Enhanced Detection through Obscurations using Optimized Temporal Polarization Imaging". *Aerospace Conference, 2007 IEEE*, volume 1, 1–11. 2007.

27. Lin, S.S., K.M. Yemelyanov, E.N. Pugh, Jr, and N. Engheta. "Separation and contrast enhancement of overlapping cast shadow components using polarization". *Optics Express*, 14(16):7099–7108, 2006.

28. Miao, George J. *Digital Signal Processing and Statistical Classification.* Artech House, Boston, MA, 2002.

29. Moon, T.K. "The expectation-maximization algorithm". *Signal Processing Magazine, IEEE*, 13(6):47–60, 1996.

30. Nashashibi, AY and FT Ulaby. "Detection of stationary foliage-obscured targets by polarimetric millimeter-wave Radar". *Geoscience and Remote Sensing, IEEE Transactions on*, 43(1):13–23, 2005.

31. Pedrotti, F.L. and L.S. Pedrotti. *Introduction to Optics 2nd Edition.* Prentice Hall, 1993.

32. Persons, C. M., D. B. Chenault, M. W. Jones, K. D. Spradley, M. G. Gulley, and C. A. Farlow. "Automated registration of polarimetric imagery using Fourier transform techniques". D. H. Goldstein and D. B. Chenault (editors), *Polarization Measurement, Analysis, and Applications V. Edited by Goldstein, Dennis H.; Chenault, David B. Proceedings of the SPIE, Volume 4819, pp. 107-117 (2002).*, volume 4819 of *Presented at the Society of Photo-Optical Instrumentation Engineers (SPIE) Conference*, 107–117. September 2002.

33. Robinson, D. and P. Milanfar. "Fundamental performance limits in image registration." *IEEE Trans Image Process*, 13(9):1185–1199, September 2004. ISSN 1057-7149.

34. Roggemann, Michael and Byron Welsh. *Imaging Through Turbulence.* CRC Press, Boca Raton, 1996.

35. Scharf, LL and LT McWhorter. "Geometry of the Cramer-Rao bound". *Statistical Signal and Array Processing, 1992. Conference Proceedings., IEEE Sixth SP Workshop on*, 5–8, 1992.

36. Scharf, Louis L. *Statistical Signal Processing: detection, estimation, and time series analysis.* Addison-Wesley, Reading, Massachusetts, 1991.

37. Schilling, B.W., D.N. Barr, G.C. Templeton, L.J. Mizerka, and C.W. Trussell. "Multiple-return laser radar for three-dimensional imaging through obscurations". *Appl. Opt*, 41(15):2791–2799, 2002.

38. Schulz, T., B. Stribling, and J. Miller. "Multiframe blind deconvolution with real data: imagery of the Hubble Space Telescope". *Optics Express*, 1(11):355–362, 1997.

39. Schulz, T.J. "Multiframe blind deconvolution of astronomical images". *J. Opt. Soc. Am. A*, 10(5):1064–1073, 1993.

40. Shepp, L. and Y. Vardi. "Maximum likelihood reconstruction for emission tomography". *IEEE Transactions on Medical Imaging*, 1(2):113–122, October 1982.

41. Shih-Schon Lin Yemelyanov, E.N. Jr. Engheta N., K.M. Pugh. "Polarization Enhanced Visual Surveillance Techniques". *Networking, Sensing and Control, 2004 IEEE International Conference on*, volume 1, 216–221. 2004.

42. Shurcliff, William A. *Polarized Light: Production and Use.* Harvard University Press, Cambridge, MA, 1962.

43. Strong, David M. *Polarimeter Blind Deconvolution Using Image Diversity.* Ph.D. thesis, Air Force Institute of Technology, Wright Patterson Air Force Base, Ohio, September 2007.

44. Tyo, J. S., M. P. Rowe, E. N. Pugh, Jr., and N. Engheta. "Target detection in optically scattering media by polarization-difference imaging". *Applied Optics*, 35:1855–+, April 1996.

45. Tyo, JS. "Optimum linear combination strategy for an N-channel polarization-sensitive imaging or vision system". *Journal of the Optical Society of America A*, 15(2):359–366, 1998.

46. Tyo, J.S. "Design of optimal polarimeters: maximization of signal-to-noise ratio and minimization of systematic error". *Appl. Opt*, 41:619–630, 2002.

47. Victor, Whitehead and Kinsell Coulson. "Remote Sensing in Polarized Light". NASA Conference Publication 3014. NASA Lyndon B. Johnson Space Center, NASA Scientific and Technical Information Division, November 3-5 1987.

48. Wang, Xianbing, Shizhi Yang, Jinji Ma, and Yanli Qiao. "Automated registration of polarimetric image using wavelet transform techniques". volume 5832, 695–702. SPIE, 2005.

49. Wolf, E. "Can a light beam be considered to be the sum of a completely polarized and a completely unpolarized beam?" *Opt. Lett.*, 33(7):642–644, 2008. URL http://ol.osa.org/abstract.cfm?URI=ol-33-7-642.

50. Yetik, A., I.S.; Nehorai. "Performance bounds on image registration". *Signal Processing, IEEE Transactions on [see also Acoustics, Speech, and Signal Processing, IEEE Transactions on]*, 54(5):1737–1749, May 2006. ISSN 1053-587X.

51. Zallat, J. and C. Heinrich. "Polarimetric data reduction: a Bayesian approach". *Optics Express*, 15(1):83–96, 2007.

52. Zitova, Barbara and Jan Flusser. "Image registration methods: a survey". *Image and Vision Computing*, 21(11):977–1000, October 2003. URL http://dx.doi.org/10.1016/S0262-8856(03)00137-9.

REPORT DOCUMENTATION PAGE

Form Approved
OMB No. 0704–0188

1. REPORT DATE *(DD–MM–YYYY)*	2. REPORT TYPE	3. DATES COVERED *(From — To)*
11–09–2008	PhD Dissertation	Sept 2005 — Sept 2008

4. TITLE AND SUBTITLE

Statistical Processing Methods
for
Polarimetric Imagery

5a. CONTRACT NUMBER

5b. GRANT NUMBER

5c. PROGRAM ELEMENT NUMBER

6. AUTHOR(S)

Daniel A. LeMaster, GG-12, DAF

5d. PROJECT NUMBER

08-321

5e. TASK NUMBER

5f. WORK UNIT NUMBER

7. PERFORMING ORGANIZATION NAME(S) AND ADDRESS(ES)

Air Force Institute of Technology
Graduate School of Engineering and Management (AFIT/EN)
2950 Hobson Way
WPAFB OH 45433-7765

8. PERFORMING ORGANIZATION REPORT NUMBER

AFIT/DEE/ENG/08-18

9. SPONSORING / MONITORING AGENCY NAME(S) AND ADDRESS(ES)

AFRL-DESA
Dr. Victor Gamiz
3550 Aberdeen Ave, Bldg 422
Kirtland AFB, NM 87117
DSN: 246-4846 email: victor.gamiz@kirtland.af.mil

10. SPONSOR/MONITOR'S ACRONYM(S)

11. SPONSOR/MONITOR'S REPORT NUMBER(S)

12. DISTRIBUTION / AVAILABILITY STATEMENT

APPROVED FOR PUBLIC RELEASE; DISTRIBUTION UNLIMITED.

13. SUPPLEMENTARY NOTES

14. ABSTRACT

Estimation theory is applied to a physical model of incoherent polarized light to address problems in polarimetric image registration, restoration, and analysis for electro-optical imaging systems. In the image registration case, the Cramer-Rao lower bound on unbiased joint estimates of the registration parameters and the underlying scene is derived, simplified using matrix methods, and used to explain the behavior of multi-channel linear polarimetric imagers. In the image restoration case, a polarimetric maximum likelihood blind deconvolution algorithm is derived and tested using laboratory and simulated imagery.Finally, a principal components analysis is derived for polarization imaging systems. This analysis expands upon existing research by including an allowance for partially polarized and unpolarized light.

15. SUBJECT TERMS

statistical image processing, polarization imaging, blind deconvolution, Cramer-Rao bounds

16. SECURITY CLASSIFICATION OF:			17. LIMITATION OF ABSTRACT	18. NUMBER OF PAGES	19a. NAME OF RESPONSIBLE PERSON
a. REPORT	b. ABSTRACT	c. THIS PAGE			Stephen C. Cain (stephen.cain@afit.edu)
U	U	U	UU	132	**19b. TELEPHONE NUMBER** *(include area code)* (937) 255–3636, ext 4716

Standard Form 298 (Rev. 8–98)
Prescribed by ANSI Std. Z39.18